

DISS. ETH NO. 19532

**Transient tunnel inflow and hydraulic conductivity
of fractured crystalline rocks in the Central Alps
(Switzerland)**

A dissertation submitted to

ETH ZURICH

for the degree of

Doctor of Sciences

presented by

Olivier Masset

Diplôme de Géologue, Université de Lausanne

18th of May 1977

citizen of Châtillon FR, Switzerland

accepted on the recommendation of

Prof. Dr. Simon Loew, examiner
Prof. Dr Jean-Michel Lemieux, co-examiner
Prof. Dr Olivier Bour, co-examiner

2011

Acknowledgements

I would like to thank my supervisor Prof. Simon Loew for giving me the opportunity to work on this challenging thesis project. Above all I appreciated his availability; his door was always open and I felt free to step in at anytime for discussion.

I would also like to thank my co-supervisor Prof. Jean-Michel Lemieux for his help and support which he provided at a difficult time of my PhD.

I am also thankful to Prof. Olivier Bour, for welcoming me in Rennes and being my external supervisor.

I also want to thank NAGRA for the funding of the thesis and more particularly Dr. Andreas Gautschi for his support and nice feedbacks.

I thank AlpTransit and more particularly Hans Ehrbar, Dr. Peter Guntli, Frederico Giovanoli, Dr. Roger Rütli, Beat Frey and Stephan Bucher for giving me access to precious data and helping me understanding them.

I also thank Dr. Peter Bayer for the many nice discussions and for the scientific input.

I will always be grateful to Juergen Hansmann for introducing me to the fields of numerics, scripting and programming. Most of the work done in the context of this thesis would not have been feasible without a basic knowledge in these fields.

Although Fanny Leuenberger-West did not directly contribute to my thesis, she provided unlimited caffeinic and psychological support. Her lab has been from many aspects an oasis to me.

I also want to thank Bernadette Würsch and Tanja Schriber for their care and Dr. Werner Balderer for his support.

I thank all my colleagues of the engineering geology group; just for being themselves.

I thank my parents and friends for being around and supporting me.

Finally, let Santa Barbara be praised for letting me through...

Contents

Acknowledgements.....	1
Contents.....	3
List of figures.....	7
List of tables.....	10
Summary.....	11
Résumé.....	13
1. Introduction	15
1.1. Study motivation.....	15
1.2. Study objectives.....	15
1.3. Structure and content of this thesis.....	16
2. Hydraulic conductivity distribution in crystalline rocks, derived from inflows to tunnels and galleries in the Central Alps, Switzerland	17
2.1. Abstract.....	17
2.2. Introduction.....	18
2.2.1. Tunnel inflows.....	18
2.2.2. Flow in fractured rocks.....	19
2.2.3. Study motivation and objectives.....	20
2.2.4. Location and geological setting of the study area.....	21
2.3. Data set description.....	23
2.3.1. Data sources.....	23
2.3.2. Data base parameters, and data processing and reliability.....	23
2.3.3. Exceptionally high tunnel inflow rates.....	26
2.4. Statistical distributions of tunnel inflow rates.....	28
2.4.1. Inflow rate distribution as a function of geological unit.....	28
2.4.2. Inflow rate distribution as a function of depth.....	30
2.4.3. Inflow spacing distribution along tunnels.....	31
2.5. Major parameters controlling tunnel inflows.....	32
2.5.1. Tectonic overprint.....	32
2.5.2. Topography and unstable slopes.....	33
2.5.3. Depth and lithology.....	33
2.6. Fracture transmissivities.....	34
2.6.1. Data processing and transmissivity models.....	34
2.6.2. Results.....	35
2.7. Rock mass effective hydraulic conductivity.....	37

2.7.1.	Data processing and conductivity models.....	37
2.7.2.	Results	38
2.8.	Discussion	39
2.8.1.	Tunnel inflow distribution and variability.....	39
2.8.2.	Uncertainties in transmissivity and hydraulic conductivity estimations.....	40
2.8.3.	Transmissivity and effective hydraulic conductivity distribution.....	42
2.8.4.	Comparison with other studies.....	43
2.9.	Summary and conclusions.....	45
2.10.	Acknowledgements	47
2.11.	Appendix 1: Notation	48
2.12.	Appendix 2: Water vapor flow rate derivation according to the Ideal Gas Law.....	49
2.13.	References.....	50
2.14.	Tables.....	56
2.15.	Figures	66
3.	Analysis of inflow rates to pre-drillings of Gotthard Base Tunnel (Sedrun section, Switzerland)	84
3.1.	Abstract.....	84
3.2.	Introduction.....	84
3.3.	Tunnel description and geologic settings.....	86
3.3.1.	General GBT settings	86
3.3.2.	GBT Sedrun section	86
3.3.3.	Tectonic units.....	87
3.4.	Pre-drillings description.....	88
3.4.1.	Pre-drilling types.....	88
3.4.2.	Borehole inflow logging.....	88
3.4.3.	Water temperature and pore-pressure	89
3.5.	Quantitative analysis of pre-drilling inflows.....	89
3.5.1.	Analytical solutions.....	89
3.5.2.	Parameter processing and probability density functions.....	91
3.6.	Results	95
3.6.1.	Conductivity of the main fault zones.....	99
3.6.2.	Correlation along a singular tube and between the two tubes	100
3.6.3.	K-distribution.....	100
3.7.	Discussion	100

3.7.1.	Limitations related to the applied flow model	100
3.7.2.	Limitations related to uncertain input parameters	101
3.7.3.	Conductive structures.....	102
3.7.4.	General K-distribution	103
3.7.5.	Representativeness of the studied section	103
3.8.	Conclusion	104
3.9.	Acknowledgements	104
3.10.	References.....	105
3.11.	Figures	107
4.	Influence of hydraulic heterogeneity on transient tunnel inflows	118
4.1.	Abstract.....	118
4.2.	Introduction.....	118
4.3.	Hydrogeologic setting of the Gotthard Base Tunnel study section.....	120
4.4.	Observed transient inflow rates to the Gotthard Base Tunnel test section.....	121
4.5.	Generic numerical simulations (box model).....	123
4.5.1.	Numerical code description.....	123
4.5.2.	Box model description	124
4.5.3.	Homogeneous-K box model description and results.....	124
4.5.4.	Heterogeneous-K box model description and results.....	125
4.6.	Numerical simulations of the Gotthard Base Tunnel.....	125
4.6.1.	General model settings.....	126
4.6.2.	Homogeneous K GBT model	127
4.6.3.	Depth dependent K GBT model	128
4.6.4.	Continuous fault zone GBT model	128
4.6.5.	Stochastic hydraulic conductivity GBT model	129
4.7.	Discussion	130
4.7.1.	Study limitations	130
4.7.2.	Impact of the spatial distribution of hydraulic conductivity.....	131
4.7.3.	Impact of the excavation speed	133
4.7.4.	Adequacy of the different models in the context of the GBT.....	134
4.7.5.	Overestimation of tunnel inflow rates	135
4.8.	Conclusion	135
4.9.	Acknowledgments.....	137
4.10.	Appendix: Hydraulic conductivity derivation for fractional flow dimensions.....	138

4.11. References.....	140
4.12. Figures	143
5. Concluding remarks	166
Curriculum vitae	168

List of figures

Figure 2-1 Sketch of Switzerland showing the perimeter of the study area.....	66
Figure 2-2 Map of the study area	67
Figure 2-3 Inflow data plots.....	68
Figure 2-4 Histogram showing dripping inflow rates and continuous inflow rates for all geologic units.....	71
Figure 2-5 Histogram showing dripping and continuous inflow rates for all geologic units.....	72
Figure 2-6 Histogram showing dripping inflow rates and continuous inflow rates for each geologic unit.....	72
Figure 2-7 All geologic units: Distribution of the inflow rate with depth.....	73
Figure 2-8 Individual geologic units: Distribution of the inflow rate with depth....	74
Figure 2-9 Continuous inflow spacing distribution	75
Figure 2-10 Gotthard SBB railway tunnel inflow spacing distribution.....	75
Figure 2-11 Goeschenen pressure drift inflow spacing distribution.....	75
Figure 2-12 EPM (equivalent porous medium) transmissivity model sketches and formulas.....	76
Figure 2-13 Histogram showing transmissivity values derived from dripping inflow rates and continuous inflow rates for all geologic units.....	76
Figure 2-14 Histogram showing transmissivity values derived from dripping inflow rates and continuous inflow rates for all geologic units.....	77
Figure 2-15 Transmissivity cumulative plot for Gotthard A2 security gallery.....	77
Figure 2-16 Histograms showing transmissivity values derived from the dripping inflow rates and from the continuous inflow rates for each geologic unit.....	78
Figure 2-17 Plots of the transmissivity values versus depth	79
Figure 2-18 Transmissivity distribution along selected tunnels.....	80
Figure 2-19 EPM hydraulic conductivity model sketches and formulas	81
Figure 2-20 Plots of the hydraulic conductivity values versus depth	82
Figure 2-21 Plots of simulated transmissivity distributions	83
Figure 3-1 Location of Gotthard Base Tunnel.....	107
Figure 3-2 Geological cross-section along Gotthard Base Tunnel starting in Erstfeld and ending in Bodio	108
Figure 3-3 Location of the studied tunnel section	109
Figure 3-4 Geological cross-section along the studied tunnel section.....	110

Figure 3-5 Depth, water temperature and rock temperature along the studied section	111
Figure 3-6 Tunnel advance, measured and interpolated pore-pressure values and measured pore-pressure distribution.....	112
Figure 3-7 Sketch of a cored borehole.....	112
Figure 3-8 Total drilling duration.....	113
Figure 3-9 Example of parameter distributions generated by Monte Carlo simulation.....	113
Figure 3-10 Contribution to the variance of the transmissivity from diverse parameters.....	114
Figure 3-11 Distribution of the transmissivity and major faults along the studied section for East and West tube	114
Figure 3-12 Raw K-values and K-envelope for East and West tube.....	115
Figure 3-13 Geometric average of the K-envelope higher and lower bounds for East and West tube	115
Figure 3-14 Processed K-distribution along tunnel for East and West tube	116
Figure 3-15 Semi-variograms of the K-values along the two tunnel tubes.....	116
Figure 3-16 Hydraulic conductivity distribution	117
Figure 3-17 Variance versus interval length.....	117
Figure 4-1 Location of Gotthard Base Tunnel.....	143
Figure 4-2 Studied section location.....	144
Figure 4-3 Cross-section along the studied section of Gotthard Base Tunnel.....	145
Figure 4-4 Tunnel inflow measured rates	146
Figure 4-5 Sketch of the box model	147
Figure 4-6 Modeled rate in function of the tunnel/borehole radius	147
Figure 4-7 Modeled tunnel inflow rates in function of cell size	148
Figure 4-8 Modeled rates of the heterogeneous box model.....	148
Figure 4-9 Impact of heterogeneous hydraulic conductivity on flow dimension.....	149
Figure 4-10 GBT model NE-SW view	150
Figure 4-11 GBT model with tunnel NW-SE view	151
Figure 4-12 Relation between time step and excavation step.....	151
Figure 4-13 "Altkristallin" Hydraulic conductivity distribution with depth	152
Figure 4-14 Measured rates and modeled rates of the GBT homogeneous K model.....	153
Figure 4-15 Measured rates and modeled rates of the GBT depth-dependent K model.....	154

Figure 4-16 Comparison of the modeled rates of the constant and depth-dependent K models	155
Figure 4-17 Comparison of the steady-state water table elevation of the constant and depth-dependent K models.....	156
Figure 4-18 Cross-sections of the continuous fault zone model.....	156
Figure 4-19 Impact of transmissive planes on modeled rates	157
Figure 4-20 Impact of transmissive planes on modeled water table positions.....	158
Figure 4-21 Back-calculated hydraulic conductivity distribution along each tunnel tube.....	159
Figure 4-22 Empirical variograms of hydraulic conductivity	159
Figure 4-23 Cross-section through an upscaled hydraulic conductivity field	160
Figure 4-24 Cross-sections through the stochastic model	161
Figure 4-25 Stochastic model with isotropic 1000 m correlation length and higher bound K-values	161
Figure 4-26 Stochastic model with isotropic 1000 m correlation length and lower bound K-values	162
Figure 4-27 Stochastic model with isotropic 500 m correlation length and higher bound K-values	162
Figure 4-28 Stochastic model with isotropic 500 m correlation length and lower bound K-values	163
Figure 4-29 Stochastic model with isotropic 250 m correlation length and higher bound K-values	163
Figure 4-30 Stochastic model with isotropic 250 m correlation length and lower bound K-values	164
Figure 4-31 Comparison of the modeled rates of the homogeneous K and stochastic models (one realization).....	164
Figure 4-32 Excavation speed impact.....	165

List of tables

Table 2-1 References to unpublished reports.....	56
Table 2-2 Basic tunnel and gallery information: Furka base tunnel, Gottard SBB, Gotthard A2 highway tunnel.....	58
Table 2-3 Basic tunnel and gallery information: KW Amsteg, KW	59
Table 2-4 Basic tunnel and gallery information: KW Goeschenen and KW Wassen	60
Table 2-5 Basic tunnel and gallery information: Gas Transit.....	61
Table 2-6 Basic tunnel and gallery information: KW Oberhasli and KW Ritom	62
Table 2-7 Basic tunnel and gallery information: KW Vorderrhein	63
Table 2-8 Geological units and their corresponding abbreviations.....	64
Table 2-9 Air water vapor content parameters and results.....	65
Table 3-1 storage values in hard fractured rocks of the Alps (FZ: fault zone)	94
Table 3-2 Mean K-value inside fault zones versus overall mean K-value	99
Table 3-3 Correlation coefficients between the K-values of the two tunnel tubes	100
Table 4-1 Monitoring section details	123
Table 4-2 Typical infiltration rate values from other studies located in the Central Swiss Alps.....	126

Summary

In a first paper (chapter 2), inflow data from 23 tunnels and galleries located in the Aar and Gotthard massifs of the Swiss Alps are analyzed with the objective to (1) understand the spatial distribution of groundwater flow in crystalline basement rocks, (2) to assess the dependency of tunnel inflow rate on depth, tectonic overprint, and lithology, and (3) to derive large scale transmissivity and hydraulic conductivity values.

Brittle tectonic overprint is shown to be the principal parameter regulating inflow rate and dominates over overburden and lithology. The highest early time inflow rate is 1300 l/s and has been reported from a shallow hydropower gallery intersecting a 200 m wide cataclastic fault zone. The derived log-normal transmissivity distributions are based on a total of 1361 tunnel intervals with a length of 100 m. Such interval transmissivities range between 10^{-9} and 10^{-1} m²/s within the first 200 to 400 m of overburden and between 10^{-9} and 10^{-4} m²/s in the depth interval of 400-1500 m below ground surface. Outside brittle fault zones, a trend of decreasing transmissivity/hydraulic conductivity with increasing overburden is observed for some schistous and gneissic geological units whereas no trend is identified for the granitic units.

In a second paper (chapter 3), inflow data from a systematic pre-drilling (drilling made ahead of the excavation front) campaign undertaken during the excavation of the Sedrun lot of Gotthard Base Tunnel are analyzed. The section covered by the systematic drilling campaign extends over 5 km. The depth of the section ranges from 897 to 2026 m and the lithology mainly consists of various gneisses. The pre-drillings include 30 cored and 94 destructive drillings distributed along the two parallel tubes constituting the tunnel. The length of the boreholes ranges from 17.5 to 358.5 m.

A new methodology to quantitatively analyze inflow and pressure data from pre-drillings for transmissivity and hydraulic conductivity estimation is presented. Hydraulic conductivity values of 50 m long sections of the tunnel are back-calculated from inflow rate and pressure measurements from pre-drillings, using the Jacob and Lohman solution for the transient inflow rate to a well of constant drawdown in a confined aquifer.

Uncertainties with respect to the derived hydraulic conductivity values are estimated through Monte Carlo analysis. In the context of the study the uncertainty mainly comes from uncertainties related to specific storage and pore-

pressure values. Derived hydraulic conductivity values range from 10^{-10} to 10^{-6} m/s. The analysis of the distribution of hydraulic conductivity along the two tubes constituting the tunnel shows that the conductive intervals are located independently from the position of major fault zones. Furthermore the correlation between the hydraulic conductivity values of each tunnel tube is weak, suggesting a limited extend for the conductive structures.

The prediction and the interpretation of the transient inflow rate to a tunnel during its excavation are difficult tasks since variations of the rock mass hydraulic conductivity and excavation speed can both lead to variations in the inflow. In a third paper (chapter 4), the impact of the spatial hydraulic conductivity distribution on transient tunnel inflows is investigated.

Two types of finite element models are implemented with the HydroGeoSphere numerical code. The first, a simple box model, simulates the instantaneous excavation of a tunnel with varying types of hydraulic conductivity distributions. The second model simulates the transient excavation of Gotthard Base Tunnel (GBT) South of the Sedrun shaft. Hydraulic conductivity values back-calculated from the inflow rate into boreholes belonging to a systematic pre-drilling campaign conducted along a 5 kilometer long section of the tunnel are used as input to the model.

The box model shows that individual inflows exhibiting non-radial flow dimensions may result of the channeling induced by a heterogeneous hydraulic conductivity field. The GBT model, implemented with four types of hydraulic conductivity distribution (constant, depth-dependent, constant with continuous fault planes and stochastic continuum) show that the stochastic model yields the best simulation of the inflow rate to a tunnel section during its excavation.

Résumé

Le premier article (chapitre 2) porte sur l'analyse de données relatives aux venues d'eau rapportées de 23 galeries et tunnels situés dans les massifs suisses de l'Aar et du Gotthard. Les objectifs sont (1) l'étude de la distribution spatiale des écoulements dans les roches cristallines du socle, (2) l'étude de la variation du débit des venues d'eau en fonction de la profondeur, de l'empreinte tectonique et de la lithologie, et (3) le calcul de valeurs de transmissivité et de conductivité hydrauliques.

L'empreinte tectonique constitue le facteur dominant pour le débit des venues d'eau. La profondeur et la lithologie, dans une moindre mesure, jouent aussi un rôle. Le plus important débit mesuré (1300 l/s, débit initial) provient d'une galerie hydroélectrique de faible profondeur excavée à travers une zone de faille de 200 m d'épaisseur. La distribution log-normale de la conductivité hydraulique est basée sur l'interprétation des débits rapportés pour des sections de tunnel/galerie d'une longueur de 100 m. Les valeurs de transmissivité varient de 10^{-9} à 10^{-1} m/s jusqu'à une profondeur de 200 à 400 m et de 10^{-9} à 10^{-4} m/s de 400 à 1500 m de profondeur. En dehors des zones de faille, la conductivité hydraulique tend à décroître avec l'augmentation de la profondeur dans les unités lithologiques schisteuses et gneissiques alors qu'elle semble indépendante de la profondeur dans les unités granitiques.

Un second article (chapitre 3), présente l'analyse de données de débits issues d'une campagne systématique de forages à l'avancer (pré-forages), entreprise lors de l'excavation du tronçon de Sedrun appartenant au tunnel de base du Gotthard. La section couverte par la campagne systématique de forage a une longueur de 5 km et une profondeur qui augmente de 897 à 2026 m du Nord vers le Sud. D'un point de vue lithologique la roche encaissante est principalement constituée de divers gneiss. La campagne de pré-forage inclu 30 forages carotés et 94 forages destructifs distribués le long des deux tubes parallèles qui constitue le tunnel. La longueur des forages varie de 17.5 à 358.5 m.

Une nouvelle méthode permettant l'analyse quantitative de données de débits et de pression de pore issues de forages à l'avancer est proposée. La méthode permet la dérivation de valeurs de conductivité hydraulique, par intervalles de 50 m, en interprétant les débits mesurés en forage à l'aide de la solution analytique de Jacob et Lohman.

L'incertitude liée aux valeurs de conductivité hydraulique dérivées est estimée par le biais d'une analyse de Monte Carlo. Dans le cadre de cette étude, l'incertitude sur la conductivité dépend majoritairement de l'incertitude liée à deux paramètres: le coefficient d'emmagasinement et la pression de pore. Les valeurs de conductivité dérivées s'étendent de 10^{-10} à 10^{-6} m/s. L'analyse de la distribution de ces valeurs le long des deux tubes constituant le tunnel de base du Gotthard montre que les valeurs de conductivité élevée sont situées indépendamment de la position des failles principales. De plus, la corrélation faible des valeurs d'un tube à l'autre suggère une extension limitée des structures favorisant la conductivité.

La prédiction et l'interprétation du débit transitoire mesuré en tunnel durant l'excavation sont ardues. Les variations de paramètres telles que la conductivité des roches encaissantes ou la vitesse d'excavation mènent tout deux à une variation du débit le long du tunnel. Dans le dernier article (chapitre 4), les auteurs investiguent l'impact de la distribution spatiale de la conductivité hydraulique sur les débits transitoires mesurés en tunnel.

Dans cet objectif, deux types de modèle à éléments finis ont été élaborés avec le code HydroGeoSphere. Le premier, un modèle basique de forme cubique, simule l'excavation instantanée d'un tunnel avec diverses distributions de la conductivité hydraulique. Le second modèle simule l'excavation du Tunnel de Base du Gotthard (GBT) le long d'une section de 5 km. Les valeurs de conductivité calculées à partir des débits mesurés en forages présentées dans le second article sont incorporées au modèle.

Le modèle cubique montre que la distribution hétérogène de la conductivité hydraulique induit une canalisation de l'écoulement qui va de pair avec une diminution de la dimension de l'écoulement. La simulation de l'excavation du Tunnel de Base du Gotthard avec quatre types de distribution de la conductivité hydraulique différents (constante, fonction de la profondeur, constante avec plans de faille continus et continuum stochastique) montre que la meilleure reproduction du débit cumulé provenant d'une section de tunnel lors de son excavation est obtenue avec le modèle stochastique.

1. Introduction

1.1. Study motivation

In the early 90' and the context of the Gotthard Base Tunnel inflow predictions, all data related to inflow to tunnels and galleries located in the Aar and Gotthard massifs have been compiled and interpreted (Löw, et al., 1996). This large dataset includes inflow data from 23 tunnels and galleries constituting a total length of 136 km.

In 2006 and the context of the search for radioactive waste disposal host rocks in Switzerland, Nagra (Nationale Genossenschaft für die Lagerung radioaktiver Abfälle - National Cooperative for the Disposal of Radioactive Waste) got interested in this dataset. Nagra was particularly interested in the medium to large scale hydraulic conductivity distribution in the Aar and Gotthard massifs; permeability being the main criterion for host rock selection.

The scientific value of this dataset and Nagra's needs motivated the start of the present PhD research project with the reinterpretation of the regional dataset of tunnel inflows. This gave rise to a large scale study on the distribution of hydraulic conductivity in Aar and Gotthard massifs published in the Hydrogeology Journal (Masset and Loew, 2010).

In a second phase of the PhD, inflow data collected during a systematic pre-drilling campaign (boreholes drilled ahead of the excavation front) conducted along a 5 km long section of Gotthard Base Tunnel, between 2004 and 2010, allowed to study the local smaller scale distribution of hydraulic conductivity in greater detail.

Finally, the availability of transient tunnel inflow rates to the same tunnel section of the Gotthard Base Tunnel motivated the elaboration of a 3D transient finite element model. This model was used to validate the hydraulic conductivity distribution from the regional and local studies, and test different hypotheses about the relationship between hydraulic conductivity distribution and transient tunnel inflow rates.

1.2. Study objectives

The main objectives of the present thesis are:

- The derivation of the regional hydraulic conductivity distribution from the back-analysis of inflow rates to a large number of historic underground excavations located in Aar and Gotthard massifs
- The derivation of the local hydraulic conductivity distribution from the systematic analysis of pre-drillings inflow rates and pore pressures
- The analysis of the multi-scale spatial distribution of hydraulic conductivity in different lithologies and tectonic settings of crystalline rocks from the Aar and Gotthard massifs
- The validation of the back-calculated hydraulic conductivity values for tunnel inflow predictions
- The assessment of the impact of the spatial distribution of hydraulic conductivity or the excavation speed on tunnel transient inflow rates

1.3. Structure and content of this thesis

The present thesis is divided into five chapters. The first and the last chapters consist of general introduction and conclusion. Chapters 2-4 are formatted as individual paper manuscripts.

The first paper, entitled "Hydraulic conductivity distribution in crystalline rocks, derived from inflows to tunnels and galleries in the Central Alps, Switzerland" (Masset and Loew 2010), presents the results of the above mentioned regional study. The second paper, entitled "Analysis of inflow rates to pre-drillings of Gotthard Base Tunnel (Sedrun section, Switzerland)", presents the results of the local study and the last paper, entitled "Influence of hydraulic heterogeneity on transient tunnel inflows", deals with the modeling and analysis of transient inflows to the Gotthard Base Tunnel.

2. Hydraulic conductivity distribution in crystalline rocks, derived from inflows to tunnels and galleries in the Central Alps, Switzerland

Olivier Masset and Simon Loew

2.1. Abstract

Inflow data from 23 tunnels and galleries, 136 km in length and located in the Aar and Gotthard massifs of the Swiss Alps, have been analyzed with the objective (1) to understand the 3-dimensional spatial distribution of groundwater flow in crystalline basement rocks, (2) to assess the dependency of tunnel inflow rate on depth, tectonic overprint, and lithology, and (3) to derive the distribution of fracture transmissivity and effective hydraulic conductivity at the 100-m scale.

Brittle tectonic overprint is shown to be the principal parameter regulating inflow rate and dominates over depth and lithology. The highest early time inflow rate is 1,300 l/s and has been reported from a shallow hydropower gallery intersecting a 200-m wide cataclastic fault zone. The derived log-normal transmissivity distribution is based on 1,361 tunnel intervals with a length of 100m. Such interval transmissivities range between 10^{-9} and $10^{-1} \text{m}^2/\text{s}$ within the first 200–400 m of depth and between 10^{-9} and $10^{-4} \text{m}^2/\text{s}$ in the depth interval of 400–1,500m below ground surface. Outside brittle fault zones, a trend of decreasing transmissivity/ hydraulic conductivity with increasing depth is observed for some schistous and gneissic geological units, whereas no trend is identified for the granitic units.

Keywords: hydraulic properties, crystalline rocks, fractured rocks, tunnel, Switzerland

2.2. Introduction

2.2.1. Tunnel inflows

Several researchers have focused on tunnel inflow phenomena. Among the different aspects of the phenomena considered are the inflow distribution, the inflow rate transient behavior and the source of inflows. One of the most popular study approaches, whatever the aspect considered, is the comparison of measured inflow data with modeled inflows in order to back calculate hydrogeological parameters. For example, Zhang and Franklin (1993) compiled inflow data from different tunnels in different types of rock and compared them with analytical and numerical models, and Hwang and Lu (2007) modeled inflow transient behavior and found it to be in agreement with the general trend of measured inflow data.

The analysis of tunnel inflow data yields important information about the spatial distribution of groundwater flow at various scales and the hydraulic properties of rock masses. Deriving large-scale hydrogeological properties of crystalline rocks is of relevance for the site selection of waste repositories, for geothermal and hydrocarbon reservoir exploitation, for groundwater resource management, and for tunneling. Standard borehole tests carried out from the ground surface only yield local hydraulic properties. In comparison, the rock mass volume affected by the pressure disturbance caused by a deep underground excavation is larger. This is due to the strong pressure drawdown caused by a deep draining tunnel, the large tunnel diameter, and the long drainage duration. This implies that the analysis of tunnel inflows provides estimates of hydraulic properties relevant for a large-scale investigation. In addition to this large-scale investigation, tunnels are often relatively long "sampling lines". In the case of detailed geological and hydrogeological tunnel observations, not only major inflows from faults and fault zones but also minor inflows from the fractured rock mass can be studied. This implies that tunnel observations can also lead to multi-scale information about flow in fractured rocks (Masset and Loew 2007).

Back analyses of tunnel inflows rely on the same principles and models like forward predictions of tunnel inflows. Several simple mathematical models have been published that can explain or predict the temporal behavior of groundwater inflows to tunnels in rocks assuming homogeneous hydraulic conductivities and a Darcy type of groundwater flow. Most of these models assume two-dimensional (2D) flow in a plane perpendicular to the tunnel axis and a constant head

boundary condition at the tunnel wall, which is often assumed to have a circular geometry. For a deep tunnel (tunnel radius $r \ll$ depth of tunnel below water table) in a homogeneous rock mass with a linear constant pressure boundary at the surface (for example a lake or a prolific aquifer), the steady state inflow rate Q into a tunnel segment of length L can be described by the well known formula reported by Goodman et al. (1965):

$$2-1 \quad Q = \frac{2\pi KL(h_e - h_t)}{2.3 \log(2(h_e - h_t) / r)}$$

where K [m/s] is the effective hydraulic conductivity (or equivalent porous medium hydraulic conductivity) in the (vertical) plane of flow, $h_e - h_t$ [m] is the tunnel drawdown (i.e. the difference between the static formation head and the tunnel head), and r [m] is the tunnel radius (see Appendix 1). Lei (1999, 2000) derived an analytical solution for the steady-state head field and groundwater flow around a tunnel close to the surface. Zhang and Franklin (1993) proposed another analytical solution to model an assumed exponential decrease of the hydraulic conductivity with depth. El Tani (1999) gives approximate solutions for steady-state inflow to tunnels with elliptical or square cross-sections.

2.2.2. Flow in fractured rocks

According to many authors such as Zhao (1998), groundwater flow in crystalline rock masses is controlled by flow in discontinuities such as faults and fractures. The prediction of inflows to tunnels in fractured crystalline rocks is a difficult task, because the permeability distribution of fractured crystalline rocks is strongly heterogeneous and ranges over several orders of magnitude. In addition, only a few highly conductive pathways control the total groundwater flow on different scales in the rock mass surrounding a deep tunnel (Loew 2001; Long et al. 1991). In the past, several researchers have attempted to model heterogeneous flow in fractured rock masses with discrete fracture network models (Cacas et al. 1990; Davy et al. 2006; Wang et al. 2001). This approach assumes that the fracture network geometry is known or can be rebuilt from borehole fracture data or surface-fracture trace maps. In such cases, the transmissivity distribution of the fracture sets that form a conductive network can be obtained by back analysis of distributed tunnel inflow data (Molinero et al. 2002).

Most of the time, the fractures are assumed to have a constant hydraulic aperture and, thus, a constant transmissivity. This is of course a simplification,

because field observations suggest that faults or large joints have complex internal geometries. An alternative is to assign each fracture a transmissivity distribution instead of a constant transmissivity value (Mourzenko et al. 1996, 1999). In that case, the transmissivity distribution is derived from the geometric fracture aperture distribution. Unfortunately, no data concerning fracture aperture distribution are available for real cases at site scales. Moreover, faults are, most of the time, filled with crushed material and their width may vary drastically, even at the scale of a tunnel diameter, which renders the transmissivity distribution within a fault difficult to assess.

2.2.3. Study motivation and objectives

Since the construction of the Gotthard railway tunnel in the years 1872–1880, numerous underground excavations have been constructed in the crystalline basement rocks of the Aar and Gotthard massifs of the central Swiss Alps. These underground excavations include several train and road tunnels for N–S and W–E connections through the Swiss Alps, numerous hydropower drifts and galleries, and some military installations. The geological findings of most of these underground constructions are described in unpublished technical reports; only a few observations are published (Keller and Schneider 1982; Keller et al. 1987; Klemenz 1974). A reference list of the unpublished reports can be found in Table 1. The unpublished reports include the locations and rates of groundwater inflows, geological cross-sections including lithology, tectonic unit, major fractures and faults, and other geotechnical properties. While most military reports are still confidential, a great number of unpublished reports dealing with traffic and hydropower constructions are available for scientific purposes. The total length of the underground excavations which have accessible documentation is 136 km. A first attempt to quantitatively analyze these observations has been made for the design of the Gotthard Base Tunnel (Loew et al. 2000; Löw et al. 1996). This study presents a complete description of this unique data set and an analysis of the following hydrogeological key properties of fractured crystalline rocks in the Aar and Gotthard massifs:

- Distribution of inflow frequency and rate as a function of depth and lithology
- Spacing distribution of different types of tunnel inflows
- Impact of brittle faulting and fracturing on tunnel inflows

- Regional variability of preferential groundwater pathways and controlling parameters
- Estimate of the distribution of fracture transmissivity
- Estimate of the distribution of rock mass effective hydraulic conductivity

2.2.4. Location and geological setting of the study area

The study area is located in the central Aar and Gotthard massifs of the Swiss Alps (Figures 1 and 2). There are distinct tectonic, lithologic and metamorphic differences between the Aar and Gotthard massifs, which are explained in the following.

Ground elevation in the central Aar massif ranges from 475 m (Erstfeld) to 3,085 m (Piz Giuv) above mean sea level. The Aar massif is striking NE, is 115 km long, 23 km wide and covers an area of about 2,000 km². It is composed of pre-Variscan polyorogenic and polymetamorphic basement rocks (primarily gneisses, schists and migmatites) intruded by late Variscan magmatic rocks (granites, diorites, syenites and in a smaller proportion vulcanites, aplites and lamprophyres) and covered by Permian and Mesozoic sediments (Abrecht 1994; Labhart 1977).

During the Tertiary alpine collision, the Aar massif was strongly compressed and thrust in the NW direction. In the north, the sedimentary cover was folded and thrust onto the basement rocks, and finally the southern margin was turned in a nearly upright position (Schmid et al. 1996; Steck 1968a; Steck and Hunziker 1994). The Tertiary collision led to an Alpine foliation and heterogeneous ductile deformations at all scales. The greenschist facies Alpine metamorphic overprint increases from NW to SE (Choukroune and Gapais 1983; Frey et al. 1980; Labhart 1977; Laws 2001; Meyer et al. 1989; Steck 1984). Presumably since the Miocene, ductile deformations have been superimposed by weak brittle deformations and a large-scale uplift in the order of 0.5–1.0 mm/year takes place (Kohl et al. 2000). This resulted in the formation of small shear fractures and joint systems (Laws et al. 2000). According to Laws (2001) and Frei and Löw (2001), steeply dipping ENE–WSW striking shear zones of the study area are primarily ductile but more fracture-bearing than the host rock. This is supported by recent observations in the Gotthard Base Tunnel (Frei and Breitenmoser 2006).

The Gotthard massif, which is also striking NE, is 80 km long and 12 km wide and covers an area of 580 km² (Figure 2). Ground elevation ranges from

1,147 m (Andermatt) to 2,963 m (Pizzo Lucendo). The Gotthard massif is composed of a pre-Variscan polyorogenic and polymetamorphic basement (mainly gneisses, schists, migmatites and amphibolites) intruded during two phases by Variscan granitoids (Labhart 1999). The Gotthard massif is bordered in the north by a stratigraphic contact with Permo-carboniferous and Mesozoic sediments of the Urseren Garvera Zone (Wyss 1986). This northern contact is locally strongly tectonized. In the south, the Gotthard massif is in contact with steeply dipping para-autochthonous metasediments (schists, carbonate, and gypsum/anhydrite) of the Piora and Nufenen zones (Herwegh and Pfiffner 1999).

During the Tertiary alpine collision, the Gotthard massif was affected by greenschist facies metamorphism with an increasing N-S grade. At its southern boundary, amphibolitic facies conditions were reached (Frey et al. 1980; Labhart 1999). The formation of a penetrative Alpine foliation and of steeply dipping ductile shear zones that mainly strike NE-SW occurred in a compressive NW-SE directed stress field (Marquer 1990; Steck 1968b; Zangerl et al. 2006; Zangerl 2003). Towards the end of the Tertiary collision, the deformation mode gradually evolved from ductile to brittle. Analyses of the interrelationship between brittle fault zones and meso-scale fractures indicate that during an early stage of brittle faulting, the stress regime changed from compression to strike-slip (Zangerl 2003; Zangerl et al. 2006). The stress conditions prevailing during the formation of these brittle faults are not well constrained, but suggest a horizontal maximum principle effective stress direction striking about NE-SW and a minimum compressive principal stress direction in NW-SE direction. According to Lützenkirchen (2002), brittle faulting in the Gotthard massif occurred preferentially along pre-existing ductile shear zones under temperatures in the range of 250–200°C. Compared to the Central Aar massif, the Central Gotthard massif clearly shows more abundant and intensive brittle deformations along pre-existing joints and ductile faults (Zangerl et al. 2006).

Lützenkirchen (2002) demonstrated that in the Bedretto leg of the Furka base tunnel (Switzerland,) most of the deep inflows are related to the damage zones around fault zones, and that the flow contributed by individual joints not related to fault zones is negligible. He also observed that brittle faulting in the Gotthard massif often overprinted ductile shear zones and that the fault zones with higher flow rates always showed slickenside striations on shear fractures. Lützenkirchen (2002) divided fault zones and shear zones into six different types:

1. Ductile shear zones showing mylonitic and/or densely spaced foliation planes
2. Ductile shear zones overprinting lamprophyre and aplitic dikes
3. Brittle-ductile shear zones intensely fractured within ductile shear zones
4. Brittle-ductile shear zones, wide, intensely fractured outside ductile shear zones
5. Brittle fracture zones
6. Brittle fault zones, narrow, intensely fractured and deformed

This showed that 90% of the estimated total flow rate to the deeper tunnel section was related to types 4 and 5. This observation is also compatible with the majority of inflows in the entire Gotthard massif study area.

2.3. Data set description

2.3.1. Data sources

The main part of the data used for the present study comes from the geological survey of 23 tunnels and galleries located in the Aar and the Gotthard massifs. References for the data sources of the individual tunnels are given in Tables 2–7. In addition to these project reports, this study also includes important data and findings from four PhD dissertations completed at the Swiss Federal Institute of Technology (ETH Zurich) in the same study area (Laws 2001; Lützenkirchen 2002; Offerdinger 2001; Zangerl 2003). These research investigations give more detailed insight into the type and properties of water-conducting structures in the Aar and Gotthard massifs.

2.3.2. Data base parameters, and data processing and reliability

Tables 2–7 and Figure 3 give the basic information for each tunnel or gallery which has been considered in the present study. The oldest document used is an unpublished report from Stapff (1882, see Table 1) on the construction of the Gotthard SBB (Schweizerische Bundesbahnen, Swiss Federal Railways) railway tunnel and the most recent is a report from Schneider 1985, unpublished report (see Table 1) on the Furka base tunnel. Data from more recent tunnel constructions in the area, e.g. the Gotthard Base Tunnel, or the Grimsel hydropower system expansions (Aar massif) will be discussed in detail in subsequent papers. The quality and type of documentation from more than 100

years of underground construction is highly heterogeneous. For this reason, and in order to compare continuous parameters (e.g. depth) with discontinuous parameters (e.g. inflow rate), data had to be homogenized before being analyzed. This was mainly done by integrating each parameter over 100-m-long tunnel sections. The integration process has mainly two consequences. It first smoothes the parameters' variability along the different tunnels, and second, decreases the variance of the different parameter distribution.

Figure 3 shows the main hydrogeological parameters of each tunnel and gallery which have been compiled in a data base in a standardized format. All plots show the geological units (abbreviations according to Table 8) and the location of their boundaries, the number of dripping zones (divided into light or heavy dripping zone class) per 100-m interval, continuous tunnel inflow rates per 100-m interval, the depth and the angle between the main rock fabric (i.e. alpine foliation) and the tunnel axis. The continuous rate term is used as opposed to the dripping rate term. It refers to inflows that present a continuous water jet, whereas dripping rates are related to smaller inflows that have been reported as dripping zones from the tunnels. The key properties for further inflow analysis (Tables 2–7 and Figure 3) are explained in the following.

Date of the tunnel excavation and hydrogeological survey

The survey date reported in Tables 2–7 is the date of the inflow rate measurements. The delay is the estimated time difference between the excavation date and the inflow measurement date at a given location along the tunnel. This delay is important information for the quantitative inflow rate analysis, but the delays are often not known or only roughly estimated (Tables 2–7). In most cases the delay is several weeks to months, i.e. most of the rates reported in the data base and in Figure 3 are close to steady state rates. Exceptions to this rule are discussed later (see section Exceptionally high tunnel inflow rates) and include, for example, the high inflows (110 and 150 l/s) to the Security gallery of the Gotthard A2 tunnel at Tm 9935 and 9910, where inflow rates, as measured by Lützenkirchen (2002), are on the order of 8 l/s. Tm stands for tunnel meters from a given reference point. In the case of the Gotthard A2 tunnel, the reference point is the northern portal (Figure 3d).

Tunnel geology, location, orientation, elevation and depth

The location of each tunnel and gallery within the Aar and Gotthard massifs, and their elevation, orientation and depth are included in Figures 2 and 3

and in Tables 2–7. The tunnels and galleries are well distributed over the study domain. The majority of the tunnels and galleries have a N–S orientation, i.e. an orientation perpendicular to the main Alpine structures. The portal elevation of each tunnel and gallery ranges between 530 m (KW Amsteg supply gallery) and 2,033 m (KW Lucendro pressure gallery). KW stands for “Kraftwerk” and means power plant in German. The different geological units crossed by each tunnel and gallery are reported in Figures 2 and 3 with abbreviations defined in Table 8 and Figure 2. The geological units relate to different rock types and tectonic units. The geological map has been modified from Labhart (1999). For each tunnel and gallery, the depth has been computed by subtracting the elevation of the gallery from the elevation of the ground surface based on a digital elevation model. The maximum depth ranges between 224 m (Gas Transit pipeline—Urweid drift) and 1,680 m (Gotthard SBB railway tunnel). The depth of every tunnel and gallery is also seen in Figure 3.

Tunnel inflows

The tunnels discussed have hardly ever been grouted (pressures and flow velocities are too high at the tunnel depths considered) and the tunnel inflow rates, therefore, represent induced flows of natural features. Geological and hydrogeological data are heterogeneous because they come from different projects and have been collected by different persons at different times. This is especially true for inflow data which have been reported in basically two different ways. The largest amount of tunnel and gallery inflow has been reported by classes of inflow rate only. A smaller part has been reported by measured or estimated inflow rates. For quantitative analysis, continuous inflows reported by classes of rate have been assigned a mean rate. Tables 2–7 give information about how inflows have been reported for each tunnel and gallery. When reported by classes, the assigned mean rate value assumed for each class is also mentioned. For example, the Gotthard A2 highway tunnel continuous inflows have been reported by three classes: inflows smaller than 0.1 l/s, inflows between 0.1 and 1 l/s and inflows bigger than 1 l/s. Then, inflows from each class have been assigned a mean rate of 0.03, 0.3 and 3 l/s respectively. If possible, when only one class of inflow was reported, the assigned mean rate value has been computed by dividing the cumulate flow at the portal by the number of continuous inflows contributing to the flow. Finally, when no cumulate flow was available, inflows have been assigned mean rate values based on the geometric mean of the class

boundaries, assuming that rate values within a given class are log-normally distributed or, more generally, that inflow rates are log-normally distributed.

When localized inflows become too small for hand measurements of inflow rates with a bucket and watch, i.e. when individual continuous water-jets break down, dripping zones are recorded by the on-site geologists. These dripping zones are sometimes mapped in two classes (heavy and light). Dripping inflows have also been assigned rates according to their class (0.01 and 0.001 l/s).

A rate error has been assumed for each rate value that was used for later transmissivity estimation (Tables 2–7). The assumed error is proportional to the rate and quality of the value that has been reported. The quality of the value is based on the measurement method used and the type of data reported. When the rate has been quantitatively reported, the rate error is assumed to be equal to half of the rate value. When inflows have been reported by classes, the rate error is estimated to be equal to two or three times the rate value.

2.3.3. Exceptionally high tunnel inflow rates

In the tunnels and galleries discussed here, a few exceptionally high singular tunnel inflow rates have been observed. These high inflows have important scientific and practical implications (they control the total inflow rate, the design of drainage measures, and safety considerations); so therefore their geologic and topographic conditions are presented here in detail. Most of these high values are not shown in Figure 3 because they represent initial (early time) inflows which strongly decreased with time. Using them for quantitative analysis would require exact knowledge of the inflow time.

In the Bedretto leg of the Furka base tunnel, up to 57 l/s of water were initially flowing into the tunnel during excavation from Tm 2815 to Tm 2850 in the Rotondo granite (GHG). Based on the descriptions of this tunnel in Keller and Schneider (1982) and Lützenkirchen (2002), this large inflow is related to a brittle fault zone. In the Bedretto gallery, exceptionally high initial inflow rates were also recorded close to the southern portal (up to 130 l/s initially between Tm 180 and Tm 360), where toppling of steeply dipping foliation planes resulted in a strongly increased rock mass hydraulic conductivity (Keller and Schneider 1982). In July 1875, in the Gotthard SBB railway tunnel, after excavation of the first 2,100 m from the southern portal in the Tremola series (GSG), a cumulate inflow rate of 130–350 l/s, taking place in the strongly fractured meta-sediments of the Tremola series, was measured at the portal over a long period of time (October 1873–July

1879). The depth is limited (0– 750 m) and toppling occurs again at ground surface and also at tunnel elevation close to the portal. In the Gotthard A2 security gallery, two initial inflows of 150 l/s (Tm 9935) and 110 l/s (Tm 9910) were encountered at greater depth, occurring in cross-cutting fault zones of the Gamsboden granite (GHG) and were intensively studied by Zangerl et al. (2006) and Lützenkirchen (2002). Today the inflow rate from this tunnel section is about 8 l/s. In the Goeschenen Voralpreuss supply gallery, at Tm 1340 in the Aar granite, an inflow with an initial maximum rate of 140 l/s was reported in a place where the depth is below 500 m. The high (initial?) inflow value of the Furkareuss supply gallery (60 l/s) must be related to the relative close proximity to ground surface, large scale tectonic faulting (Eckart et al. 1983; Steck 1968b), and unloading features observed along the Urseren valley. In the KW Oberhasli Gadmenwasser supply gallery, an early time inflow of 300 l/s was observed in a brittle fault zone of 1-m width in gneisses of the Aar massif (ANG). The inflow location has a depth of about 800 m. In KW Ritom Unteralpreuss supply gallery, 140 l/s was initially flushed out of a clayey joint when it was intersected by the excavation at Tm 2306. This inflow is found in heterogeneous gneisses of the southern Gotthard massif at a shallow depth. The sugar-grained dolomites found in the southern sediment cover of the Garegna supply gallery show high inflows ranging between 120 and 150 l/s over a total section length of about 1,000 m. Close to the northern portal of the KW Vorderrhein Val Val—Curnera reservoir supply gallery, a maximum (initial?) inflow rate of 1,300 l/s occurred within a 200-m wide cataclastic fault zone in the gneisses of the Tavetsch massif close to the northern border to the Aar massif (possibly the same regional tectonic structure responsible for the large inflows to the Furkareuss supply gallery). In the KW Vorderrhein Sedrun—Medels gallery, 1,000 l/s rushed in from a 200-m-long tectonized section in the transition area from Triassic sediments to Permo-Carboniferous gneisses of the Urseren-Garvera zone (Tm 5.050–5.250). Due to the shallow depth, the evaporitic sediments (anhydrite/gypsum) occurring within this succession are presumably affected by karstic dissolution phenomena. Finally, in the Gas Transit pipeline Obergesteln gallery, strong initial inflows were recorded in the northern 1,000 m, with the highest individual inflow of 110 l/s (Tm 550) encountered at 300 m depth (Klemenz 1974). Again, this entire section shows relatively deep (>300 m) toppling of Variscan gneisses (GHG), and the initial inflow rates quickly decreased towards much lower values (10–50 l/s over the entire section after 1 year).

2.4. Statistical distributions of tunnel inflow rates

2.4.1. Inflow rate distribution as a function of geological unit

In the statistical analysis of the distribution of inflow rate, only tunnel inflow rate data with a sufficient quality have been taken into account. Data from the following tunnels or galleries have been excluded: KW Amsteg supply gallery, Goeschenen pressure gallery, KW Lucendro pressure gallery, KW Ritom Garegna supply gallery, KW Vorderrhein Sedrun-Medels gallery, KW Wassen supply gallery and Gas Transit Gstellli gallery.

As discussed earlier, rate data have been divided into three different sets, based on continuous inflows, dripping zones, and "dry" tunnel sections. The rates of continuous inflows, summed over 100-m-long tunnel intervals, include all mapped continuous inflows shown in Figure 3, but exclude extreme values and continuous inflows smaller than 0.01 l/s. Inflows with a rate lower or equal to 0.01 l/s have not been systematically reported and for that reason have been excluded.

The second set is derived by assigning a value to each dripping zone according to its strength and by summing these values again over 100 m-long tunnel intervals. The values assigned are 0.001 and 0.01 l/s for low and heavy dripping zones respectively. Assigning rate values to dripping zones is problematic for the given data set. An attempt to relate the dripping zones to inflow rates in Bedretto gallery can be found in Lützenkirchen (2002), but as the definition of dripping zones varies between individual tunnel geologists, the generalization of his assessment remains questionable. Lützenkirchen estimated flow rates for dripping zones lower than the values assigned in this study. Modifying the assigned rate values results in a shifting and/or rescaling of the dripping-rate distribution. However, it does not significantly modify the total cumulative inflow rate from dripping and continuous inflows.

The last set of inflow rates used in this study is the mean inflow rate from "dry" tunnel sections (i.e. without dripping inflows), which is non-visible water inflow transported as water vapor through the tunnel ventilation. For the assessment of these rates, new air water vapor measurements from a 1,000-m-deep section of the Gotthard Base Tunnel near Sedrun (Figure 2) could be used. In this section, located north and south of the Sedrun shaft, individual vapor flow measurements from the west tube (W) and the east tube (E) were used. Both tube sections in the north (tubes NW, NE) are around 1,300 m long and located in the Tavetsch massif. The other two sections located south of Sedrun's shaft (tubes

SW, SE) are around 2,300 and 2,500 m long respectively and belong to different geological units (see Figure 2). While long sections of the north tubes are indeed "dry", the tubes in the south direction contain several dripping sections and a few continuous inflows. Details of the procedure used to compute the water vapor output are described later (see Appendix 2). The water vapor flow rate of each of the four tubes (NW, NE, SW, and SE) has been divided by its length to obtain the flow rate per tunnel meter or hectometer. As shown in Table 9, the hectometric inflow rates are comparable to the smallest inflow rates reported for a single continuous inflow (0.01 l/s). The equivalent transmissivity and hydraulic conductivity values have also been computed by assuming a tunnel radius of 5 m and a differential head of 1,000 m. The different water vapor output parameters and resulting rate values are summarized in Table 9. These water-vapor rate values are mean values because the water-vapor flow has been integrated over more than 1,000 m of tunnel. Most probably this flow is not constant along the tunnel and a function of the local rock-mass hydraulic conductivity. Since the walls of NW and NE tubes are rather dry, the transmissivity (T) and hydraulic conductivity (K) values derived from these sections can be considered as mean T- and K-values for the matrix, here defined as the rock embedding these tunnel "dry" sections without dripping zones and continuous inflows.

The histogram of Figure 4 shows the distribution of the continuous inflow rates (black bars) and the dripping inflow rates (grey bars) for all the geological units combined. The binning is logarithmic and the bin size is chosen to be equal to the size of the rate classes (one log cycle in this case) in order to avoid a discontinuous or incomplete representation of the rate distribution. Both rate distributions look log-normal and overlap each other. Due to sampling limits, the surveyed rate distribution is truncated toward the low rate values. Although the dripping-inflow-rate distribution is more uncertain than the continuous-inflow-rate distribution, combining them has the advantage to extend the sampled rate distribution towards the low rate values. The surveyed rate distribution per 100 m tunnel section for all geological units extends over seven orders of magnitudes from 10^{-4} to 10^4 l/s. Figure 5 shows the undifferentiated-inflow-rate distribution when dripping and continuous flow rates are summed over each individual 100-m interval. The resulting distribution is again close to a log-normal distribution.

Similar histograms have been created for each geological unit and are shown in Figure 6. The histograms rarely follow a log-normal distribution and are sometimes scattered and asymmetric: the right (higher rate) tail of the distribution

is often longer than the left tail. There is no evident correlation between distributions of similar lithologies. For example, the highest maximum rate is found for the Gotthard massif granites (GHG), whereas the lowest maximum rate is observed for the Aar massif granites (AAG).

2.4.2. Inflow rate distribution as a function of depth

For the analysis of the dependence of inflow rate as a function of depth, the same tunnels in the previous section (see section Inflow rate distribution as a function of geological unit) have been excluded from the data set. Only the first set of data (continuous inflows) have been used, and 100-m intervals with inflow rates lower or equal to 0.01 l/s have been assigned the rate value 0.01 l/s to account for the dripping and the moisture evaporation. This simplification can lead to overestimation of inflow rates and a bias in the rate distribution.

For all geological units combined, and for each geological unit, five different plots (Figures 7 and 8) have been generated to study the interdependency between inflows and depth. As data are discrete and non-homogeneously distributed with depth, a sampling window (moving average) of 200 m depth has been used in all the plots for five different rate classes (0.01, 0.01–0.1, 0.1–1, 1–10 and >10 l/s). The first type of plot shows the total number of 100-m intervals (NI) of the different rate classes versus depth in order to visualize the variability of sampling frequency with depth. The more data are available, the more the results in the next four plots are significant. The second plot type shows the total number of 100-m intervals of the different rate classes divided by the total number of all 100-m intervals as a function of depth; the result is the proportion of the different classes (PC) among the sampled intervals. The third plot type shows the total inflow rate (TIR) of the different rate classes versus depth. For the fourth plot type, the total inflow rate of the different classes is divided by the total inflow rate and plotted versus depth; this gives the contribution to the total flow (CC) of each class versus depth. Finally, the last plot type represents the total inflow rate of the different rate classes divided by the number of 100-m intervals of each class versus depth; the result is the total mean inflow rate (MIR) per 100-m interval of the different classes versus depth.

From the analysis of the plots for all geological units combined (Figure 7), one can conclude that:

- PC: The relative proportion of the different inflow classes is nearly constant with depth
- NI: Apart from the artificial 0.01 l/s class, which includes 50–70% of the intervals, the most frequent is the 1–10 l/s class and the highest rate class (>10 l/s) is the less represented
- CC: More than 90% of the total flow rate is fed by intervals whose rate is bigger or equal to 1 l/s
- MIR: The mean inflow rate per 100 m interval amounts to about 2 l/s and is relatively uniform over long depth sections
- MIR: A section of extraordinary high mean-inflow rates appears between 1,050 and 1,250 m depth

Concerning the plots of the individual geological units (Figure 8), one can conclude that:

- NI: The depth intervals with a significant amount of observations strongly varies with geological unit
- PC and MIR: The upper most 200–400 m of the AAG, ANG and GHG geological units show a low relative proportion of the highest rate classes and low mean inflow rates
- PC and MIR: In contrast, the upper most 200–400 m of the AIK, GAK and GSG geological units show a high relative proportion of the highest rate classes and high mean inflow rates
- PC and MIR: Below the uppermost interval, a general decrease of the highest rate classes proportion and of the mean rates is observed in the ASG, GAK and GSG geological units
- MIR: The AAG unit shows a steady increase of the mean inflow rate down to 800 m depth
- MIR: No clear depth trend is observed in the mean rate of GHG and ANG units

2.4.3. Inflow spacing distribution along tunnels

The spacing distribution of continuous inflows has been analyzed along four tunnels and galleries where precise inflow localization was available (Masset and Loew 2007). This analysis shows that the spacing distribution of continuous inflows along the Realp leg of Furka base tunnel, the Gotthard SBB railway tunnel,

the Gotthard A2 security gallery and the Goeschenen pressure drift are well fitted by power laws over ~ 1.5 – 2 orders of magnitude (Figure 9). This illustrates the clustered distribution of continuous inflows along tunnels. In other terms, these appear in series separated by intervals where only dripping occurs and this pattern repeats at different scales.

Figures 10 and 11 show the spacing distribution of continuous inflows, heavy dripping inflows and light dripping inflows along Gotthard SBB railway tunnel and Goeschenen pressure drift. On both plots, it can be seen that, in contrast to continuous inflows, dripping zones are more evenly spaced and particularly light dripping inflows are well fitted by exponential functions. Thus, it appears that the spacing distribution of inflows along tunnels is a function of the inflow rate or type.

2.5. Major parameters controlling tunnel inflows

2.5.1. Tectonic overprint

In the central Aar and Gotthard massifs, the tectonic overprint has induced important multi-scale ductile and brittle deformations. Brittle tectonic overprint includes all types of fractures formed during and after the Alpine orogeny.

In Figures 7 and 8, the peaks in mean inflow rate always results from the presence of one or a few high-rate inflows at the intersection between the tunnel and zones of brittle deformation. For example, the deviation from the mean inflow rate shown in Figure 7 in the depth interval of 1,050 to 1,250 m is related to the local occurrence of strong inflows from brittle faults in the ANG (KW Oberhasli Gadmenwasser supply gallery) and GHG geological units (Gotthard A2 security gallery). These deviations are superimposed on possible depth or lithology dependant trends in inflow rate. The strong brittle overprint of GHG (granites of the Gotthard massif) controls the inflow rate distribution and completely obscures the correlation between inflow rate and depth.

In contrast, the AAG geological unit (granites of the Aar massif) shows no significant peaks of the inflow rate and the lower brittle overprint of AAG compared to GHG allows the observation of a depth-dependant inflow rate. A general lower brittle tectonic overprint not only characterizes the AAG geological unit, but also the entire central Aar massif, with the exception of its southern margin (ASG). Consequently, mean 100-m interval inflow rate values are lower for the Aar massif (2.6 l/s) than for the Gotthard massif (3.85 l/s).

2.5.2. Topography and unstable slopes

The systematic trend of increasing inflow frequencies and rates in the upper 100 to 400 m of Figures 7 and 8 reflects partly unsaturated conditions in mountain slopes. In the study area, the upper 100–400 m below ground surface often show highly permeable rock masses composed of a dense partially interconnected pattern of open fractures (southern portal of SBB Gotthard, northern portal of gas transit Obergesteln, southern portal of Bedretto gallery). These open-fracture sets are composed of tectonic and near-surface unloading fractures (Bucher 2006; Zangerl et al. 2006). Fractures are opened by stress release and slope deformation phenomena, especially flexural and block toppling (Keller and Schneider 1982; Klemenz 1974). This induces a significant increase in fracture transmissivity. Depending on the local topographic and geologic situation, the upper most 100–400 m of rock can show saturated or unsaturated conditions before tunnel excavation, i.e. the absence of tunnel inflows in these sections do not imply low permeability rock masses. In fact, the initial tunnel inflow rates from such sections are often relatively high and decrease during the first days and weeks dramatically due to lowering of the water table down to the elevation of the tunnel (Klemenz 1974; Loew et al. 2007). Late time inflows are small and strongly controlled by local and temporally varying groundwater recharge. As discussed earlier, most of the high initial inflows have not been included in the data base shown in Figure 3.

2.5.3. Depth and lithology

The dependency between inflow rate and depth is most visible in the particular case of the AAG unit (granites of the Aar massif) because the tunnel sections crossing this unit did not encounter strong inflows that can be related to surface unloading or brittle faults (Figure 8). This unit shows increasing inflow rates with depth (MIR in Figure 8). However, this does not mean that granites are in general less affected by brittle tectonic or less permeable than gneisses since the GHG unit (granites of the Gotthard massif) shows strong inflow rate variations with depth due to brittle faulting.

Moreover, when comparing the Gotthard railway (SBB) tunnel (Figure 3c) with Gotthard A2 security gallery (Figure 3d), which run nearly parallel to each other at a lateral distance of up to 3 km, one can see that the high inflow rates found in the granitic section (GHG) of the A2 security tunnel have no equivalent in the gneissic section (GAK) of Gotthard railway tunnel. As inflows in both

tunnels are controlled by brittle faults cross-cutting the tunnels at a high angle, it is suggested that brittle faulting in granites leads to more conductive structures than brittle faulting in gneisses.

2.6. Fracture transmissivities

2.6.1. Data processing and transmissivity models

To compute transmissivity values from tunnel inflows, only data with sufficient quality have been used. Data from the following tunnels and galleries are not included in the transmissivity analysis: KW Amsteg supply gallery, Goeschenen pressure gallery, KW Lucendro pressure gallery, KW Ritom Garegna supply gallery, KW Vorderrhein Sedrun-Medels gallery, KW Wassen supply gallery and Gas Transit Gstellli gallery. Continuous inflow intervals with rates smaller or equal to 0.01 l/s have been excluded because small rates have not systematically been reported. As described earlier (see section Data set description), dripping zones have been assigned rates of 0.01 l/s or 0.001 l/s depending on their strength. Transmissivity values have been computed for each 100-m interval using three different analytical models depending on the hydrogeological setting of the considered 100-m interval (Loew 2002). All models are 2D and assume that:

- The inflow is derived from an infinite planar layer oriented normal to the tunnel/gallery axes (vertical layer, fracture zone, fault or fault zone)
- The layer transmissivity is homogeneous and no leakage takes place between the layer and the surrounding rock
- The tunnel is radial and at a constant head controlled by atmospheric pressure
- The flow is governed by Darcy's law
- The inflow time of the rate reported in the data base corresponds to the delay time
- The rock mass specific storage is equal to 10^{-6} m^{-1} (only required for transient models)

The first model represents infinite acting radial flow (Figure 12a) and can be approximated with the Jacob and Lohman (1952) solution for non-steady flow to a well of constant drawdown, assuming that the hydraulic head drawdown is equal to the elevation difference between the tunnel and the water table (often

approximated by ground surface). The radial flow model is the basic model applied to most of the productive 100-m tunnel intervals.

The second model is similar to the first one except that it is limited by a linear constant head upper boundary (Figure 12b) under steady-state conditions. This model is applied instead of the first model when a recharging lake, a river or a Quaternary aquifer at the surface is suspected to maintain the water table at a constant level. For example, this model is used to compute transmissivity of a section of the Gotthard railway and A2 highway tunnels below the gravel aquifer of the Urseren valley. This model it is also used to compute the transmissivity from dripping rate values.

The third model derived from Doe (1991) is a solution for linear flow under a constant drawdown. It applies when the drying out of surface springs in direct response to the tunnel or gallery excavation demonstrates the drawdown of the water table down to the tunnel elevation and when linear horizontal flow normal to the tunnel axes is a reasonable approximation (Figure 12c) (Klemenz 1974, Loew et al. 2007). The specific yield (S_y) is set to 0.01. This value has been derived by dividing the total amount of water drained into a section of the Obergesteln gallery by the volume of rock drained. The volume of water was measured and the volume of rock estimated from the position of dried out and unmodified surface springs (Loew and Masset 2008, unpublished report, see Table 1). This value has also been derived by other authors in similar surrounding (e.g. Maréchal et al. 2004, 2006). As an example, the third model is used to compute transmissivity for the northern shallow section of the Gas Transit Obergesteln Drift affected by toppling, resulting in open vertical fractures oriented perpendicularly to the tunnel axes.

2.6.2. Results

Transmissivity distribution

The transmissivity distribution for all geological units combined is plotted on the semi-logarithmic histogram in Figure 13. The binning size is equal to one logarithmic cycle. Transmissivity values computed from both continuous flow rates (black bar) and dripping flow rates (grey bar) are represented. Transmissivity values range over 9 orders of magnitude from 10^{-10} to 10^{-1} m²/s. Figure 14 shows the distribution of transmissivity when continuous and dripping inflows are summed for every 100-m interval. The resulting transmissivity distribution could be bimodal or log-normal. The true transmissivity distribution of continuous

inflows is probably close to log-normal as suggested by Figure 15. In this figure, the transmissivity distribution derived from high-quality continuous inflow measurements of the Gotthard A2 security gallery (black line) is plotted on a double logarithmic graph of transmissivity versus cumulative number. The grey line represents a log-normal synthetic sample with the same mean, variance and data number. Figure 16 shows histograms of the transmissivity distribution of each geological unit. The binning is again logarithmic and each bin corresponds to one log cycle. Transmissivity values derived from both dripping inflows (grey bars) and continuous inflows (black bars) are represented.

Transmissivity distribution versus overburden

The 100-m interval transmissivity distribution of each geological unit and of all geological units combined is plotted versus depth in Figure 17. The data, represented by crosses (model 1), circles (model 2) and triangles (model 3), are plotted with arithmetic (black) and geometric (dashed grey) moving averages of 200-m-sized windows. Only transmissivities computed from continuous inflow rates are shown in this figure. Transmissivity values close to the ground surface are more scattered than at depth. This results from the difficulty to interpret and convert shallow tunnel inflow rates into transmissivity values. At depths greater than 400 m, the rock-mass is always saturated and inflows are less difficult to interpret, even after long term drainage conditions. The 100-m interval transmissivity values below 400-m depth typically range from 10^{-9} to 10^{-4} m²/s with an arithmetic and geometric mean around 10^{-6} m²/s and show no global trend with depth. The deeper transmissivity values from the ASG and GSG geological units (mainly gneisses and schists) have a weak tendency to decrease with increasing depth. The deeper AAG, GAK, GHG geological units (mainly granitic rocks) have transmissivity values which show no decreasing trend with increasing depth.

Transmissivity distribution along selected tunnels

Finally, Figure 18 shows plots of the transmissivity distribution along selected tunnels. These tunnels have been chosen for the higher quality of their inflow data. Bars represent the total transmissivity value per 100-m interval accounting for the continuous inflows, the dripping inflows and the water vapor flow. The water vapor flow has been taken into account by assigning each 100-m interval a transmissivity value of 10^{-8} m²/s. Again, the greatest uncertainty in the computed transmissivities is related to the tunnel sections with shallow depth. For

example, the Gotthard SBB railway tunnel in Figure 18 indicates a highly transmissive section close to the southern portal of the Gotthard SBB tunnel. In other sections with similar geological and hydrogeological conditions (Gas Transit Obergesteln gallery; Furka base tunnel Bedretto gallery), such high inflows have not been included in the main data base because they only represent early time inflows.

2.7. Rock mass effective hydraulic conductivity

2.7.1. Data processing and conductivity models

Different models have been used to estimate rock mass effective hydraulic conductivity from the individual inflow transmissivities (Löv et al. 1996). The equations of the three different effective hydraulic conductivity models are summarized in Figure 19. These models are all derived from a general effective hydraulic conductivity model for fractured rocks as described for example in Voborny et al. (1994):

$$2-2 \quad K_{eff,i} = G_i \bar{T} F$$

with:

- $K_{eff,i}$: diagonal ii-components of the effective K-Tensor
- G_i : geometric factor describing conductive fracture orientation and extension
- \bar{T} : mean T-value of conductive fractures (arithmetic or geometric, see text)
- F : frequency of conductive fracture

If a single family of equidistant parallel features of infinite extent has a log-normal distribution of its transmissivity values, then the effective hydraulic conductivity in the direction of the features is proportional to the arithmetic mean of the distribution (Voborny et al. 1993, unpublished report, see Table 1). This relation is used to compute the effective vertical hydraulic conductivity. In contrast, if the extent of the features is limited, the orientation of the features is isotropic, their spatial distribution is homogeneous and their transmissivities are log-normally distributed, then the effective hydraulic conductivity is proportional to the geometric mean of the distribution (Gelhar 1987).

All three models used are strong simplifications and assume that matrix conductivity is negligible (no leakage) and conductive fractures have homogeneous transmissivity (no channeling). The first two models refer to the bulk rock mass hydraulic conductivity from sets of fractures feeding continuous inflows. The third model represents hydraulic conductivity from sets of fractures feeding dripping inflows. The main difference between models 2 and 3 and model 1 is the assumed distribution of fracture orientations (isotropic versus vertical): models 2 and 3 can be viewed as representing intermediate and small-scale fractures (joints) which show a nearly isotropic distribution of spatial orientation, and model 1 as representing the larger-scale faults, striking at a large angle to the tunnel axes and dipping steeply towards the south or north. Whereas models 2 and 3 give isotropic hydraulic conductivity, model 1 only considers vertical hydraulic conductivity. Because all available data refer to 100-m interval transmissivity and not individual fracture transmissivity, frequencies and transmissivity means are referred to 100-m tunnel intervals with continuous inflows (models 1 and 2) or dripping inflows (model 3).

2.7.2. Results

Figure 20 shows plots of the distribution of the effective hydraulic conductivity as a function of depth for the three effective hydraulic conductivity models. From the analysis of the plots for all geological units combined one can conclude that:

- The uppermost 200–400 m below ground surface show strongly increased hydraulic conductivities.
- Below this section, the fracture-related isotropic effective hydraulic conductivity, as well as the matrix isotropic effective hydraulic conductivity, remains constant with increasing depth.
- Below 200–400 m, the fault zone-related vertical effective hydraulic conductivity weekly decreases with increasing depth.

Concerning the individual geologic unit plots:

- Below the near surface unloading section, a decrease of the effective hydraulic conductivity is observed in gneissic and schistose rocks of ASG, GSG and GAK.

- Both granitic units (AAG and GHG) show no clear trend of the effective hydraulic conductivity with increasing depth. The large scatter in the GHG profile results from localized occurrence of highly conductive brittle faults. Such faults have not been encountered in tunnel sections crossing the AAG unit.

2.8. Discussion

In this section, the inflow spatial variability, some of the critical model assumptions for transmissivity and hydraulic conductivity estimations, and the resulting transmissivity and effective hydraulic conductivity distributions are interpreted and discussed. Finally the results are compared with those from other studies.

2.8.1. Tunnel inflow distribution and variability

The main parameter governing tunnel inflow rate is the degree of brittle tectonic overprint; the inflow rate variability due to the presence or absence of brittle tectonic features is higher than the variability due to changes in lithology or depth (see section Depth and lithology). The mean inflow rate is highly dependent on the extreme rate values which are mostly linked to important fault or fracture zones (see section Exceptionally high tunnel inflow rates). Unfortunately information concerning the type of fracture related to each inflow is not available for most of the tunnels and galleries considered. The spacing distribution of inflows (see section Inflow spacing distribution along tunnels) shows that continuous inflows, in contrast to dripping zones, are not evenly spaced and therefore difficult to predict. This unpredictability increases with the rate because high rate inflows (>10 l/s) are rare. Even if strong inflows can be related to important fault zones, locating these features does not ensure a good inflow prediction due to variations of fault architecture and channeling (only a small portion of faults are highly conductive and directly intersected by a tunnel).

Regional investigations show, that the Gotthard massif suffered much stronger brittle tectonic deformations than the Aar massif and that brittle faults of substantial width occur frequently in the Gotthard massif but not in the Aar massif (Laws 2001; Lützenkirchen 2002; Zangerl et al. 2006). With the exception of an extreme inflow from a brittle fault in the Goeschenen Voralpreuss supply gallery, granites in the Aar massif (AAG) show low inflow rates and sparse inflows with only minor influences of brittle faulting visible by the small scatter of the

depth dependant inflows (Figure 8). This is the only case where a systematic increase of tunnel inflow with depth can be observed in the first 1,000 m. The derived interval transmissivities and hydraulic conductivities are constant (Figures 17 and 20) and indicate that in these granites inflow rates are mainly controlled by the tunnel-induced hydraulic head gradients increasing with depth.

2.8.2. Uncertainties in transmissivity and hydraulic conductivity estimations

The most critical assumptions of the models used to estimate fracture transmissivity (transmissivity of 100-m intervals with flowing fractures) are:

- The fracture extension is big enough to be considered as infinite or well interconnected and no leakage takes place between the fracture and the embedding matrix. However, in the long term, fluid exchange between fracture and matrix might be considerable. As most of the inflows considered here are relatively late (a few weeks), the error related to this assumption might be significant. As flow at late times should be controlled by matrix leakage, the real transmissivity values might be slightly underestimated.
- Flow in fractures is governed by Darcy's law. Because of the extremely high head gradients around open deep tunnels, non-linear turbulent flow is suspected to impact strong inflows. This process will lead to an underestimation of the true fracture transmissivity.
- Fracture apertures do not change in response to tunnel drainage. Rutqvist and Stephansson (2003) state that, if stress and stiffness are high, additional closure resulting from the fluid pressure release will be insignificant at a large scale. However, significant differences between inflows to pre-drillings and (upscaled) inflows to tunnels at the same locations have been observed in many projects, suggesting an influence of the pore pressure and effective stress on fracture apertures around tunnels. For a depth of 500 m in granite, Ivars (2006) has carried out a detailed modeling study on the influence of hydro-mechanical coupling in fractured rock masses. He concludes that even a small change in aperture at the large depth considered has a significant effect on flow. The effect is dependant on the fractures' orientation, normal- and shear-stiffness, and friction and dilation angles. Normal stiffness values on joints in granitic

rocks have recently been compiled from laboratory tests, reported by Zangerl et al. (2008c), who applied them in a large-scale rock mass consolidation study (Zangerl et al. 2008a, b). Closure and shear of joints and faults around Alpine tunnels in response to drainage and pore pressure drawdown is shown to be significant and the cause of surface settlements amounting to about 4 cm (Zangerl et al. 2008b). For these reasons, it has to be assumed that the estimated fracture transmissivities have the tendency to underestimate the values under natural pore pressure conditions.

In summary, all assumptions made for the transmissivity derivation could have lead to a slight underestimation of the true fracture transmissivity. To compare the uncertainty of the reported transmissivity values resulting from the three different flow models, a probability density function has been assumed for each parameter included in the three different models (Figure 12). Rate, specific storage and yield are assumed to be log-normally distributed, whereas radius, time, depth and drawdown, are assumed to be distributed normally. The probability density function of transmissivity, derived by Monte Carlo analysis, has then been computed for each selected 100-m interval based on the assumed parameter distributions and on standard deviations. Two parameter scenarios have been investigated: a "best guess" that assumes relatively small parameter standard deviations and a "worst case" with upper bound parameter standard deviations (Table 10). Specific storage is poorly known, assumed to be constant and equal to 10^{-6} 1/m (Löw et al. 1996). For this reason, this parameter has been given the highest standard deviation (10^{-5} 1/m).

The resulting transmissivity histograms for three selected 100-m tunnel intervals (one per transmissivity model) and for each scenario are plotted in Figure 21. For the best guess parameter distributions, the Jacob and Lohman and the constant head boundary models result in transmissivity values which are log-normally distributed and remain within one log cycle. This uncertainty of the estimated values is acceptable especially when compared to the uncertainties resulting from other types of large scale transmissivity estimation. In contrast, the distribution resulting from the linear flow model spreads over five orders of magnitude. This high variability is related to the head gradient which is raised to the power of four in the linear flow transmissivity equation. For the worst case, the uncertainty in transmissivity for all transmissivity models is only slightly

increased. Consequently one can be confident in the transmissivity values derived from the two radial flow models, and relatively cautious with the transmissivity values derived with the linear flow transmissivity model. This is confirmed by the large transmissivity variations resulting from the linear flow model as shown in Figure 17 (triangles). The uncertainties in the hydraulic conductivity models result from some of their strong and unverified assumptions such as infinite extent of homogeneous parallel planes for the vertical fracture model or the homogeneous distribution and interconnectivity of conductive fractures for both isotropic models.

2.8.3. Transmissivity and effective hydraulic conductivity distribution

As shown in Figure 13, the shape of both dripping and continuous inflow transmissivity distributions is close to the shape of a log-normal distribution, whereas in Figure 14, when both types of transmissivity values are summed over each 100-m interval, the resulting distribution looks bimodal and skewed. This bimodal aspect could result from an incomplete sampling of continuous inflow rates lower than 0.01 l/s or from an underestimation of the dripping rates. If it reflects reality, then it implies that continuous inflows and dripping zones are issued from different fracture systems. This explanation would support the conceptual model hypothesis that dripping inflows are related to a small fracture network belonging to the matrix, whereas continuous inflows are often related to a bigger network of faults.

The effective hydraulic conductivity distribution of all geological units combined (Figure 20), is about 10^{-8} m/s for the isotropically oriented fracture model, ranges from 10^{-8} to 10^{-5} m/s for the vertical fault zone model and is about 10^{-10} m/s for the matrix model. Again, the unloading zone in the uppermost 200–400 m is clearly visible, both in the combined plot and in the individual foliated rock units (toppling can not occur in granites because they lack a steeply dipping foliation set).

Concerning the individual geologic unit plots, a decrease of the effective hydraulic conductivity with depths below the unloading zone is weakly expressed in gneisses and schists of ASG and GSG. For all other geologic units, effective hydraulic conductivity remains more or less constant with increasing depth. The presence of a decrease in the hydraulic conductivity for some gneisses and schists with increasing depth can be explained by the lower stiffness of fractures and

faults in gneisses and schists compared to granitic rocks. As shown by Laws et al. (2003) fractured zones in gneisses (damage zones with cm-spaced fractures with 1-mm infill and micro fractures) of the Aar Massif have tangent Young's moduli (at 5 MPa confining pressure) ranging between 0.05–1.3 GPa, whereas the same zones in granites show values ranging between 1.5 and 14 GPa. At the same confining pressure of 5 MPa, the ratio of stiffness of the fault core (cohesionless micro breccias) in granite and the stiffness of the fault core in gneiss is about 3. This implies that, at least at shallow depth, gneisses and schists have a stronger response to changes in effective stress (Laws et al. 2003). For brittle faults with thick infillings of cataclastic materials, the relationships between stress and permeability as derived for porous media might be applicable—as in, for example, the Kozeny-Carman equation. For smooth parallel plate joints, the cubic law relates aperture change to permeability. Both relationships imply a strong non-linearity between porosity change and permeability. Therefore, stiffer fault rocks at greater depth (see Laws et al. 2003) might still show depth-dependant transmissivity.

2.8.4. Comparison with other studies

Systematic analyses of tunnel inflows have also been carried out in other regions (e.g. Cesano et al. 2000; Gargini et al. 2008). Cesano et al. (2000) showed that the thickness and composition of the weathered material and unconsolidated deposits above the intact bedrock surface were important factors in regulating groundwater inflows to the Bolmen tunnel (Sweden). The Bolmen tunnel's depth varies between 30 and 90 m, whereas in the present study, in Switzerland most of the inflows considered come from bigger depths. For shallow flow systems, the effects of surface deposits on groundwater recharge and tunnel inflow are much more pronounced. As shown by spring observations and numerical modeling (e.g. Loew et al. 2007; Ofterdinger 2001) the interactions between the water table and the draining tunnel are of minor importance for deep Alpine tunnels.

Gargini et al. (2008) integrated a large amount of spring and tunnel inflow data in the Northern Apennines and identified three distinct and hierarchically nested groundwater-flow systems. The shallowest (150–200 m deep) and most permeable was hosted by the decompacted portion of the rock mass. A second flow system reaching 300–400 m depth, and a third flow system of up to 2,000 m depth were related to tectonic faults. In comparison to observations for this Swiss study, the first flow system type can be confirmed. Because of the stronger relief,

the depth of the mass movement and unloading phenomena is deeper in the Swiss study area (Klemenz 1974, Loew et al. 2007).

The published transmissivity and effective hydraulic conductivity values of crystalline rocks are mainly derived from borehole packer tests (Mazurek 1993; Stober 1997). When comparing transmissivity or permeability values obtained from tunnel inflow data with transmissivity or effective hydraulic conductivity values derived from packer tests, it is important to note that the volume tested by a deep tunnel is much bigger than that of a surface based borehole hydro-test. This is due to the large pressure drawdown induced by an open deep tunnel, the drawdown duration and the dimensions of the excavation. This might influence the comparison of hydraulic conductivity if this property is indeed scale-dependent as suggested for example by Brace (1980) and Clauser (1992).

The deepest inflow (1.2 l/s) included in the full data set was reported from the Bedretto gallery at a depth of 1,515 m. The existence of high inflows into underground excavations in crystalline rocks of that depth is not surprising. In the French part of Mont Blanc tunnel (linking France to Italy), for example, a cumulate inflow rate of 140 l/s was measured along a 750-m section whose depth is greater than or equal to 2,000 m (Gudéfin 1967). Moreover, the existence of deep water circulation in crystalline rocks has been demonstrated in several deep boreholes. For example, in a hot dry rock (HDR) well in Urach, Germany, water circulation in an open fracture system has been detected by hydraulic tests at depths of 3 –4 km (Stober and Bucher 1999).

An extensive review and a discussion of deep borehole hydraulic test results from crystalline rocks can be found in Stober and Bucher (2007). The range of hydraulic conductivity values derived for granites in the present study ($K=10^{-11}$ – 10^{-7} m/s) is on the lower side of the range of hydraulic conductivity values reported for similar rocks ($K=10^{-11}$ – 10^{-4} m/s) and the range of hydraulic conductivity values for gneisses in this study ($K=10^{-11}$ – 10^{-4} m/s) is quite similar to the range of hydraulic conductivity values derived from deep boreholes of northern Switzerland ($K=10^{-13}$ – 10^{-4} m/s). Despite the fact that hydraulic conductivity values derived by inflow analysis are representative for larger volumes of rock than packer tests, the hydraulic conductivity values derived from both methods are comparable.

According to Stober and Bucher (1999), granites of the Black Forest (Germany) are on average more permeable than gneisses. This difference is attributed to differences in texture and mineral composition which in turn causes

granites to deform in a more brittle fashion than gneisses. Stober (1995; 1997) also reports that, in the Black Forest, a general permeability decrease with depth characterizes the gneisses but not the granites. Both trends can also be identified in the data set reported in this paper.

2.9. Summary and conclusions

In the central Aar and Gotthard massifs (Switzerland), groundwater inflows to 136 km of tunnels and galleries have been analyzed in order to characterize the hydraulic properties of different geological units and investigate their dependency on different parameters like depth, lithology and tectonic faulting. Inflow rates per 100 m of tunnel are converted into transmissivity values by means of basic transmissivity models like the Jacob and Lohman approximation for radial flow to a well with constant drawdown. Transmissivity values are then converted into hydraulic conductivity values with analytical equivalent porous medium (EPM) models.

The distribution of inflow frequency and rate can be described by two main depth intervals. The first interval ranges from the surface down to 200–400 m of depth. In most of the geological units (ANG, AAG, GHG, GMB), this interval is characterized by a low inflow frequency and rate, both of which increase with depth. Exceptions are AIK, GAK and GSG geological units which exhibit relatively high frequencies and rates from the surface. The authors interpret this interval to be a variably saturated zone of enhanced permeability resulting from stress release and slope deformation phenomena. Stress release and slope deformations (often related to deep toppling) can open joints and induce very high, large effective hydraulic conductivities. Given the Alpine topography, the inflows in these near surface sections can be low because of deep water tables (tunnel sections can be above the water table initially or after short term drainage). Therefore, close to the surface (up to 200–400 m) the spatial distribution of groundwater flow depends on:

- Topography: steep slopes in hard rocks are more susceptible to unloading phenomena and gravitational movements than moderate hill slopes
- Valley orientation with respect to the foliation: toppling occurs when the steeply dipping foliation runs parallel to the valley axes

- Rock fabric: rocks presenting no foliation (granites or massive gneisses) are not affected by toppling but can develop exfoliation fractures parallel to the topography that decrease in frequency and persistence with depth

Below 200–400 m depth, increasing (AAG) and decreasing (ASG, GAK, GSG) trends of inflow rates are observed, as long as they are not superimposed by a few strong inflows from brittle fault zones. These differences in trends are related to the variations in stiffness of fractured gneisses and granites—as shown by lab experiments on cores from the Aar massif at 5 MPa confining pressure, the stiffness of fractured zones (damage zones) in gneisses is about one order of magnitude smaller than in granites. The authors suggest that the stiffness of fractured granites is so low, that in the upper 400– 1,500 m, increasing effective stresses with depth has no measurable effect on fracture apertures and permeability. On the other hand, the induced hydraulic head gradients around tunnels that increase with depths lead to slightly increasing inflow rates in this depth interval. The low stiffness of fractured rocks in gneisses and schists significantly reduces fractures apertures and transmissivity in the observed depth range of up to 1,500 m.

Below 200–400-m-depth brittle faulting is the dominant parameter controlling inflow frequency and rate. The study shows that significant regional variations in brittle tectonic overprint exist. Mainly ductile Alpine deformation structures (fine grained metamorphic mylonites) are found in the Aar massif shear zones, whereas in the Gotthard massif, most ductile Alpine shear zones have been strongly reactivated under brittle conditions. The more intensive brittle tectonic overprint of the Gotthard massif clearly translates into a higher mean tunnel inflow rate compared to the Aar massif.

The spacing distribution of inflows along tunnels or galleries is a function of the inflow rate. Low rate inflows (dripping zones) follow a negative exponential distribution and are more evenly distributed and more abundant than higher-rate inflows (continuous inflows) which follow power law distributions and appear in clusters. Inflows with outstanding rates are rare and unpredictable. However, these rare and extreme inflows have a big impact on the total flow into an underground excavation. Whereas in the entire study area, the mean inflow rate per 100-m tunnel segment is about 2 l/s; more than 90% of the total flow rate is fed by intervals whose rate is bigger or equal to 1 l/s.

Transmissivity distribution has been derived from the fracture inflows to 100-m-long tunnel segments using three types of analytical flow models, frequently used in the analysis of tunnel inflows. These models rely on important assumptions regarding fracture persistence, leakage, laminar flow and hydro-mechanical coupling. It is shown that the analytical equations used have the tendency to underestimate the undisturbed fracture transmissivities.

Down to 200–400 m depth, transmissivity values per 100 m of tunnel (10^{-9} – 10^{-1} m²/s) are higher on average and are more scattered than at larger depths (10^{-9} – 10^{-4} m²/s). The higher transmissivity is a real characteristic of the shallower part of the rock mass, whereas the higher scatter of the data could be partially an artifact resulting from the difficulty to interpret and convert shallow tunnel inflow rates into transmissivity values. The transmissivity values tend to decrease in the gneissic or schistous geological units (ASG, GSG), whereas no trend is observed for the granitic units (AAG, GAK, GHG). The transmissivity distribution of continuous inflows is close to a log-normal distribution.

As equivalent porous medium (EPM) hydraulic conductivities are computed with mean transmissivities, they essentially show the same characteristics. A more permeable zone at shallow depths (up to 200–400 m) is characterized by values ranging between 10^{-10} and 10^{-4} m/s. A deeper zone of constant (AAG, GHG) or decreasing (ASG, GSG, GAK) hydraulic conductivity shows values ranging between 10^{-10} and 10^{-7} m/s. The decrease in EPM hydraulic conductivity is again related to effective stress dependant closure of fractures in gneissic rocks or schists. Strong deviations from these trends are related to brittle faults that appear as important preferential groundwater pathways, also at great depth.

2.10. Acknowledgements

The authors acknowledge the support from Nagra (A. Gautschi) and AlpTransit Gotthard AG (H. Ehrbar). Many original reports were provided by T. Schneider. W. Klemenz and B. Ehrminger made significant contributions to initial data compilations. U. Offerdinger, S. Laws, V. Lützenkirchen and C. Zangerl provided additional data and scientific input for detailed inflow analyses to the Bedretto and Gotthard A2 tunnels. Three anonymous reviewers made important comments to the first draft of this paper; the authors would like to thank them also.

2.11. Appendix 1: Notation

A [m ³ /s]	Air flow rate at airway entrance
C []	Channeling factor
c1 [kg/kg]	Air water content at the first measuring point 1
c2 [kg/kg]	Air water content at the first measuring point 2
F [m ⁻¹]	Frequency of the water conducting structures
G _i []	Geometrical factor
h [m]	Hydraulic head
K [m/s]	EPM hydraulic conductivity
K _{eff,i} [m/s]	Diagonal components of the effective hydraulic conductivity tensor
K _M [m/s]	Matrix hydraulic conductivity
L [m]	Tunnel length
m [kg/s]	Water vapor mass flow rate
P [Pa]	Absolute air pressure
P _w [Pa]	Water vapor partial pressure
Q [m ³ /s]	Flow rate
r [m]	Tunnel radius
R _f [J/(kg × K)]	Gas constant for wet air
R _L [J/(kg × K)] = 287:1	Gas constant for air
S []	Storativity
S [1/m]	Specific storage
S _y []	Specific yield
T [m ² /s]	Transmissivity
\bar{T} [m ² /s]	Mean transmissivity
t [s]	Time elapsed
Temp [K]	Dry bulb temperature
V [l/s]	Water vapor volumetric flow rate
V ₂ [l/s/m]	Water vapor volumetric flow rate per meter
V ₃ [l/s/hm]	Water vapor volumetric flow rate per hectometer
Δc [kg/kg]	Airway water vapor content
Δh [m]	Drawdown
ρ [kg/m ³]	Air density

2.12. Appendix 2: Water vapor flow rate derivation
according to the Ideal Gas Law

$$2-3 \quad R_f = R_L \frac{1}{1 - 0.378 \frac{P_w}{P}}$$

$$2-4 \quad \rho = \frac{P}{R_f \times \text{Temp}}$$

$$2-5 \quad m = A \times \rho$$

$$2-6 \quad \Delta c = c_2 - c_1$$

$$2-7 \quad V = m \times \Delta x$$

$$2-8 \quad V_2 = V / L$$

$$2-9 \quad V_3 = 100 V_2$$

2.13. References

- Abrecht J (1994) Geologic units of the Aar massif and their pre- Alpine rock associations: a critical review. *Schweiz Mineral Petrogr Mitt* 74:5–27
- Brace WF (1980) Permeability of crystalline and argillaceous rocks. *Int J Rock Mech Min Sci Geomech Abstr* 17:241–251
- Bucher S (2006) Talklüfte im östlichen Aarmassiv (Schöllenen-Schlucht) [Exfoliation joints in the eastern Aar massif]. Diploma Thesis, ETHZ, Switzerland
- Cacas MC, Ledoux E, Marsilly GD, Tillie B, Barbreau A, Durand E, Feuga B, Peaudecerf P (1990) Modeling fracture flow with a stochastic discrete fracture network: calibration and validation 1—the flow model. *Water Resour Res* 26:479–489
- Cesano D, Olofsson B, Bagtzoglou AC (2000) Parameters regulating groundwater inflows into hard rock tunnels: a statistical study of the Bolmen Tunnel in Southern Sweden. *Tunn Undergr Space Technol* 15:153–165
- Choukroune P, Gapais D (1983) Strain pattern in the Aar Granite (Central Alps): orthogneiss developed by bulk inhomogeneous flattening. *J Struct Geol* 5:411–418
- Clauser C (1992) Scale effects of permeability and thermal methods as constraints for regional-scale averages. In: Quintard M, Todorovic M (eds) *Heat and mass transfer in porous media*. Elsevier, Amsterdam
- Davy P, Bour O, De Dreuzy J-R, Darcel C (2006) Flow in multiscale fractal fracture networks. In: Cello G, Malamud BD (eds) *Fractal analysis for natural hazards*. Geological Society, London
- Doe TW (1991) Fractional dimension analysis of constant-pressure well tests. SPE paper 22702, Society of Petroleum Engineers, Richardson, TX
- Eckart P, Funk H, Labhart TP (1983) Postglaziale Krustenbewegung an der Rhein-Rhone-Linie [Post-glacial crustal movements along the Rhine-Rhone line]. *Vermess Photogr Kulturtech* 2:83
- El Tani M (1999) Water inflow into tunnels. In: Alten T, Backer L, Bollingmo P, Broch E, Holmoy K, Holter KG, Nielsen K (eds) *World Tunnel Congress 1999 on Challenges for the 21st Century*, Oslo, Norway, 29 May–3 June 1999
- Frei B, Breitenmoser T (2006) Geologisch-geotechnische und hydrogeologische Verhältnisse im Vortrieb Amsteg: Vergleich zwischen Prognose und Befund [Geological, geotechnical and hydrogeological settings of the Amsteg section: comparison of prediction and on-site findings]. In: Löw S (ed)

- Geologie und Geotechnik der Basistunnels am Gotthard und am Lötschberg.
Hochschulverlag, Zürich
- Frei B, Löw S (2001) Struktur und Hydraulik der Störzonen im südlichen Aar-Massiv bei Sedrun [Structure and hydraulic properties of shearzones of the southern Aar massif in the vicinity of Sedrun]. *Eclogae Geol Helv* 94:13–28
- Frey M, Bucher K, Frank E, Mullis J (1980) Alpine metamorphism along the geotraverse Basel-Chiasso: a review. *Eclogae Geol Helv* 73:527–546
- Gargini A, Vincenzi V, Piccinini L, Zuppi G, Canuti P (2008) Groundwater flow systems in turbidities of the Northern Apennines (Italy): natural discharge and high speed railway tunnel drainage. *Hydrogeol J* 16:1577–1599
- Gelhar LW (1987) Applications of Stochastic models to solute transport in fractured rocks. Technical Report SKB, SKB, Stockholm
- Goodman RE, Moye DG, Schalkwyk AV, Javandel I (1965) Ground water inflows during tunnel driving. *Bull Assoc Eng Geol* 2:39–56
- Gudefin H (1967) Observations sur les venues d'eau au cours du percement du tunnel sous le Mont-Blanc [Findings related to inflows during the excavation of Mont Blanc tunnel]. *Bull BRGM* 4:95–107
- Herwegh M, Pfiffner OA (1999) Die Gesteine der Piora-Zone (Gotthard-Basistunnel) [Rocks of the Piora zone (Gotthard Base Tunnel)]. In: Loew S, Wyss R (eds) *Vorerkundung und Prognose der Basistunnel am Gotthard und am Lötschberg*. Balkema, Rotterdam, The Netherlands
- Hwang J-H, Lu C-C (2007) A semi-analytical method for analyzing the tunnel water inflow. *Tunn Undergr Space Technol* 22:39–46
- Ivars DM (2006) Water inflow into excavations in fractured rock: a three-dimensional hydro-mechanical numerical study. *Int J Rock Mech Min Sci* 43:705–725
- Jacob CE, Lohman SW (1952) Nonsteady flow to a well of constant drawdown in an extensive aquifer. *Trans Am Geophys Union* 33
- Keller F, Schneider TR (1982) Der Furka Basis-Tunnel: Geologie und Geotechnik [The Furka base tunnel: geology and geotechnics]. *Schweizer Ing Architekt* 100:512–520
- Keller F, Wanner H, Schneider TR (1987) Geologischer Schlussbericht Gotthard-Strassentunnel, Zusammenfassung [Final geological report of the Gotthard highway tunnel]. *Beiträge Geol Schweiz Geotech Serie* 70:1–67

- Klemenz W (1974) Die Hydrogeologie des Gebirges im Obergestelnstollen [Hydrogeology of the rock mass in Obergesteln gallery]. Gas-Wasser-Abwasser 54:287–289
- Kohl T, Signorelli S, Rybach L (2000) Constraints on Palaeotopography by revised Apatite FT uplift rates, 25 April 2000, EGS 25th Gen. Assembly, Nice, France
- Labhart TP (1977) Aarmassiv und Gotthardmassiv [Aar and Gotthard massifs]. Borntraeger, Berlin
- Labhart TP (1999) Aarmassiv, Gotthardmassiv und Tavetscher Zwischenmassiv: Aufbau und Entstehungsgeschichte [Aar, Gotthard and Tavetsch massifs: structure and history]. In: Loew S, Wyss R (eds) Vorerkundung und Prognose der Basistunnels am Gotthard und am Lötschberg, Balkema, Rotterdam, pp 31–34
- Laws S (2001) Structural, geomechanical and petrophysical properties of shear zones in the Eastern Aar Massif, Switzerland. PhD Thesis, ETHZ, Switzerland
- Laws S, Loew S, Eberhardt E (2000) Structural make-up and geophysical properties of brittle fault zones in the eastern Aar Massif, Switzerland. International Conference on Geotechnical and Geological Engineering, Melbourne, Australia, November 2000
- Laws S, Eberhardt E, Loew S, Descoeudres F (2003) Geomechanical properties of shear zones in the Eastern Aar Massif, Switzerland and their implication on tunneling. Rock Mech Rock Eng 36:271–303
- Lei S (1999) An analytical solution for steady flow into a tunnel. Ground Water 37:23–26
- Lei S (2000) Steady flow into a tunnel with a constant pressure head. Ground Water 38:643–644
- Loew S (2001) Natural groundwater pathways and models for regional groundwater flow in crystalline rocks. In: Seiler KP, Wohnlich S (eds) New approaches characterizing groundwater flow (Proceedings of the XXXI IAH Congress), Munich, Germany, September 2001
- Loew S (2002) Groundwater hydraulics and environmental impacts of tunnels in crystalline rocks. Paper presented at the IAEG, Durban, South Africa, December 2002
- Loew S, Ziegler H-J, Keller F (2000) Alptransit: engineering geology of the longest tunnel system. GeoEng2000, Melbourne, December 2000, Technomic, Melbourne, Australia

- Loew S, Luetzenkirchen VH, Offerdinger US, Zangerl C, Eberhardt E, Evans KF (2007) Environmental impacts of tunnels in fractured crystalline rocks of the Central Alps. In: Krasny J, Sharp JM (eds) Groundwater in fractured rocks. Selected Papers 9, IAH, Goring, UK, pp 507–526
- Long JCS, Karasaki K, Davey A, Peterson J, Landsfeld M, Kemeny J, Martel S (1991) An inverse approach to the construction of fracture hydrology models conditioned by geophysical data an example from the validation exercises at the Stripa mine. *Int J Rock Mech Min Sci Geomech Abstr* 28:121–142
- Löw S, Ehrminger B, Klemenz W, Gilby D (1996) Abschätzung von Bergwasserzuflüssen und Oberflächenauswirkungen am Beispiel des Gotthard-Basistunnel [Estimation of tunnel inflows and surface effects using the example of Gotthard Base Tunnel]. In: Oddson B (ed) *Instabile Hänge und andere risikorelevante natürliche Prozesse*, Birkhauser, Basel, Switzerland
- Lützenkirchen VH (2002) Structural geology and hydrogeology of brittle fault zones in the Central and Eastern Gotthard Massif, Switzerland. PhD Thesis, ETHZ, Switzerland
- Maréchal JC, Dewandel B, Subrahmanyam K (2004) Use of hydraulic tests at different scales to characterize fracture network properties in the weathered-fractured layer of a hard rock aquifer. *Water Resour Res* 40. doi:10.1029/2004wr003137
- Maréchal JC, Dewandel B, Ahmed S, Galeazzi L, Zaidi FK (2006) Combined estimation of specific yield and natural recharge in a semi-arid groundwater basin with irrigated agriculture. *J Hydrol* 329:281–293
- Marquer PD (1990) Structures et déformation alpine dans les granites hercyniens du massif du Gotthard (Alpes centrales suisses) [Alpine structures and deformation in the Hercynian granites of the Gotthard massif (central Swiss Alps)]. *Eclogae Geol Helv* 83:77–97
- Masset O, Loew S (2007) Spatial distribution of tunnel inflows in the Central Aar and Gotthard Massifs (Switzerland). In: Ribeiro L, Chambel A, de Melo MTC (eds) *XXXV Congress of the International Association of Hydrogeologists, Groundwater and Ecosystems*, Lisbon, Portugal, September 2007
- Mazurek M (1993) Geology of the crystalline basement of Northern Switzerland. Nagra Technical Report NTB 93-12, Nagra, Wettingen, Switzerland
- Meyer J, Mazurek M, Alexander WR (1989) Petrographic and mineralogical characterization of fault zones AU 96 and AU 126. In: Bradbury MH (ed) *Laboratory investigations in support of the migration experiments at the*

- Grimsel test site. Nagra Technical Report NTB 88-23, Nagra, Wettingen, Switzerland
- Molinero J, Samper J, Juanes R (2002) Numerical modeling of the transient hydrogeological response produced by tunnel construction in fractured bedrocks. *Eng Geol* 64:369–386
- Mourzenko VV, Thovert J-F, Adler PM (1996) Geometry of simulated fractures. *Phys Rev E* 53:5606–5626
- Mourzenko VV, Thovert J-F, Adler PM (1999) Percolation and conductivity of self-affine fractures. *Phys Rev E* 59:4265–4284
- Ofterdinger US (2001) Ground water flow systems in the Rotondo Granite, Central Alps (Switzerland). PhD Thesis, ETHZ, Switzerland
- Rutqvist J, Stephansson O (2003) The role of hydromechanical coupling in fractured rock engineering. *Hydrogeol J* 11:7–40
- Schmid SM, Pfiffner OA, Froitzheim N, Schönborn G, Kissling E (1996) Geophysical-geological transect and tectonic evolution of the Swiss-Italian Alps. *Tectonics* 15:1036–1064
- Schneider TR (1974) Geologie und Geotektonik der Stollen und Schächte im Abschnitt Brienzwiler-Griespass [Geology and geotectonics of galleries and shafts in the Brienzwiler-Griespass section]. *Gas-Wasser-Abwasser* 54:278–286
- Schneider TR (1981) Wasserführung in bestehenden Untertagebauten im Kristallin der Zentralmassive und des Penninikums im Tessin und Misox [Groundwater in existing underground constructions in crystalline rocks of the Central Massifs and Peninic units in Tessin and Misox]. NIB 81-02, Nagra, Wettingen, Switzerland
- Steck A (1968a) Die Alpidischen Strukturen in den Zentralen Aaregraniten des westlichen Aarmassivs [The Alpine structures of the granites in the western Aar massif]. *Eclogae Geol Helv* 61:19–48
- Steck A (1968b) Junge Bruchsysteme in den Zentralalpen [Late Alpine faulting in the Central Alps]. *Eclogae Geol Helv* 61:387–393
- Steck A (1984) Structures de déformations tertiaires dans les Alpes Centrales (Transversale Aar-Simplon-Ossola) [Tertiary deformation structures in the Central Alps (Aar-Simplon-Ossola transverse)]. *Eclogae Geol Helv* 77:55–100
- Steck A, Hunziker J (1994) The tertiary structural and thermal evolution of the Central Alps: Compressional and extensional structures in an orogenic belt. *Tectonophysics* 238:229–254

- Stober I (1995) Die Wasserführung des kristallinen Grundgebirges (Groundwater in the crystalline basement). Enke, Stuttgart, Germany
- Stober I (1997) Permeabilities and chemical properties of water in crystalline rocks of the Black Forest, Germany. *Aquat Geochem* 3:43–60
- Stober I, Bucher K (1999) Deep groundwater in the crystalline basement of the Black Forest region. *Appl Geochem* 14:237–254
- Stober I, Bucher K (2007) Hydraulic properties of the crystalline basement. *Hydrogeol J* 15:213–224
- Voborny O, Vomvoris S, Wilson S, Resele G, Hürlimann W (1994) Hydrodynamic synthesis and modeling of groundwater flow in crystalline rocks of northern Switzerland. Nagra Technical Report NTB 92-04, Nagra, Wettingen, Switzerland
- Wang M, Kulatilake PHSW, Panda BB, Rucker ML (2001) Groundwater resources evaluation case study via discrete fracture flow modeling. *Eng Geol* 62:267–291
- Wyss R (1986) Die Urseren Zone: Lithostratigraphie und Tektonik [The Urseren zone: lithostratigraphy and tectonics]. *Eclogae Geol Helv* 79:731–767
- Zangerl CJ (2003) Analysis of surface subsidence in crystalline rocks above the Gotthard highway tunnel, Switzerland. PhD Thesis, ETHZ, Switzerland
- Zangerl C, Loew S, Eberhardt E (2006) Structure, geometry and formation of brittle discontinuities in anisotropic crystalline rocks of the Central Gotthard Massif, Switzerland. *Eclogae Geol Helv* 99:271–290
- Zangerl C, Evans KF, Eberhardt E, Loew S (2008a) Consolidation settlements above deep tunnels in fractured crystalline rock: part 1, investigations above the Gotthard highway tunnel. *Int J Rock Mech Min Sci* 45:1195–1210
- Zangerl C, Eberhardt E, Evans KF, Loew S (2008b) Consolidation settlements above deep tunnels in fractured crystalline rock: part2, numerical analysis of the Gotthard highway tunnel case study. *Int J Rock Mech Min Sci* 45:1211–1225
- Zangerl C, Evans KF, Eberhardt E, Loew S (2008c) Normal stiffness of fractures in granitic rock: a compilation of laboratory and in-situ experiments. *Int J Rock Mech Min Sci* 45:1500–1507
- Zhang L, Franklin JA (1993) Prediction of water flow into rock tunnels: an analytical solution assuming a hydraulic conductivity gradient. *Int J Rock Mech Min Sci* 30:37–46
- Zhao J (1998) Rock mass hydraulic conductivity of the Bukit Timah granite, Singapore. *Eng Geol* 50:211–216

2.14. Tables

Table 2-1-1 References to unpublished reports

Grundner (1942) Geologisch-petrographische Aufnahme der Zuleitung Haslital der Kraftwerk Oberhasli AG [Geological and petrological survey of the Haslital adit of the Oberhasli AG power plant] Stollenaufnahmen 1:1000, Pläne Kraftwerk Innertkirchen, Ablaufkanal, Zentrale, Wasserschloss, Benzlani, Hostet
Hügi T (1961) Zuleitung der Unteralpreuss in den Ritomsee- Zulaufstollen: Geologisches Längsprofil 1:2000/1:200 und Ausführungsplan SBB [Diversion of the Unteralpreuss River to the Ritom Lake-gallery: geological longitudinal profile and Swiss Federal railway project plan]
Loew S, Masset O (2008) Groundwater resources in fractured aquifers of Switzerland: estimations derived from tunnel inflows and surface springs in the Gotthard massif (Switzerland). ETH Report No. 3465/62, ETH, Zurich, Switzerland
SBB Druckstollenkommission (1923) Bericht der Druckstollenkommission über den Druckstollen des Kraftwerks Amsteg [Report of the Pressure Tunnel commission on the pressure tunnel of the Amsteg power plant]. Lage der Versuchsstrecken im Zulaufstollen mit geologischer Diagnose nach Prof Dr Hügi Uebersichtslängenprofil und Lageplan 1:10000/1000 und 1:10000, SBB
Schneider TR (1972) Gotthard Basistunnel: Petrographische Sammelprofile durch das Tavetscher Zwischenmassiv und Gotthardmassiv 1:5000 aufgrund der Aufnahmen in den Stollen der Wasser Kraftwerke Vorderrhein [Gotthard Base Tunnel: petrological profile through the Tavetsch and Gotthard massifs 1:5000 based on the survey of the Vorderrhein hydropower plant galleries]. zusammengestellt von Dal Vesco E. Auswertung der Stollenaufnahmen NOK, Wasseranfall im Horizontalschnitt 1:25000 Unveröffentlichter Bericht 307e/3,5
Schneider TR (1979) Gotthard Strassentunnel: Geologischer Schlussbericht Nordseite IV Bergwasserführung Chemismus und Temperaturen, Geologisches Befundprofil durch Tunnelröhre 1:10000 [Gotthard highway tunnel: final geological report of the northern part number 4—groundwater flow, chemistry and temperatures, geological profile along the tunnel at the 1:10000 scale]. Unveröffentlichter Bericht 305am
Schneider TR (1985) Basis-Tunnel Furka – Geologischer Schlussbericht, Geologische Aufnahme 1:200 des Tunnels Los 62 Realp und Fensters Los 63 Bedretto [Furka base tunnel: final geological report, geological 1:200 scale map of the Realp and Bedretto legs]. Unveröffentlichte Berichte 338f, 338g, 338o

Table 2-1-2 References to unpublished reports

- Stapff FM (1882) Geologische Aufnahme des Gotthard- Bahntunnels: 60 Geologische Tunnelprofile 1:200 (Längen- und Horizontalschnitte) [Geological survey of the Gotthard railway tunnel: 60 geological 1:200 scale vertical and horizontal profiles of the tunnel]. Quartalsberichte zu Handen des Schweizerischen Bundesrates, Geneva
- Voborny O, Resele G, Vomvoris S (1993) Hydrogeology of crystalline rocks of northern Switzerland: synthesis of hydraulic borehole data and assessment of effective properties. Nagra Internal Report NIB 92-87, Nagra, Baden, Switzerland
- Winterhalter RU (1949a) Kraftwerk Wassen: Geologischer Schlussbericht—Geologisches Profil längs des Druckstollens 1:5000 [Wassen power plant: final geological report—geological profile along the pressure gallery at the 1:5000 scale]. Unveröffentlichter Bericht 113b/2
- Wanner H (1982) Galleria Stradale del San Gottardo, Rapporto Finale Lotto Sud: Profilo Idrogeologico attraverso il tunnel stradale del Gottardo 1:10000 [Gotthard highway tunnel, final report of the southern section: hydrogeological profile along the tunnel at the 1:10000 scale]
- Winterhalter RU (1949b) Kraftwerk Lucendo: Geologischer Schlussbericht—Geologisches profil längs des Druckstollens 1:10000 [Lucendo power plant: final geological report— geological profile along the pressure gallery at the 1:10000 scale]. Unveröffentlichte Berichte 47e/3
- Winterhalter RU (1957) Kraftwerk Ritom: Zuleitung der Garegna: Geologischer Schlussbericht, Geologische Stollenaufzeichnungen 1:500 [Ritom power plant: diversion of the Garegna River—final geological report, geological profile of the gallery at the 1:500 scale]. Unveröffentlichter Bericht 109o/1
- Winterhalter RU (1969a) Kraftwerk Göschenen: Geologischer Schlussbericht—Geologische Stollenaufnahme 1:1000 der Zuleitung der Furkareuss und der Zuleitung der Voralpreuss [Goeschenen power plant: final geological report—geological 1:1000 scale profile along the supply gallery from the Furkareuss and the Voralpreuss rivers]. Unveröffentlichte Berichte 122v/3-1,4 122v/4,1
- Winterhalter RU (1969b) Kraftwerk Göschenen: Geologischer Schlussbericht—Herkunft der Gesteinproben und Wasseranfall 1:10000, geologisches Profil durch die Zuleitung Furkareuss 1:10000 [Goeschenen power plant: final geological report—origin of the rock samples and inflows at the 1:10000 scale, geological profile along the supply gallery of the Furkareuss River 1:10000]. Unveröffentlichte Berichte 122v/2-1,4-10
- Winterhalter RU, Dal Vesco E (1961) Gotthardtunnel SBB, Vortrieb und Wasseranfall [Gotthard railway tunnel, excavation and inflows]. Unveröffentlichter Plan, 215a/6

Table 2-2 Basic tunnel and gallery information: Furka base tunnel, Gottard SBB, Gotthard A2 highway tunnel

Tunnel name	Furka base tunnel		Gotthard SBB	Gotthard A2 highway tunnel	
Tube/gallery name	Realp leg	Bedretto leg	Railway tunnel	Security gallery	Main gallery
References	a	a	b, c	b, d	b, d
Excavation date	1973 – 1978	1973 – 1978	1872 – 1880	1980	1980
Survey date	From 1975	–	–	–	–
Delay	3 weeks – months	3 weeks	months – years	1 day – 4 months	3 weeks
Portal location(s) and elevation(s) [m]	Realp 1,550	Bedretto 1,480	Goeschenen 1,106 Airolo 1,142	Goeschenen 1,080 Airolo 1,146	Goeschenen 1,080 Airolo 1,146
Inflow reported by	Classes	Classes	Classes/rates	Classes	Classes
Drip. zone classes	LDZ/ HDZ	LDZ/ HDZ	LDZ/ HDZ	LDZ/ HDZ	LDZ/ HDZ
Assigned rates [l/s]	0.001/ 0.01	0.001/ 0.01	0.02/ 0.3	0.01/ 0.1	0.01/ 0.1
Inflow classes [l/s]	<1/ 1–10/ >10	<1/ 1–10/ >10	N section/ S section	<0.1 (N section only)/ 0.1–1/ >1	<0.1 (N section only)/ 0.1–1/ >1
Assigned rates [l/s]	0.3/3/25	0.3/3/25	1.9–2.2/ 3.2–4.9	0.03/0.3/3	0.03/0.3/3
Reported rates [m]	–	–	–	–	–
Rate error [l/s]	$\Delta Q=2Q$	$\Delta Q=2Q$	$\Delta Q=3Q$	$\Delta Q=2Q$	$\Delta Q=2Q$

LDZ light dripping zone, HDZ heavy dripping zone

^a Keller and Schneider (1982); Schneider 1985, unpublished report, see Table 1

^b Schneider 1979, unpublished report, see Table 1

^c Stapff 1882, unpublished report (see Table 1); Winterhalter and Dal Vesco 1961, unpublished report (see Table 1)

^d Wanner 1982, unpublished report (see Table 1)

Table 2-3 Basic tunnel and gallery information: KW Amsteg, KW

Tunnel name	KW Amsteg	KW Lucendro
Tube/gallery name	Supply gallery	Pressure gallery
References ^a	SBB Druckstollenkommission 1923	Winterhalter 1949b
Excavation date	–	–
Survey date	–	–
Delay	3 weeks	–
Portal location(s) and elevation(s) [m]	Pfaffensprung 791 Amsteg 530	Lucendro 2,033 Airolo 1,768
Inflow reported by	Classes	Classes
Drip. zone classes	DZ	DZ
Assigned rates [l/s]	–	0.01
Inflow classes [l/s]	Continuous inflow	Not reported
Assigned rates [l/s]	2.2	–
Reported rates [l/s]	–	–
Rate error [l/s]	–	–

DZ dripping zone

^a Unpublished reports (see Table 1)

Table 2-4 Basic tunnel and gallery information: KW Goeschenen and KW Wassen

Tunnel name Tube/gallery name	KW Goeschenen			KW Wassen
	Pressure drift	Furkareuss supply gallery	Voralpreuss supply gallery	Supply gallery
References ^a	Winterhalter 1969b	Winterhalter 1969b	Winterhalter 1969a	Winterhalter 1969a
Excavation date	–	1956–1958	1956–1957	–
Survey date	1958	1958	1958	–
Delay	–	3 weeks	3 weeks	–
Portal location(s) and elevation(s) [m]	Goescheneralp 1,690 Goeschenen 1,100	Furkareuss 1,800 Goescheneralp 1,792	Voralpreuss Goescheneralp 1,792	Close to Wassen ~796
Inflow reported by	Classes	Classes	Classes	Classes
Drip. zone classes	LDZ/HDZ	DZ	LDZ/HDZ	Not reported
Assigned rates [l/s]	0.001/0.01	0.01	0.001/0.01	–
Inflow classes [l/s]	Continuous inflow	<0.1/0.1–1/>1	–	Continuous inflow
Assigned rates [l/s]	2.2	0.03/0.3/3	–	2.2
Reported rates [l/s]	–	–	Yes	–
Rate error [l/s]	–	$\Delta Q=2Q$	$\Delta Q=Q/2$	–

^a Unpublished reports (see Table 1)

Table 2-5 Basic tunnel and gallery information: Gas Transit

Tunnel name	Gas Transit		
Tube/gallery name	Urweid gallery	Gstelli gallery	Obergesteln gallery
References ^a	Schneider (1974)	Schneider (1974)	Schneider (1974)
Excavation date	1972	1972–1973	Feb 1972—May 1973
Survey date	March 1973	1973	–
Delay	3 weeks	3 weeks	Several months
Portal location(s) and elevation(s) [m]	Close to Urweid ~800	Close to Guttannen ~1,150	Close to Obergesteln ~1,350
Inflow reported by	Classes	Classes/rates	Classes
Drip. zone classes	DZ	DZ	DZ
Assigned rates [l/s]	0.01	0.01	0.01
Inflow classes [l/s]	<1/>1	–	–
Assigned rates [l/s]	0.3/3	–	–
Reported rates [l/s]	–	Yes	Yes
Rate error [l/s]	$\Delta Q=2Q$	$\Delta Q=2Q$	$\Delta Q=Q$

^a Unpublished reports (see Table 1)

Table 2-6 Basic tunnel and gallery information: KW Oberhasli and KW Ritom

Tunnel name	KW Oberhasli	KW Ritom		
Tube/gallery name	Gadmenwasser supply gallery	Handegg supply gallery	Unteralpreuss supply gallery	Garegna supply gallery
References ^a	–	Grundner 1942	Hügi 1961	Winterhalter 1957
Excavation date	–	–	1955–1958	1947–1955
Survey date	–	–	–	–
Delay	3 weeks	3 weeks	3–39 months	
Portal location(s) and elevation(s) [m]	Gadmental 1,342 Handegg gallery 1,290	Handegg ~1,400 Innertkirchen ~625	Unteralpreuss Lake Ritom ~1,850	
Inflow reported by	Classes	Classes/rates	Classes/rates	Classes
Drip. zone classes	–	–	LDZ/HDZ	–
Assigned rates [l/s]	–	–	0.001/0.1	–
Inflow classes [l/s]	Continuous inflow	Continuous inflow	–	Continuous inflow
Assigned rates [l/s]	5	0.6	–	5
Reported rates [l/s]	–	NW part only	Yes	–
Rate error [l/s]	–	$\Delta Q=Q/2$ or $2Q$	$\Delta Q=Q/2$	$\Delta Q=2Q$

^a Unpublished reports (see Table 1)

Table 2-7 Basic tunnel and gallery information: KW Vorderrhein

Tunnel name	KW Vorderrhein				
Tube/gallery name	Val Val – Curnera gallery	Nalps – Sedrun gallery	Curnera – Nalps gallery	Sedrun – Medels gallery	Santa Maria – Nalps gallery
References	a	a	a	a	a
Excavation date	-	-	-	-	-
Survey date	-	-	-	-	-
Delay	3 weeks	3 weeks	3 weeks	3 weeks	3 weeks
Portal location(s) and elevation(s) [m]	Val ValCurnera ~1,950	Nalps ~1,900; Sedrun ~1,400	Curnera ~1,950; Nalps ~1,900	Sedrun ~1,400 Medels	Santa Maria Nalps ~1,900
Length [m]	5,700	3,600	3,600	6,200	8,600
Inflow reported by	rates	rates	rates	rates	rates
Drip. zone classes	-	-	-	-	-
Assigned rates [l/s]	-	-	-	-	-
Inflow classes [l/s]	-	-	-	-	-
Assigned rates [l/s]	-	-	-	-	-
Reported rates [l/s]	Yes	Yes	Yes	Yes	Yes
Rate error [l/s]	$\Delta Q=2Q$	ΔQ	ΔQ	ΔQ	ΔQ

^a Unpublished reports (see Table 1)

Table 2-8 Geological units and their corresponding abbreviations

Tectonic unit	Geological unit	Abbreviation
Aar massif	"Innertkirchner-Kristallin"	AIK
	Northern "Altkristallin"	ANG
	Granite sensu lato	AAG
	Southern "Altkristallin"	ASG
Tavetsch massif		TZM
Gotthard massif	"Urseren-Garvera-Zone"	UGZ
	Northern "Altkristallin"	GAK
	Variscan intrusives	GHG
	Southern "Altkristallin"	GSG
	Southern sedimentary cover	GMB

Table 2-9 Air water vapor content parameters and results

Parameters	Units	Tunnel sections			
		SW	SE	NW	NE
Air volumetric flow rate	A [m ³ /s]	42	43.8	45	44.9
Absolute pressure	P [Pa]	96,200	96,200	96,300	96,300
Absolute temperature	Temp [K]	300.9	299.6	297.2	298.4
Water vapor partial pressure	Pw [Pa]	2,060	1,300	1,730	1,600
Air water content #1	c1 [kg/kg]	0.0127	0.0100	0.0084	0.0107
Air water content #2	c2 [kg/kg]	0.0189	0.0152	0.0125	0.0147
Tunnel section length	L [m]	2,300	2,500	1,300	1,300
Gas constant for air	RL [J/(kg × K)]	287.1	287.1	287.1	287.1
Tunnel radius	r [m]	5	5	5	5
Hydraulic head	h [m]	1,000	1,000	1,000	1,000
Gas constant for wet air	Rf [J/kg × K]	289.4	288.6	289.1	288.9
Density	ρ [kg/m ³]	1.10	1.11	1.12	1.12
Vapor mass flow rate	m [kg/s]	46.4	48.7	50.4	50.2
Air water content difference	Δc [kg/kg]	0.0062	0.0052	0.0041	0.0040
Vapor volumetric flow rate	V [l/s]	0.29	0.25	0.21	0.20
Vapor vol. flow rate per m	V2 [l/s/m]	1.25×10 ⁻⁴	1.01×10 ⁻⁴	1.59×10 ⁻⁴	1.54×10 ⁻⁴
Vapor vol. flow rate per 100 m	V3 [l/s/hm]	0.01	0.01	0.02	0.02
Transmissivity per 100 m	T [m ² /s]	1.19×10 ⁻⁸	9.66×10 ⁻⁹	1.52×10 ⁻⁸	1.47×10 ⁻⁸
Hydraulic conductivity	K [m/s]	1.19×10 ⁻¹⁰	9.66×10 ⁻¹⁰	1.52×10 ⁻¹⁰	1.47×10 ⁻¹⁰

2.15. Figures

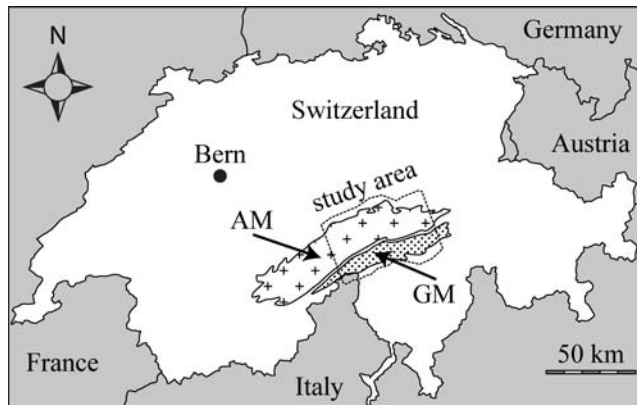


Figure 2-1 Sketch of Switzerland showing the perimeter of the study area (tilled line) and the location of the Aar massif (AM) and Gotthard massif (GM)

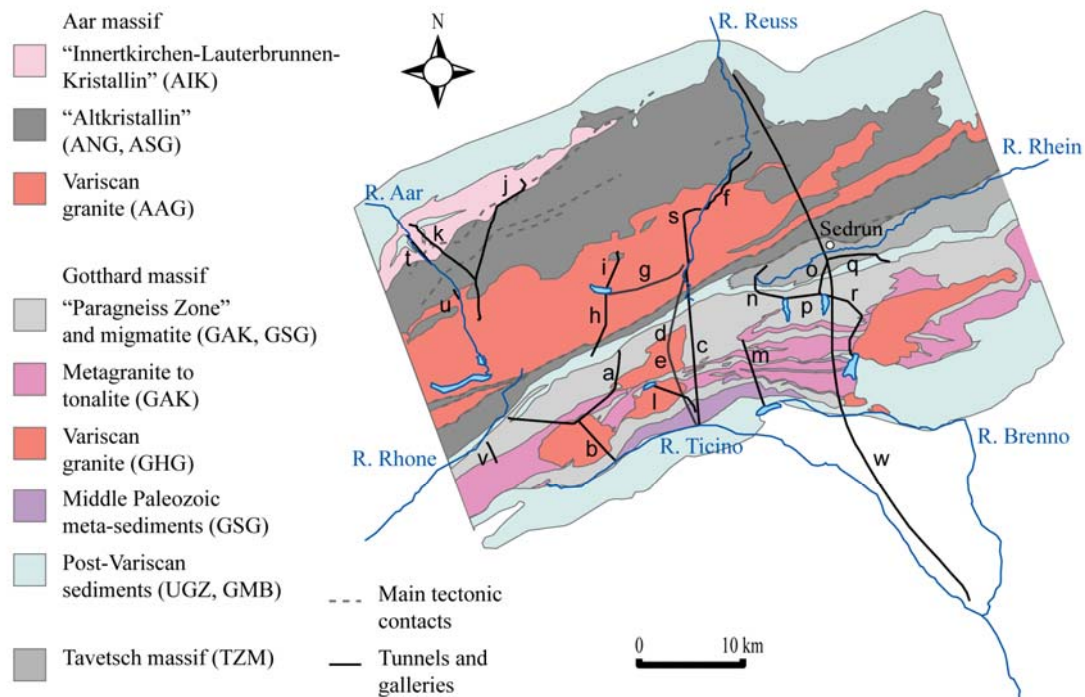


Figure 2-2 Map of the study area showing the main rivers, the main lithologies (their corresponding geological units, modified from Labhart(1999), the main tectonic units and tectonic contacts with black lines representing: Furka base tunnel Realp leg (a); Furka base tunnel Bedretto window gallery (b); Gotthard SBB railway tunnel (c); Gotthard A2 highway security gallery (d); Gotthard A2 highway main tunnel (e); KW Amsteg supply gallery (f); KW Goeschenen pressure gallery (g); KW Goeschenen Furkareuss supply gallery (h); KW Goeschenen Voralpreuss supply gallery (i); KW Oberhasli Gadmenwasser supply gallery (j); KW Oberhasli Handegg supply gallery (k); KW Lucendro pressure gallery (l); KW Ritom Garegna and Unteralpreuss supply galleries (m); KW Vorderrhein Val Val-Curnera gallery(n); KW Vorderrhein Tgom-Nalps gallery (o); KW Vorderrhein Curnera-Nalps gallery (p); KW Vorderrhein Sedrun-Medels gallery (q); KW Vorderrhein Nalps-St Maria gallery (r); KW Wassen supply gallery (s); Gas Transit Urweid gallery (t); Gas Transit Gstelli gallery (u); Gas Transit Obergesteln gallery (v); Gotthard Base Tunnel (under construction) (w)

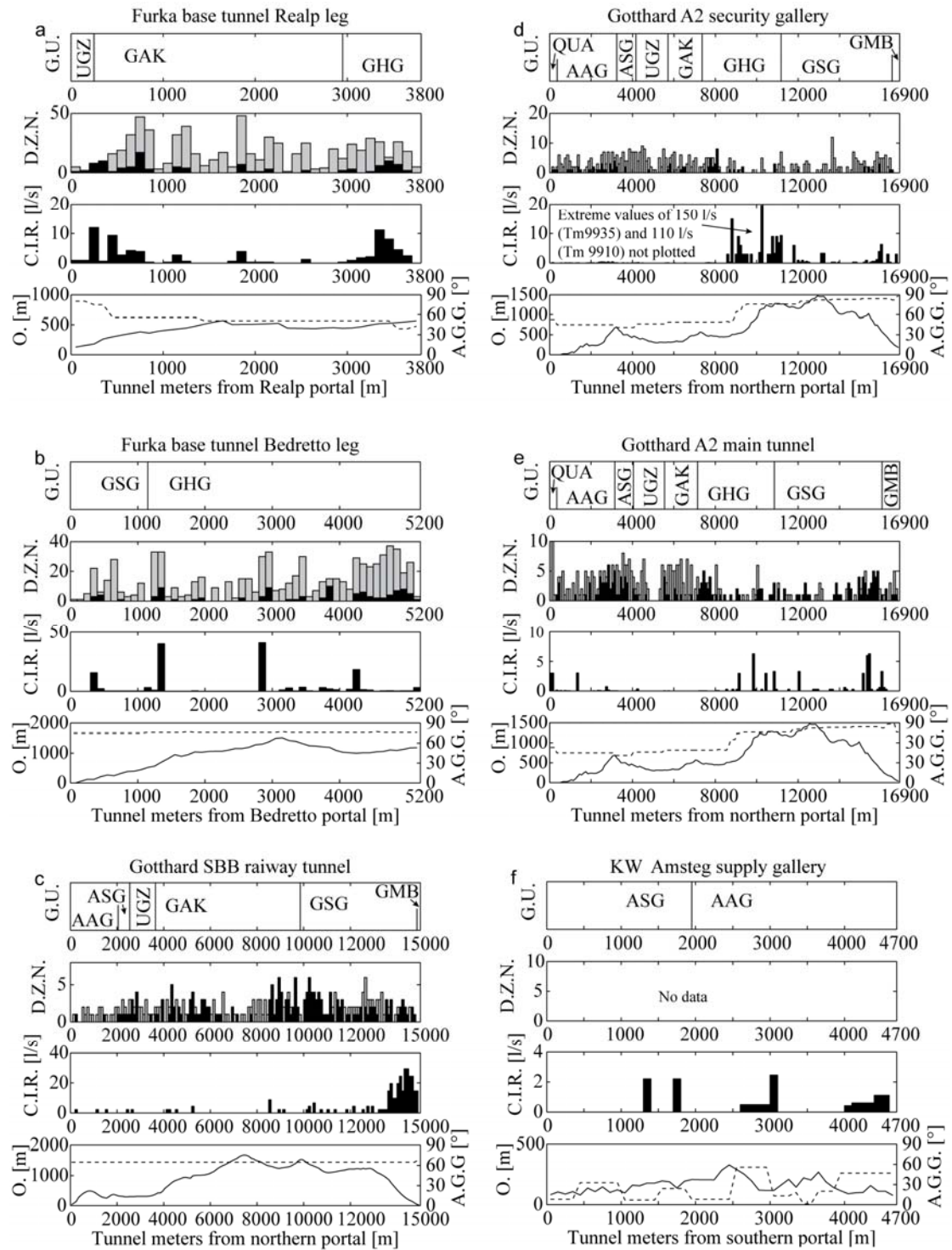


Figure 2-3 Location plot of the geologic boundaries (GU) along the tunnel, bar chart of the number of dripping zones (grey: light dripping zone; black: heavy dripping zone) per 100 m of tunnel (DZN), bar chart of the continuous inflow rate per 100 m of tunnel (CIR) and plot of the depth (D, continuous line) and the angle between the tunnel axis and the Alpine main foliation (AGG, dashed line) along the tunnel for all underground excavations discussed in this paper. a–v The labels of each part correspond to the labels for the tunnels listed in the Figure 2 caption

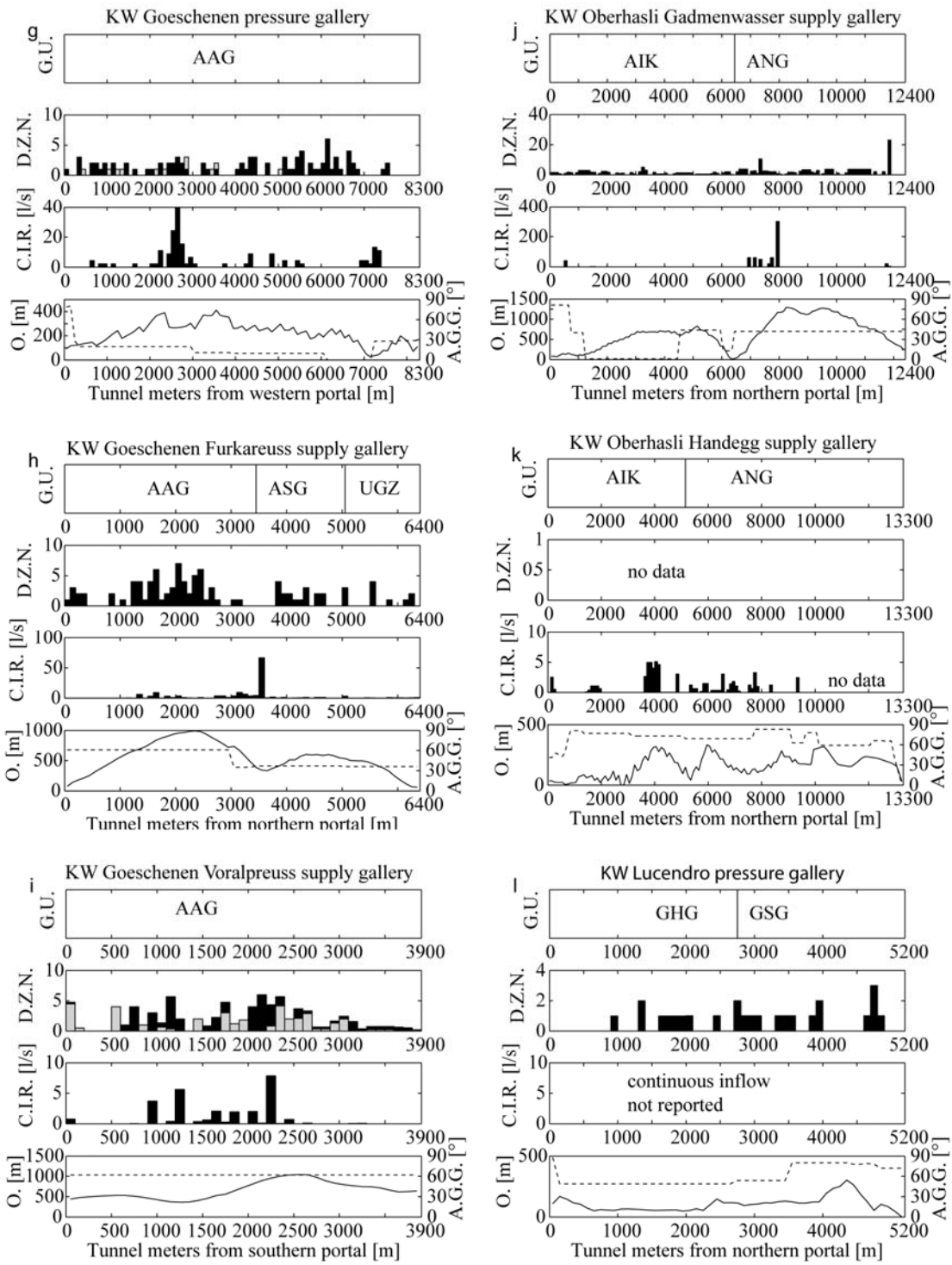


Figure 2-3 (continued)

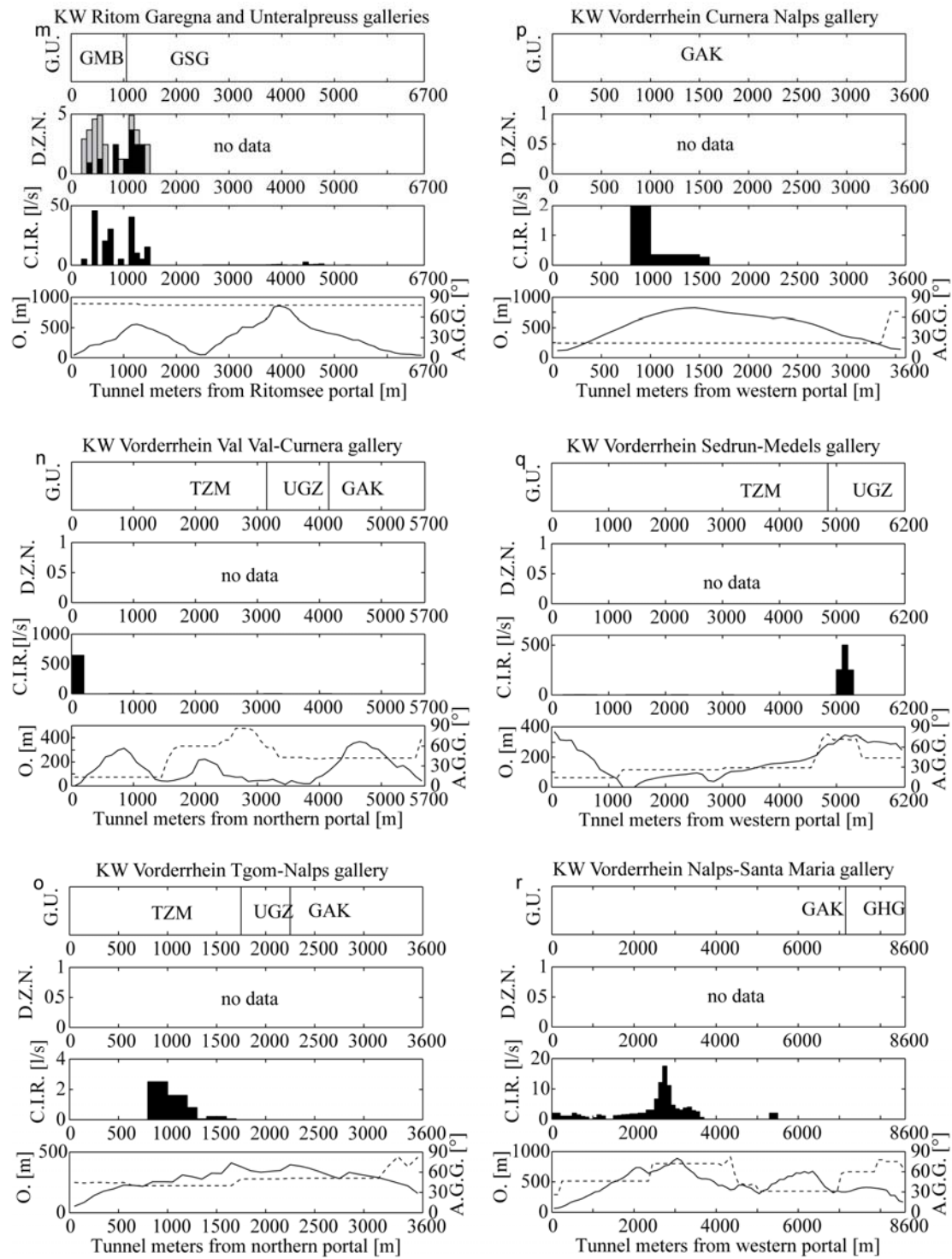


Figure 2-3 (continued)

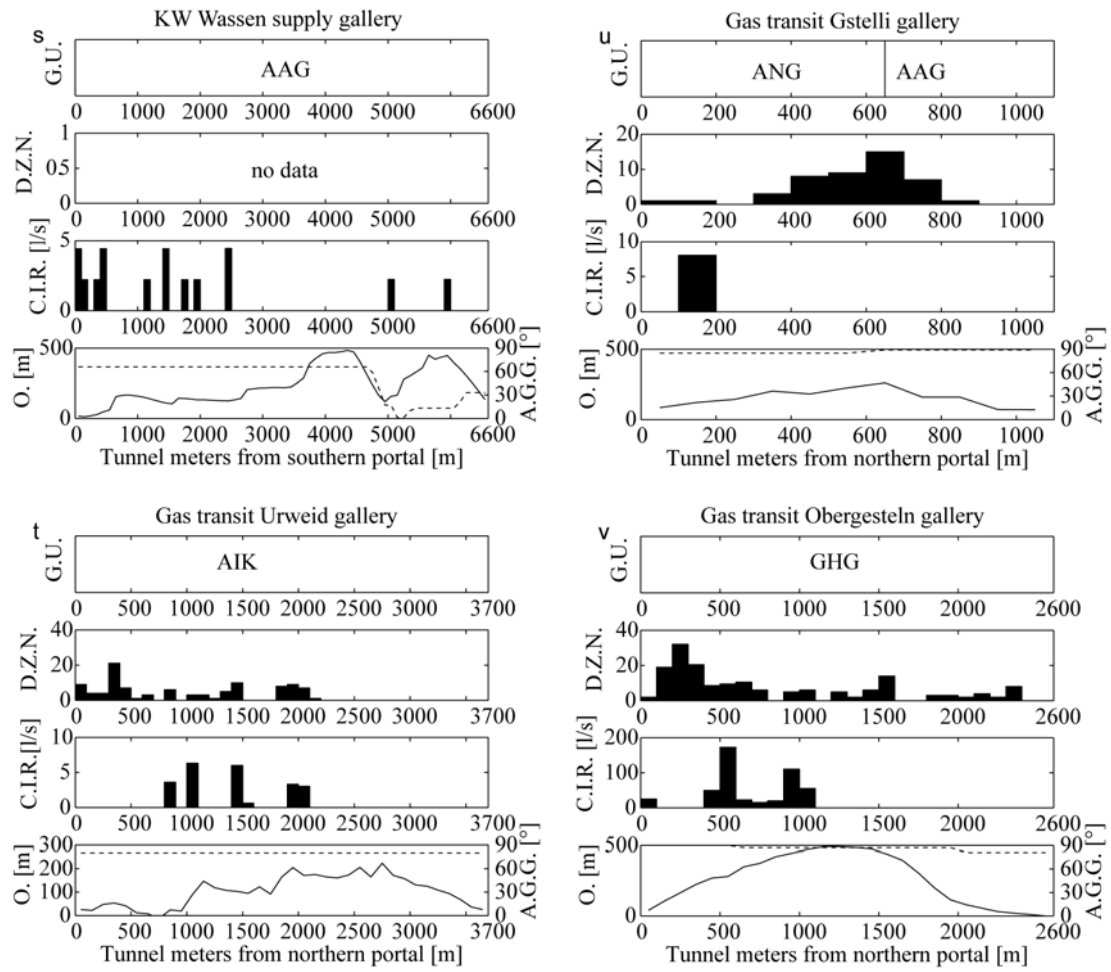


Figure 2-3 (continued)

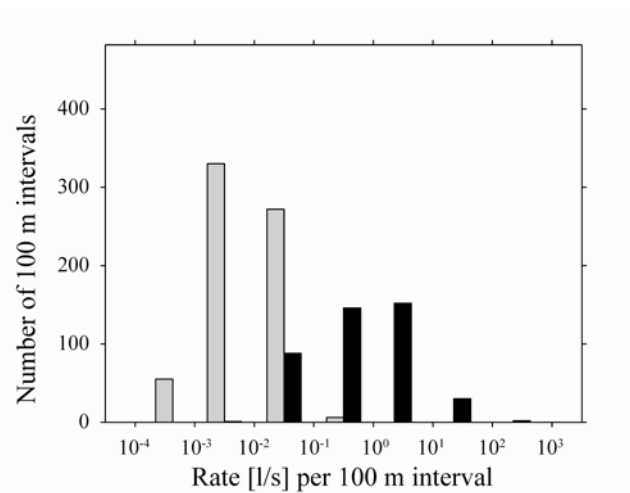


Figure 2-4 Histogram showing dripping inflow rates (grey) and continuous inflow rates (black) for all geologic units

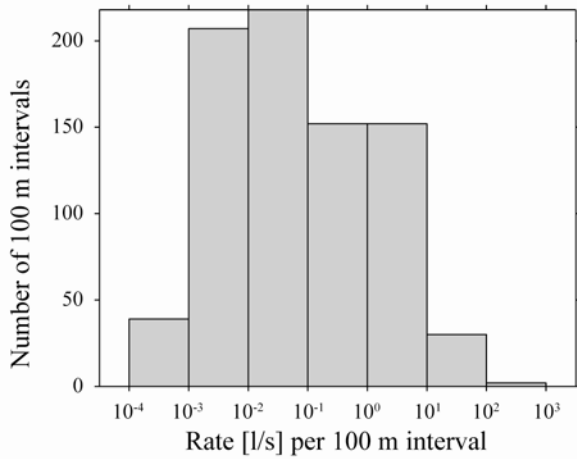


Figure 2-5 Histogram showing dripping and continuous inflow rates for all geologic units

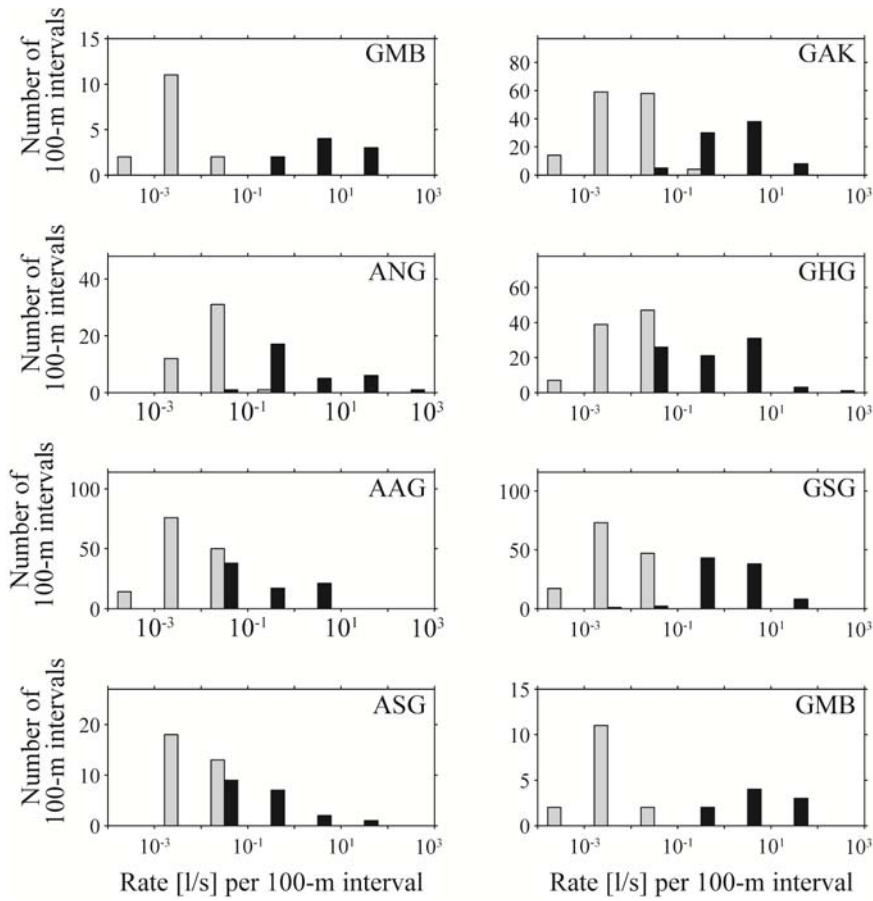


Figure 2-6 Histogram showing dripping inflow rates (grey) and continuous inflow rates (black) for each geologic unit

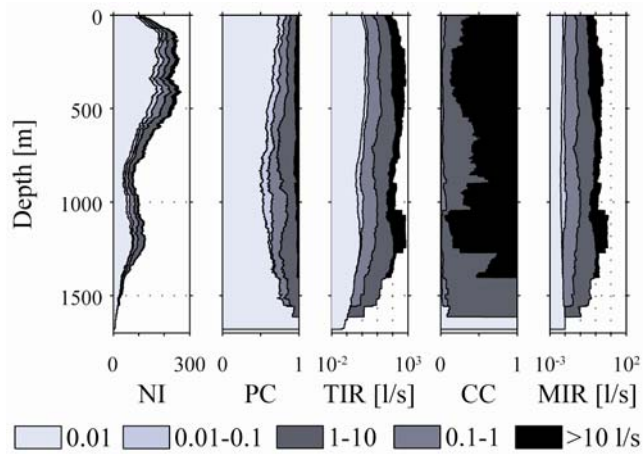


Figure 2-7 All geologic units: Moving average (200 m) of the number of intervals (NI) of the different rate classes (0.01, 0.01–0.1, 0.1–1, >10 l/s) with depth, moving average of the proportion of the different rate classes (PC) with depth, moving average of the total inflow rate (TIR) with depth, moving average of the class contribution (CC) to the total rate with depth and moving average of the mean inflow rate per 100-m interval (MIR) with depth

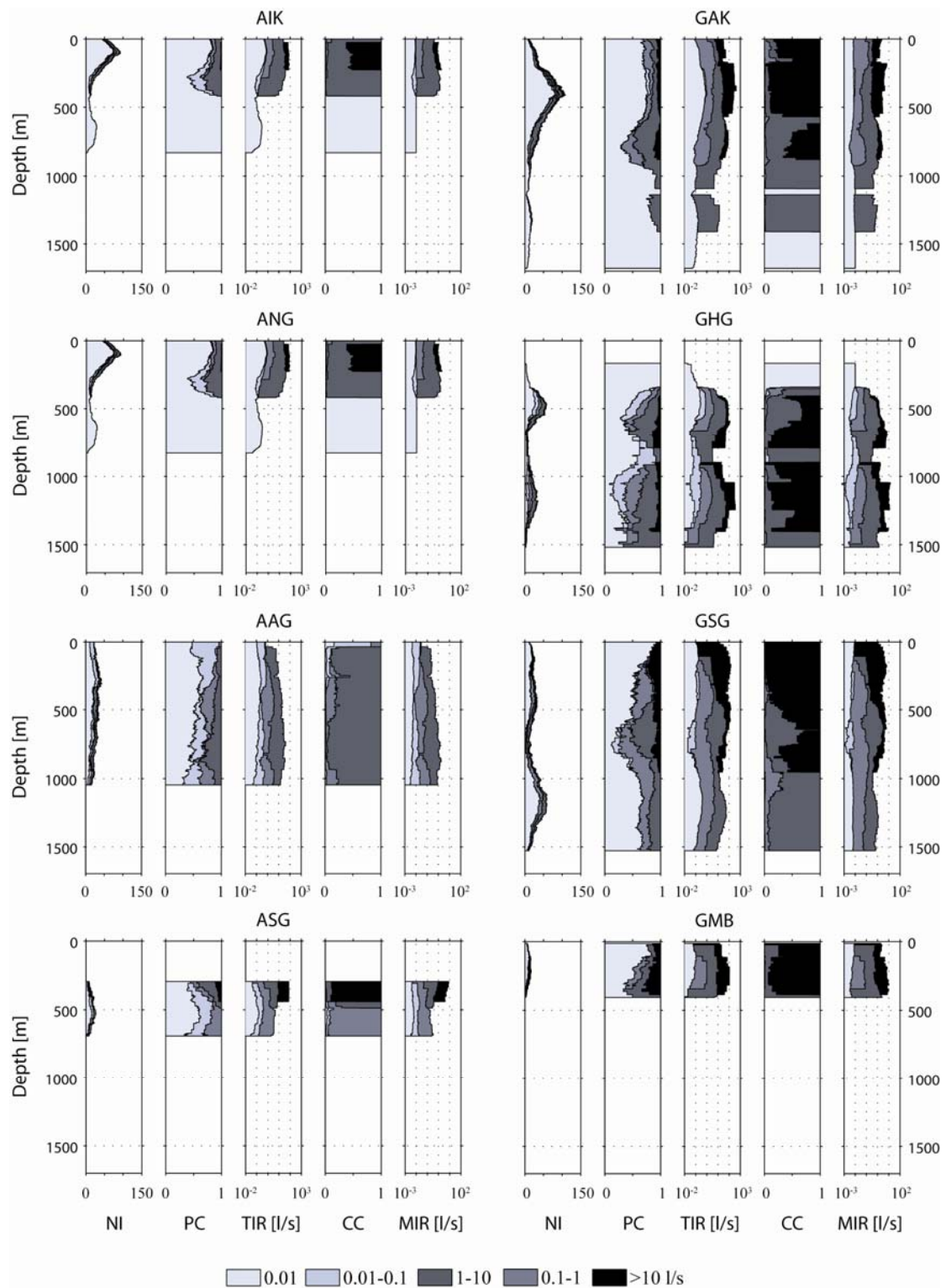


Figure 2-8 Individual geologic units: Moving average (200 m) of the number of intervals (NI) of the different rate classes (0.01, 0.01–0.1, 0.1–1, >10 l/s) with depth, moving average of the proportion of the different rate classes (PC) with depth, moving average of the proportion of the different rate classes (PC) with depth, moving average of the total inflow rate (TIR) with depth, moving average of the class contribution (CC) to the total rate with depth and moving average of the mean inflow rate per 100-m interval (MIR) with depth (see Table 8 for explanation of abbreviations)

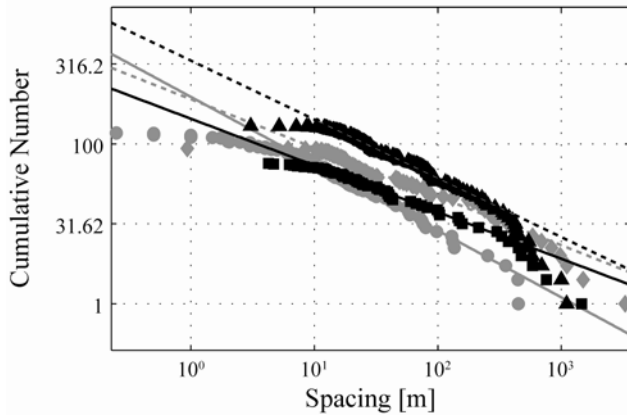


Figure 2-9 Continuous inflow spacing distribution fitted by power laws along the Realp leg of Furka base tunnel (grey circles, grey line), the Gotthard SBB railway tunnel (grey diamonds, dashed grey line), the Gotthard A2 security gallery (black triangles, dashed black line) and the Goeschenen pressure drift (black squares, black line)

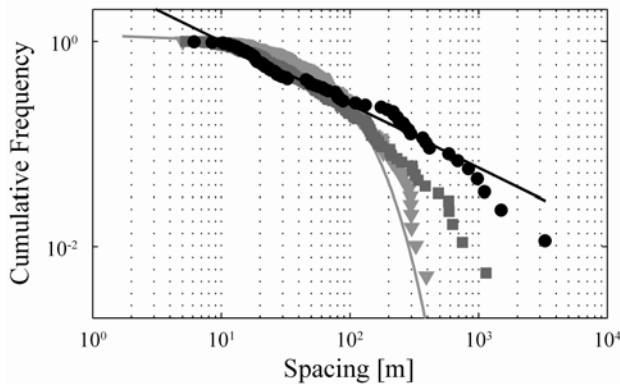


Figure 2-10 Gotthard SBB railway tunnel spacing distributions of light dripping zones (pale grey triangles) fitted by an exponential curve (pale grey curve), heavy dripping zones (dark grey squares) and continuous inflows (black circles) fitted by a power law (black line)

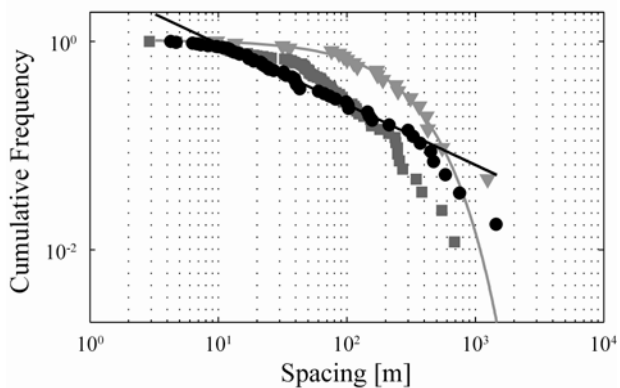


Figure 2-11 Goeschenen pressure drift spacing distributions of light dripping zones (pale grey triangles) fitted by an exponential curve (pale grey curve), heavy dripping zones (dark grey squares) and continuous inflows (black circles) fitted by a power law (black line)

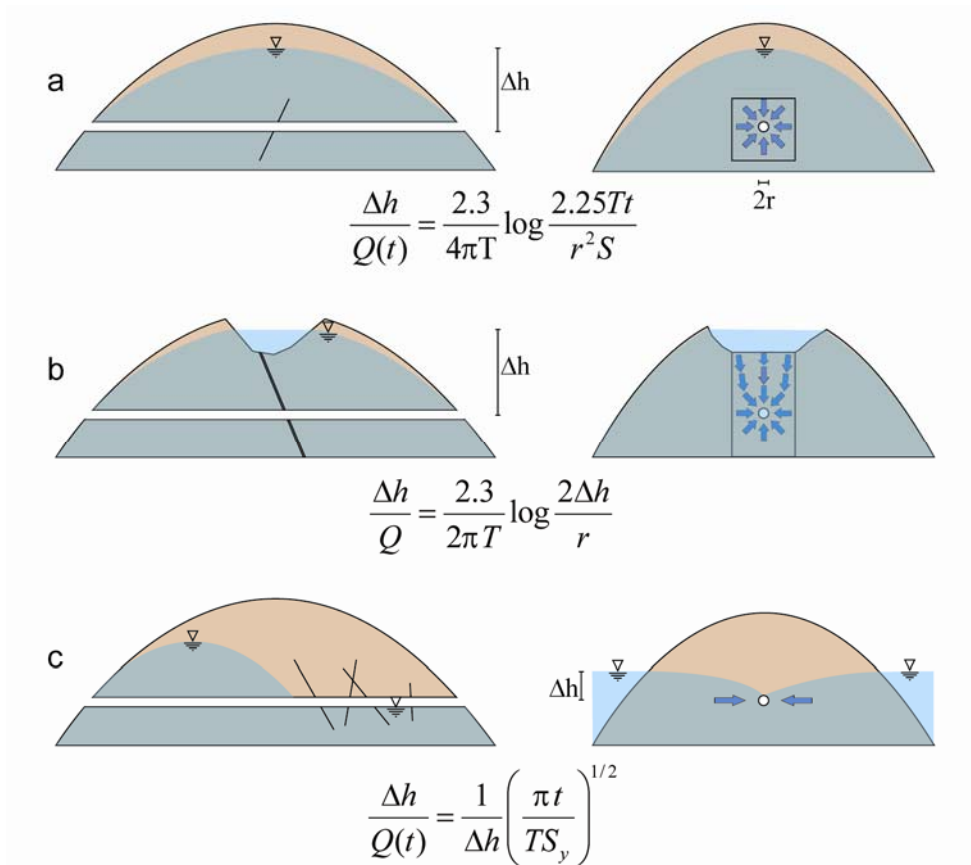


Figure 2-12 EPM (equivalent porous medium) transmissivity model sketches and formulas for a the radial flow without recharge transmissivity model, b the radial flow with constant head boundary transmissivity model, c the linear flow with variable water-table transmissivity model

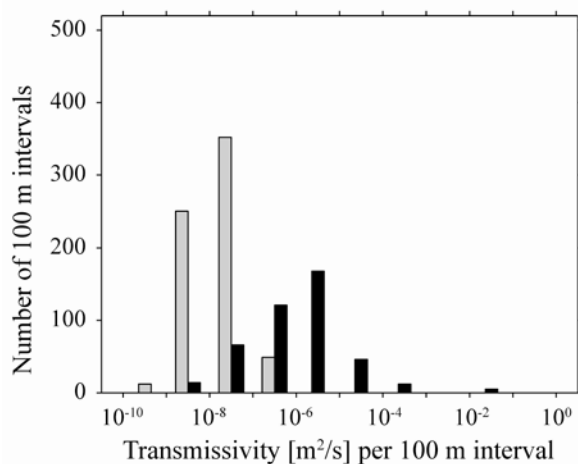


Figure 2-13 Histogram showing transmissivity values derived from dripping inflow rates (grey) and continuous inflow rates (black) for all geologic units

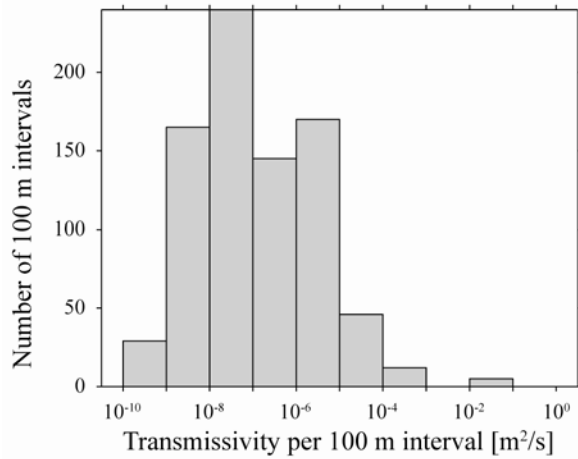


Figure 2-14 Histogram showing transmissivity values derived from dripping inflow rates (grey) and continuous inflow rates (black) for all geologic units

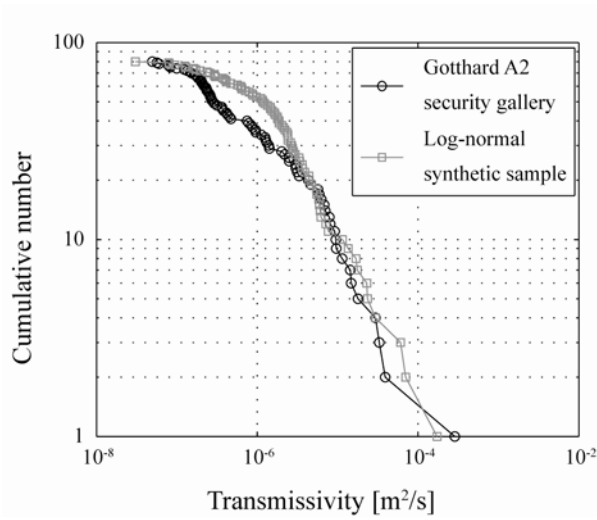


Figure 2-15 Transmissivity cumulative plot for Gotthard A2 security gallery (black) compared with a log-normally distributed synthetic sample of same size, mean and variance (grey)

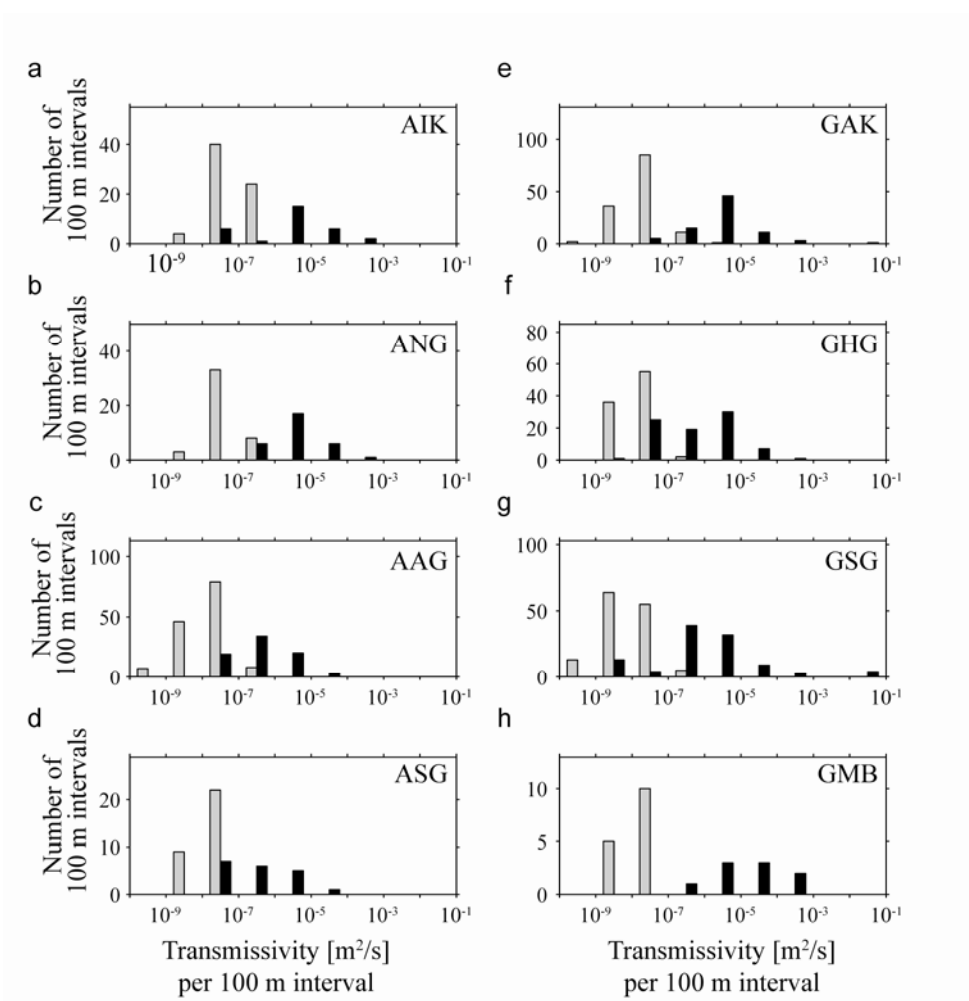


Figure 2-16 Histograms showing transmissivity values derived from the dripping inflow rates (grey) and from the continuous inflow rates (black) for each geologic unit

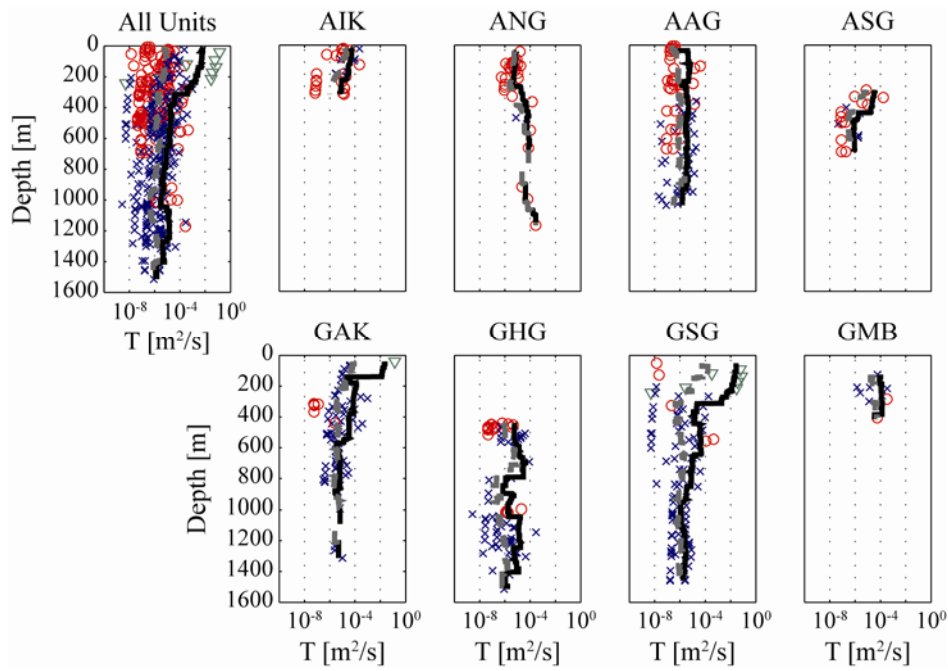


Figure 2-17 Plots of the transmissivity values derived with the radial flow without recharge transmissivity model (model 1, blue crosses), the radial flow with constant head boundary transmissivity model (model 2, red circles) and the linear flow with variable water table transmissivity model (model 3, green triangles) versus depth with logarithmic (dashed grey line) and arithmetic (black line) moving averages (200 m) for all geologic units and for each of them

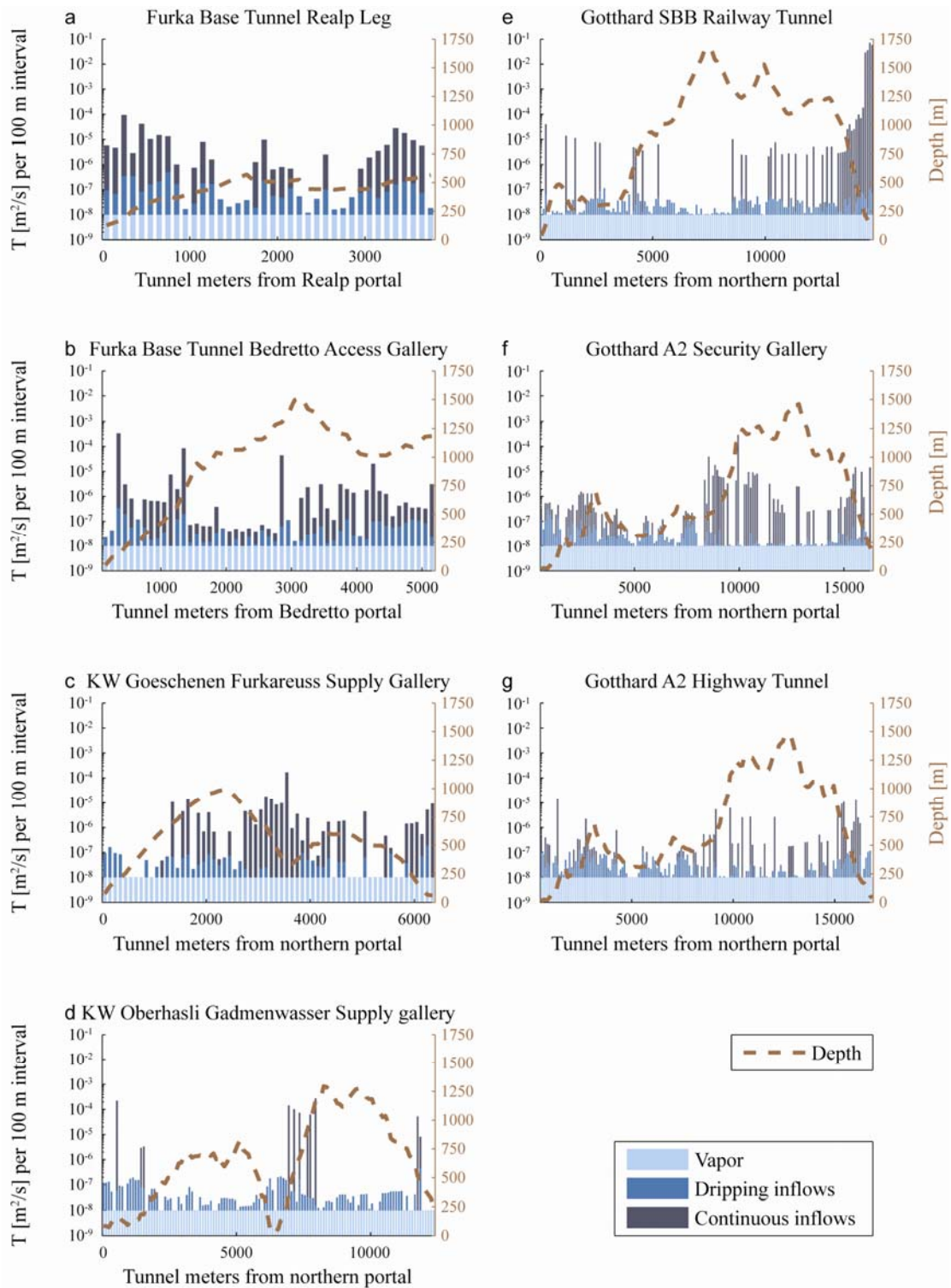


Figure 2-18 Transmissivity distribution along tunnel with dark blue bars, representing transmissivity values derived from continuous inflow rates stacked onto medium blue bars, representing transmissivity values derived from dripping inflow rates, finally stacked onto light blue bars, representing the minimum transmissivity derived from water vapor output measurements in the Gotthard Base Tunnel, for selected tunnels: a, b, h, j, c, d and e (see Figure 2 caption)

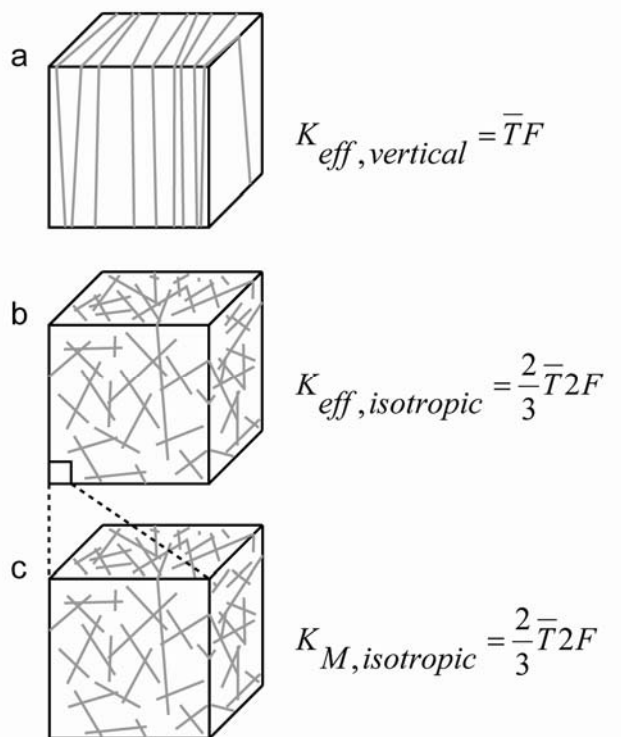


Figure 2-19 EPM hydraulic conductivity model sketches and formulas for a the vertical fracture hydraulic conductivity model, b the isotropic fracture hydraulic conductivity model and c the isotropic matrix hydraulic conductivity model

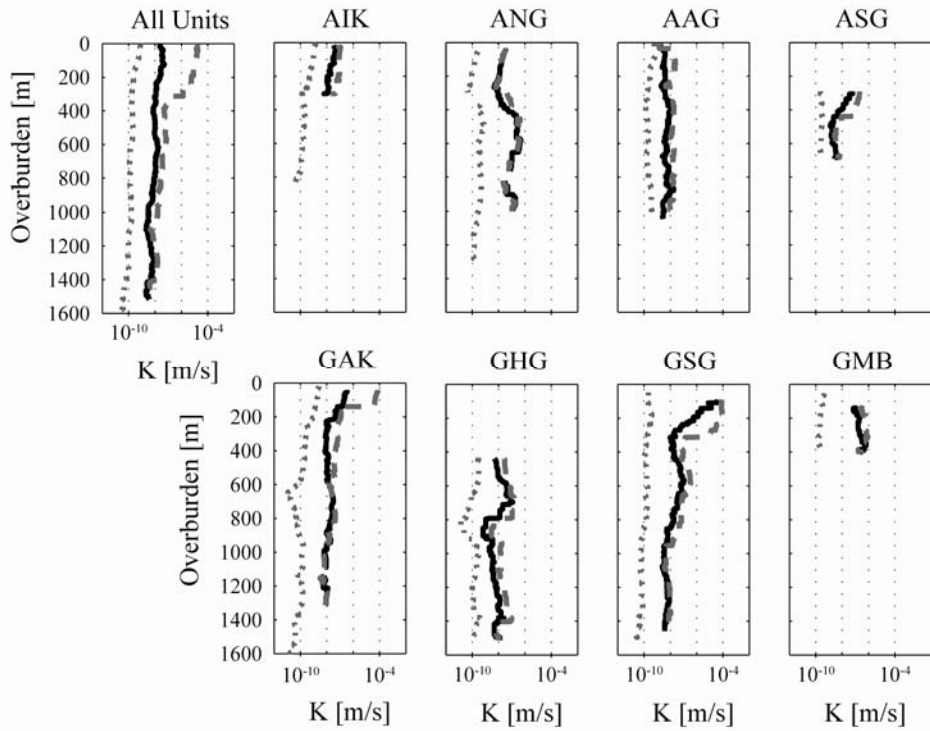


Figure 2-20 Plots of the hydraulic conductivity values derived with the isotropic fracture hydraulic conductivity model (black line), the vertical fracture hydraulic conductivity model (dashed grey line) and the isotropic matrix hydraulic conductivity model (dotted grey line) for all geologic units and for each of them

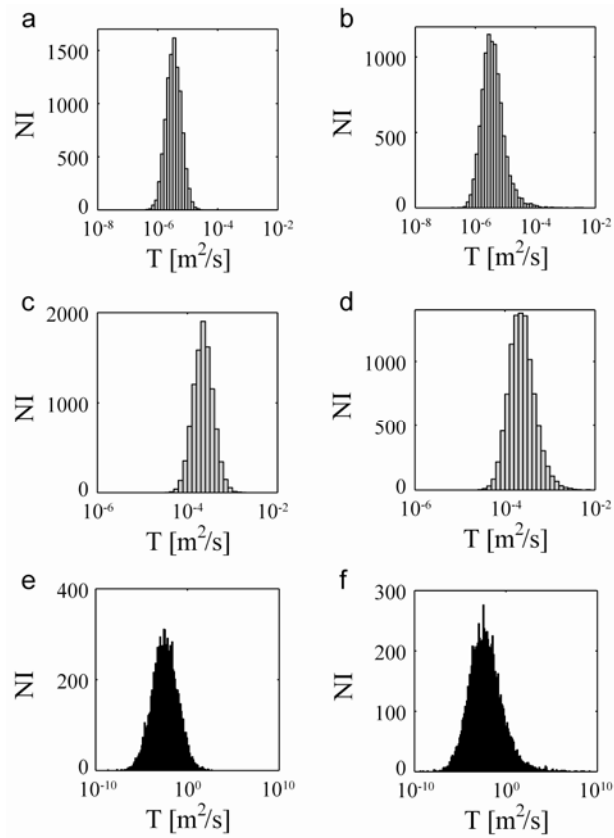


Figure 2-21 Plots of simulated transmissivity distributions for: a the 1,400–1,500-m interval of KW Oberhasli Gadmenwasser supply gallery (radial flow without recharge transmissivity model) with best-guess parameter standard deviations; b the same interval with worst-case parameter standard deviations; c the interval 500–600 m of the same gallery (radial flow with constant head boundary transmissivity model) with best-guess parameter standard deviations and; d the same interval with worst-case parameter standard deviations; e the 14,400–14,500-m interval of Gotthard SBB railway tunnel (linear flow transmissivity model) with best-guess parameter standard deviations; f the same interval with worst-case parameter standard deviations

3. Analysis of inflow rates to pre-drillings of Gotthard Base Tunnel (Sedrun section, Switzerland)

3.1. Abstract

A systematic pre-drilling (sub-horizontal drilling ahead of the excavation front) campaign was undertaken during the excavation of the Sedrun lot of the Gotthard Base Tunnel. The section covered by the systematic drilling campaign extends over 5 km. The depth of the section ranges from 897 to 2026 m and the lithology mainly consists of various gneisses. The pre-drillings include 30 cored and 94 destructive drillings distributed along the two parallel tubes constituting the tunnel. The length of the boreholes ranges from 17.5 to 358.5 m.

The authors present a new methodology to quantitatively analyze inflow and pressure data from pre-drillings for transmissivity and hydraulic conductivity estimation. Hydraulic conductivity values of 50 m long sections of the tunnel are back-calculated from inflow rate and pressure measurements from pre-drillings, using the Jacob and Lohman solution for the transient inflow rate to a well of constant drawdown in a confined aquifer.

Uncertainties with respect to the derived hydraulic conductivity values are estimated through Monte Carlo analysis. In the context of the study the uncertainty mainly comes from uncertainties related to specific storage and pore-pressure values. Derived hydraulic conductivity values range from 10^{-10} to 10^{-6} m/s. The analysis of the distribution of hydraulic conductivity along the two tubes constituting the tunnel shows that the conductive intervals are located independently from the position of major fault zones. Furthermore the correlation between the hydraulic conductivity values of each tunnel tube is weak, suggesting a limited extend for the conductive structures.

3.2. Introduction

The inflow rate to underground excavations has always been a concern in the fields of deep tunneling and mining. The prediction of the inflow rate is, for example, essential to design the drainage system and dimension the pumping devices but also to prevent the occurrence of large inflows endangering the life

of miners and the stability of the excavation. Examples of such large inflow surges are numerous in underground excavations of the Central Swiss Alps (Masset and Loew 2010).

To better understand the inflow spatial and temporal rates, a detailed physical description of the rock mass surrounding the underground excavation is needed. The main hydraulic parameters required to describe a water-saturated rock mass in order to understand leakage to an underground excavation are the distributions of hydraulic conductivity (K), required for transient and steady-state rates, and specific storage (S_s), required for transient rates only.

For shallow excavations, hydraulic parameter distributions can be derived from boreholes drilled from the surface (Raymer 2001). In case of deep and long excavations, the depth precludes the systematic characterization of the rock mass from surface boreholes. During the planning phase, data might be compiled from preceding excavations or drillings from similar settings (Löw et al. 1996). If a particular threat related to water inflow or water pressure is brought to light by the preliminary investigations, pre-drillings (probing ahead of the excavation front) can be used to characterize the rock mass to be excavated.

The Sedrun section of Gotthard Base Tunnel (GBT) is located about 1380 meters below the Nalps hydropower reservoir. The drainage of a massif by a deep tunnel is known to cause settlements even in hard crystalline rocks (Zangerl et al. 2008; Zangerl et al. 2008a). In response to potential surface deformations at the foundation of the Nalps arch dam caused by the drainage of the massif through tunneling, systematic pre-drillings have been carried out in a 5 km long tunnel section. In this case, the main objective of the pre-drillings was to forecast and prevent large inflows to the tunnel, causing critical surface settlements.

This pre-drilling campaign constitutes an extraordinary opportunity to systematically study the rock mass hydraulic properties of a long section in fractured crystalline rocks. In the present paper, the authors use data from the pre-drillings to derive distributions of transmissivity (T) and hydraulic conductivity for 50 m sized blocks (K). A particular effort is made to estimate the uncertainties related to the derived values. The results are discussed and interpreted in terms of the geologic and fracture properties. The K -values are then compared with those obtained from similar studies at regional scale (Masset and Loew 2010). Finally the authors discuss the distribution of hydraulic conductivity in fractured rocks along pre-drillings at 50 m scale. The resulting K -value distribution is used

in a companion paper (chapter 4) to simulate transient tunnel inflows which in turn are compared to observed tunnel inflows.

3.3. Tunnel description and geologic settings

3.3.1. General GBT settings

The GBT is a 57 km long railway tunnel build across the Central Swiss Alps (Figure 1). Its purpose is to facilitate the transit of people and goods across the Alpine chain. The excavation of the tunnel is close to completion (97% excavated on August 1st 2010). The tunnel is composed of two parallel tubes of about 10 meters diameter, separated by a distance of about 40 meters. Parts of the tunnel have been excavated with a tunnel boring machine (TBM) and other parts by drill and blast. The excavation of the GBT started at five different points of attack: Erstfeld, Amsteg, Sedrun, Faido and Bodio (Figure 2). The depth of GBT ranges from 0 to 2400 meters, the elevation from 300 to 530 meters a.s.l. and the general orientation is NNW-SSE (Figure 1). The tectonic units crossed by the tunnel are from North to South, the Aar massif (AM), the Tavetsch "Zwischenmassiv" (TZM), the Urseren-Garvera zone (UGZ), the Gotthard "massif" (GM), the Piora zone and the Penninic gneiss zone (Figure 2). Note that TZM and GM are not true massifs in the sense that they are allochthonous (Pfiffner et al. 1997).

3.3.2. GBT Sedrun section

The section studied in the present paper belongs to the Sedrun lot which starts in the southern part of the TZM, crosses the UGZ and ends in the centre of GM (Figure 3). Along the studied section, located south of the Sedrun point of attack (Figure 2 to Figure 4), the tunnel has been excavated by drill and blast below the Nalps reservoir dam located in the northern GM (Figure 3 and Figure 4). Figure 4 shows a cross-section along the tunnel studied section with geological settings, projection of the Nalps Lake and location of major fault zones. The numbers plotted on the fault zones are identification numbers that were attributed to fault zones mapped from the surface in the context of GBT prognosis. All these fault zones have been recognized in the tunnel except FZ51 and FZ52. There are a couple of supplementary fault zones that were identified in the tunnel only. These do not have identification numbers and are identified with an interrogation mark on Figure 4. The tunnel depth in the studied section ranges

from 897 to 2026 meters (Figure 5) and the surface elevation from 1550 to 2950 meters. The local orientation of the tunnel is N-S, which means that the tunnel axis is about perpendicular to the steeply dipping Alpine foliation and geological boundaries.

3.3.3. Tectonic units

The Tavetsch "Zwischenmassiv" (TZM) is a 35 km long "massif" wedged between the Aar massif (AM) in the North and the Gotthard "massif" (GM) in the South (Ambühl et al. 2008). The contact zone to the AM is strongly tectonized (Guntli 2006). At South, the TZM is in tectonic contact with the sediments of the Urseren-Garvera zone (UGZ) (Figure 2-4). The TZM is mainly composed of metasediments, migmatites, meta-vulcanites, pegmatitic dikes and interlayered talc schists, serpentinites, metadiorites, amphibolites and quartzo-sericitic schists. Quartz veins are abundant in the vicinity of the major shear zones.

The Urseren-Garvera zone (UGZ) separating the TZM from the GM consists of a thin sediment-layer of more than 100 km length along strike (Figure 2-4) (Ambühl et al. 2008) It essentially includes the post-Variscan mono-metamorphic sediment cover of the Gotthard massif. The steeply dipping layers contain metasediments from Permo-Carboniferous to Jurassic ages. The metasediments consist of meta-psammities and meta-pellites, intercalated with quartzite, green schists, meta-rhyolites and conglomerates, and carbonate rich metasediments.

The Gotthard "massif" (GM) is a 115 km long NE-striking crystalline body of the European continental crust (Figure 2-4). It is composed of pre-Variscan polyorogenic and polymetamorphic basement rocks, including gneisses, schists, migmatites and amphibolites, intruded by Variscan granitoids (Labhart 1977). To the North it is in stratigraphic contact with the Permo-Carboniferous sediments of the Urseren-Garvera zone (Wyss 1986). This contact locally also shows a strong tectonic overprint. To the South, the Gotthard massif is in contact with steeply dipping parautochthonous metasediments of the Piora and Nufenen zones consisting of schists, carbonates, and evaporates (Herwegh and Pfiffner 1999). The formation of a penetrative Alpine foliation and of steeply dipping ductile shear zones that mainly strike NE-SW occurred during the Oligocene in a compressive NW-SE directed stress field (Marquer 1990; Steck 1968; Zangerl et al. 2006; Zangerl 2003). Towards the end of the Tertiary collision, the deformation mode gradually evolved from ductile to brittle (Luetzenkirchen and Loew 2010).

3.4. Pre-drillings description

3.4.1. Pre-drilling types

The section of the tunnel analyzed in the present study corresponds to the section with systematic pre-drillings (Figure 4). Along this 5 km long section, 30 cored and 94 destructive boreholes have been drilled ahead of the two tunnel tubes. The boreholes slightly overlap so that the entire length has been covered along both tunnel tubes. Destructive boreholes (in-hole hammer) have length values ranging from 17.5 to 106.7 meters with a mean of 70 meters and a diameter of 64 mm. Cored boreholes (cable drilling) have length values ranging from 47 to 358.5 meters with a mean of 70 meters and a diameter of 96 millimeters.

3.4.2. Borehole inflow logging

While drilling, the drilling crew systematically surveyed the inflow rate and rate measurements have been taken when significant changes in the inflow rate were observed. In the case of cored boreholes, rate data were sometimes acquired during the drilling operations, when the core was taken out, and at the end of drilling under open-hole conditions. The core catcher length, 3 m, determines the precision of the inflow location. When a water conductive structure is cross cut by the borehole, water flows from the structure along the annulus (open space of about 3 mm) in direction of the drillbit, passes through the drill bit and flows back through the drilling rods. In case of destructive boreholes, the inflow rate was sometimes measured during the drilling with the bore rods in the borehole and after drilling completion without the bore rods. By analogy to cored boreholes, water flows along the annulus, passes through the in-hole hammer flush holes and flows back in the drill string. The main difference is the annulus open space width which is much larger for the in-hole hammer (open space of 2 cm). In case of important inflows a decrease of the inflow rate through friction along the annulus (especially in the case of cored drilling) can be expected. However, the comparison of measured rates over the entire boreholes with and without bore rods shows that for the considered low rate range there is no significant decrease of the flow rate through friction along the annulus. The inflow rate was always measured three times with a bucket and a watch and averaged. The rate values range from 0.001 to 7.9 liters per second.

3.4.3. Water temperature and pore-pressure

Water and rock temperatures are plotted on Figure 5 with the depth of the tunnel. Both increase with depth and show similar values. Water temperature allows converting transmissivity or hydraulic conductivity values into transmissibility or permeability values.

The pore pressure has been measured in 26% of the boreholes (Figure 6). The boreholes tested were shut for several minutes up to several hours and the borehole pressure recorded with a gauge until it reached a stable value. The pore-pressure corresponds to the maximum pressure recorded.

The pore-pressure values range from 6 to 140 bars which is equivalent to pressure heads of 61 to 1430 meters (for water at 20°C). The highest value reported comes from a borehole located below the projection of the Nalps reservoir ahead of the more advanced SE-tube (Figure 5). The difference between the elevations of the tunnel and the surface of the Nalps Lake at that location and at the date of the measurement (04.11.2008) amounts to 1375 +/- 5 meters. The highest value can be interpreted in terms of water table elevation above the tunnel under undisturbed pore-pressure conditions, whereas the lowest ones are influenced by the pore-pressure drawdown caused by the tunnel or earlier pre-drillings.

3.5. Quantitative analysis of pre-drilling inflows

3.5.1. Analytical solutions

The Jacob and Lohman solution for the transient rate to a well under constant drawdown (Jacob and Lohman, 1952) is used to estimate the transmissivity of the rock mass surrounding each measurement interval of all pre-drillings:

$$3-1 \quad \frac{\Delta h}{Q(t)} = \frac{2.3}{4\pi T} \log \frac{2.25Tt}{r^2 S}$$

Δh is head drawdown, $Q(t)$ is flow rate in function of the elapsed time t , T is transmissivity, r is radius of the well and S , storativity. In the context of the pre-drillings, Δh is calculated from the measured pore-pressures at the end of drilling, $Q(t)$ is measured, t is interpolated, r is known and S is assumed. The Jacob and Lohman model assumes:

1. An infinite confined aquifer (in the present case of vertical extent)
2. A uniform aquifer thickness, permeability and compressibility
3. No flow boundaries at the bottom and the top of the aquifer (in the present case, no flow lateral boundaries)
4. A uniform initial head is followed by an instantaneous drop of the head in the borehole at time zero
5. Laminar (Darcian) single-phase flow.

Because of the first assumption, the model applicability is limited in time. It is only valid as long as the pore-pressure perturbation propagating from the well does not reach a flow boundary. The time limit (t_{lim}) for the validity of the Jacob and Lohman solution can be expressed by the following equation from Perrochet (2005a):

$$3-2 \quad t_{lim} = \frac{S^2}{\pi T} \left(\frac{L}{r\sqrt{e}} - 1 \right)^2$$

With L, the closest distance to a flow boundary.
Replacing the ratio of T over S by diffusivity, D:

$$3-3 \quad t_{lim} = \frac{r^2}{\pi D} \left(\frac{L}{r\sqrt{e}} - 1 \right)^2$$

The radius of the pore-pressure perturbation extent at a given time can be calculated with the following relation:

$$3-4 \quad r = \sqrt{e} \left(\sqrt{\pi t D} + 1 \right)$$

r is the perturbation radius, the distance from the borehole axis to the rim of the pore-pressure perturbation, t, the elapsed time between the drilling and the measurement and D, the diffusivity. The second group of assumptions implies that the rock mass surrounding each measurement interval constitute a vertical layer of uniform thickness, permeability and compressibility. The third assumption implies that no water exchange takes place between the "layers" defined by the different measurement intervals and that the flow geometry is purely radial. The

fourth assumption implies that the drilling of the preceding measurement intervals uniformly affect the head distribution in the layers defined by the next interval. The last assumption implies for example that no head losses take place due to a local turbulent flow regime or to dual-phase flow (e.g. CO₂ degassing). Most of these assumptions are not fulfilled. The use of the Jacob and Lohman solution in the present context should therefore be considered as a simple approximation. The realism of the different assumptions will be further addressed in the discussion section.

3.5.2. Parameter processing and probability density functions

Because the primary objective of the pre-drilling campaign was to detect locations with large inflows to the tunnel and not to characterize the rock mass hydraulic conductivity/transmissivity, parameters required to calculate transmissivity/hydraulic conductivity have not all been precisely measured. Therefore these parameters needed to be interpolated or assumed. Consequently uncertainties are associated with some parameters and the resulting K/T-values. Therefore a probability distribution function was attributed to each parameter (Table 1). The assumed variability of the parameters is given in standard deviation (SD) or relative standard deviation (RSD); except for the elapsed time (empiric distribution). The uncertainty associated with the resulting K/T-values was derived by Monte Carlo simulation (MCS) for each measurement interval.

Table 3-1 Probability density functions of input parameters

Parameter	Interval Length	Measured Pressure Head	Interpolated Pressure Head	Inflow Rate	Elapsed Time	Borehole Radius	Specific Storage
Unit	L[Tm]	P _m [Pa]	P _i [Pa]	Q[m ³ /s]	t[s]	r[m]	S _s [m ⁻¹]
PDF	Gaussian	Half-Gaussian	Gaussian	Gaussian	Empiric	Half-Gaussian	Log-Gaussian
SD	-	-	-	-	-	-	0.5
RSD [%]	1	5	50	1	-	1	-

Interval length

Figure 7 shows a sketch of a cored borehole. Most boreholes start with a standpipe of 15 m (grey). The borehole is drilled in steps of 3 m (length of the core catcher). The inflow rate was only measured when significant changes in the flow rate occurred. The precise measurement of the inflow rate implies a break in

the drilling operation. Some time between the drilling stop and the measurement is needed to be sure that the water flowing out is groundwater and not drilling water. In general, when a measurement was taken, two values have been reported: the total inflow rate and the increase in the rate over a given interval. This interval can be the distance between two reported measurements or a smaller distance as well. For example on Figure 7 the increase in the inflow rate at point B is the difference between rates B and A. The interval length is the distance between point A and B. At point C, the rate increased of 1 l/s over the last three meters.

There are basically three different options for the interpretation of the rates:

1. If the inflow rate is assumed to be constant, the difference in rate between two consecutive measurements is the contribution of the interval separating the two measurements. This option has an important drawback: a decrease in the inflow rate cannot be explained with constant rates.
2. Assuming a decrease of the inflow rate with time would be a better option however it requires precise information concerning the drilling schedule of the different intervals as well as local hydraulic conductivity and specific storage values.
3. The last option is to consider that the measured rates come from the entire drilled interval at the time of the measurement. This is always true and does not require any assumption. Compared to the first two options, the drawback of this option is that the defined rate intervals are longer and overlapping and the variability of the flow rate smoothed.

The third option was selected by elimination. The first one is not realistic and the second one not applicable in this case.

It was possible to further precise the measurement interval in some cases. For example, if no flow comes out of a starting section of the borehole, its length can be subtracted to the measurement interval. Similarly if no flow comes out during the drilling of a central section, the sum of the lengths of all preceding sections including the central one can be subtracted to the next measurement interval. The interpretation of the destructive boreholes is similar. In total, 312 intervals have been defined. Their lengths range from 0.1 to 309.5 meters. The assumed PDF for the interval length is normal and has an assumed RSD of 1%.

Radius of the borehole

In principle the radius of a borehole has a constant value. However a half-normal distribution was taken with a RSD of 1% to test the effect of variation of the radius due to breakouts.

Pressure head

The uncertainty associated with the drawdown term (Δh) is function of the pore-pressure reading precision and the duration of the measurement. In addition, pore-pressure values are missing for 74% of the measured intervals and in that case the closest value from nearby intervals was taken. Consequently, when no pore-pressure measurement is available, the uncertainty associated with the pore-pressure value is much higher. When measured, the pore pressure has an assumed relative standard deviation (RSD) equal to 5% of the pore pressure value. When "interpolated" the assumed RSD amounts to 50% of the pore pressure value which equals to the RSD of all pore-pressure measurements (Figure 6).

Inflow rate

The uncertainty related to the inflow rate ($Q(t)$) is only function of the measurement method. The inflow rate was measured three times with a bucket and a watch and the inflow rate taken as the mean of the three measurements. The rate RSD is assumed to be equal to 1% of the rate value.

Elapsed time

In theory the elapsed time is the time elapsed between the drilling at one location and the rate measurement at that location. This means that the elapsed time vary within a measurement interval. In practice, the elapsed time is defined as the time elapsed between a mean drilling time and the measuring time of the measurement interval. As the starting and ending drilling times of specific borehole intervals have not been recorded, these are interpolated.

The derivation of the mean elapsed time and its associated uncertainty is done in three steps: the calculation of the total drilling duration, the derivation of the drilling mean speed and the calculation of the elapsed time.

1. The total drilling duration equals to the difference between the drilling end time and the drilling start time plus or minus one time unit (Figure 8). The

time unit used is function of the precision of the reported times (day, hour or minute).

2. The drilling mean speed equals to the ratio between the total length of the drilling and the drilling duration. A Gaussian distribution with a RSD of 1% is assumed for the total length of the drilling.
3. The mean elapsed time equals to the ratio between the interval length and the drilling mean speed divided by two plus one hour to account for the time between the drilling stop and the measurement. The interval length has an assumed Gaussian distribution with a RSD of 1%. The resulting PDF of the mean elapsed time is derived through Monte Carlo simulation.

Note that the uncertainty calculated for the elapsed time only accounts for the input parameter uncertainties. The uncertainty related to the method of derivation is not included and will be addressed in the discussion section.

Specific storage

Table 2 shows some typical specific storage values reported from massive limestones and crystalline rocks of the Alps. The specific storage values range from 2×10^{-7} to 10^{-5} m^{-1} . A mean value of 10^{-6} m^{-1} has been selected in the present study. The PDF of the specific storage is assumed to be log-normal. The base-ten logarithm of the specific storage has an assumed SD of 0.5 m^{-1} . This means that 95% of the values range over two orders of magnitude ($1 \cdot 10^{-7} - 1 \cdot 10^{-5} \text{ m}^{-1}$).

Table 3-1 storage values in hard fractured rocks of the Alps (FZ: fault zone)

Rock type	Location	Value/range [m^{-1}]	Reference
Fractured limestone	Loetschberg	$4-9 \times 10^{-7}$	(Pesendorfer and Loew, 2010)
FZ in granite	Mt Blanc	1.8×10^{-5}	(Maréchal and Perrochet, 2003)
FZ in granodiorite	Grimsel	10^{-5}	(Hoehn, et al., 1990)
Gneiss	Adula	10^{-6}	(Nagra, 1988)

Radius of the pore-pressure perturbation

The radius of the pore-pressure perturbation is calculated for each interval measurement and compared with the minimum distance to the water table, assumed to be located about a 100-meter below ground surface. If the radius of the perturbation overpasses the minimum distance to the water table, the infinite-aquifer assumption of the Jacob and Lohman model is not satisfied anymore. In

such a case, the Goodman et al. (1965) equation would be used, assuming a constant head upper boundary above the tunnel:

$$3-5 \quad Q = \frac{2\pi T \Delta h}{2.3 \log(2\Delta h / r)}$$

Q is constant rate, T is transmissivity, Δh is drawdown and r is the radius.

3.6. Results

Uncertainties

There are two types of uncertainty. The first type relates to inadequacies between some of the Jacob and Lohman model assumptions and the system. Uncertainties of this type can hardly be quantified and will be addressed in the discussion section. The second type of uncertainty relates to the model parameters uncertainty. As example, Figure 9 shows histograms of the distribution of the main parameters (elapsed time, borehole radius, inflow rate, interval length, hydraulic head and specific storage) for one interval and the resulting transmissivity, diffusivity, hydraulic conductivity and pressure perturbation radius distributions derived by Monte Carlo simulation.

Contribution to variance

Figure 10 shows pie charts of the contribution in percent of the different parameters to the variance of the transmissivity. The contribution to the variance takes into account both the uncertainty and the sensitivity of the parameter. The T-uncertainty mainly relates to the specific storage and pore pressure uncertainties. Uncertainties related to the inflow rate and the interval length, have a lower impact. Finally uncertainties related to both elapsed time and borehole radius are negligible.

Validity of the Jacob and Lohman "infinite aquifer" assumption

It has been checked that the theoretic distance reached by the pore-pressure perturbation at the time of the measurement (equation 4) was smaller than the assumed closest flow boundary Figure 9. In the present study, the pore pressure perturbation radiuses of all intervals remain smaller than the theoretic minimum distance to the closest flow boundary. Consequently, the Jacob and Lohman solution was applied overall.

T-distribution along the studied section

The distribution of the transmissivity along the studied section is shown in Figure 11. The first plot on the top shows the distribution of T along the eastern tube and the second plot, the T-distribution along the western tube. The plotted rectangles represent the length of the measurement interval along the x-axis and the probable range of T-values calculated with the MCS along the y-axis. The probable range corresponds to four times the calculated standard deviation. This means that 95% of the ten-base logarithms of T-values are included in this range provided that the underlying distribution of the logarithmic values is normal. The colored rectangles represent the intervals with a measured pore-pressure value and the empty rectangles, the interval without measured pore-pressure measurement. The gaps along the x-axis result from the water-non-productive intervals. The dashed vertical lines indicate the location of the major contacts (right: TZM/UGZ, left: UGZ/GM). The pink vertical line indicates the location of the "Rötiserie", a dolomitic layer intercalated in the sediments of the UGZ. Finally, the vertical grey lines indicate the location of the major fault zones. Fault zone numbers correspond to the numbers plotted on the cross-section (Figure 4). The blue numbers will be discussed further when describing the hydraulic conductivity distribution.

Derivation of the K-distribution along the studied section

The K-distribution is derived in three steps. In a first step, hydraulic conductivity values are derived, dividing the transmissivity by the interval length (Figure 12). In a second step, higher and lower bounds hydraulic conductivity values are defined along the two tunnel tubes (Figure 12). The last step consist in averaging (geometric average) the higher and lower bound hydraulic conductivity values over tunnel intervals of 50 m (Figure 13).

Distribution of the K-values along the studied section

The distribution of the hydraulic conductivity along the studied section is shown in Figure 14. The first plot on the top shows the distribution of K along the eastern tube and the second plot, the distribution of K along the western tube. The light color bars represent the lower-bound K-distribution and the dark color bars, the higher-bound K-distribution. The vertical lines indicate the location of major geologic structures as described in section 5.4.

Interpretation of the high-K-values

Figure 14 shows the distribution of the hydraulic conductivity along the studied section for the East (top plot) and the West tubes (bottom plot). K-values are represented with bars of 50 m width. The light color bars represent the lower bound K-values and the dark color bars, the higher bound K-values. The dashed vertical lines indicate the location of the major contacts (right: TZM/UGZ, left: UGZ/GM). The pink vertical line indicates the location of the "Rötiserie", a dolomitic layer intercalated in the sediments of the UGZ. Finally, the vertical grey lines indicate the location of the major fault zones.

In the following, some of the intervals/sections showing the highest K-values are briefly described from the lithologic and structural point of view. The numbers correspond to the blue numbers plotted on Figure 11.

1. The first section consists of pegmatitic gneiss and pegmatite interlayered with biotitic-muscovitic gneiss (significant stiffness contrast). Some thin layers of kakirite are present a few meters south of the interval (Tm 2193 – Tm 2195). The presence of faults/shear zones of small width (<0.5 m) increases towards the south.
2. The second interval consists of muscovitic-biotitic gneiss intercalated with more schistous and intensively fractured rocks with few graphitic shear zones (<2 cm). A 1.2 m-width fault zone (FZ41) with fault gauge and cataclastic rocks (Tm 2462 – Tm 2468) is present to the south of the interval.
3. The third section consists of biotitic muscovitic gneiss with a more or less developed schistosity. The section ends with a 1-m-thick schistous phyllitic shear zone.
4. The fourth interval is made of an alternation of quartz rich leucocratic biotitic gneiss exhibiting brittle deformation with little fractured grey biotitic gneiss (stiffness contrast). Open fractures (<3 mm), graphitic shear surfaces and sandy kakirite (1-m-thick) have been encountered as well.
5. This fifth section is made of biotitic gneiss. An interval of six meters present several open fractures. Hydro-tests conducted on longer intervals including the present section yield transmissivity values ranging from 8.8×10^{-7} m²/s (test length: 189 m) to 4.2×10^{-6} m²/s (test length: 275 m).
6. This sixth interval is centered on fault FZ 49, exhibiting thin layers of fault gauge and cataclastic rocks. An increased frequency of fractures is

observed over tens of meter on both sides of the relatively small fault zone (3.6 m). Hydro-tests conducted over a 137-m-long section enclosing the 50-m-interval yield transmissivity values ranging from 8×10^{-7} m²/s to 9.0×10^{-6} m²/s.

7. The seventh section is found to the South of a wide fault zone (FZ50b) ranging over 130 m exhibiting several fault cores. It consists of intensely fractured gneisses exhibiting tens of thin kakiritic layers.
8. This eighth interval is made of chloritic biotitic gneiss and schistous gneiss intensively fractured. The interval ends with a 1-m-thick kakiritic section.
9. The ninth interval is made out of chloritic biotitic gneiss partly overprinted by schistosity with some lenses of calcsilicate rich rock (serpentinites).
10. The tenth section includes biotitic gneiss intercalated with a lower proportion of schistous gneiss.
11. The eleventh interval consists of biotitic muscovitic gneiss including a 0.5 m thick lamprophyre dike.
12. The twelfth section is found to the south of a fault core of 15 m width (FZ41) alternating sandy and clayey kakirite. The section is made of an alternation of gneiss and pegmatite overprinted by schistosity.
13. The thirteenth interval consists of an alternation of pegmatite/pegmatitic gneiss and biotitic gneiss (stiffness contrast). Contact between the pegmatite and the biotitic gneiss exhibit a higher fracture density.
14. The fourteenth section is made of biotitic muscovitic gneiss alternated with pegmatite/migmatitic gneiss. At the end of the interval a fracture zone (zone with high fracture frequency) is encountered.
15. The fifteenth interval consists of gneiss cut by a 5-cm-thick layer of kakiritic gneiss.
16. The sixteenth section locates to the south of 47-m-wide fault zone (FZ44). The rock consists of intensively fractured biotitic scericitic gneiss containing several cm-thick layers of kakirite.
17. The seventeenth interval is the equivalent of interval number 4 and presents the same characteristics.
18. The eighteenth section ends at the rim of FZ49. An increased density of fractures and shear surfaces is observed in direction of the fault zone in the biotitic gneiss.

19. The nineteenth section starts on the other side of fault zone number 49. It consists of biotitic muscovitic gneisses. The interval does not show an increased fracture frequency.
20. The twentieth interval follows FZ50, a narrow fault zone of 8-m-width. The interval consists of biotitic gneiss exhibiting lamprophyric dikes and dm to cm-thick zones containing several open fractures (<1 mm).
21. The twenty-first section is found at the northern rim of FZ50b. It consists of gneiss and schistous gneiss exhibiting an increased brittle overprint in direction of the fault zone.
22. The twenty-second section is the equivalent of section 8 and presents the same characteristics.

3.6.1. Conductivity of the main fault zones

Fault zones (FZs) considered here are the one that were previously identified from the surface and that have been encountered by the boreholes first and by the tunnel later. It is assumed that these FZs are continuous structures ranging over large distances. At surface these FZs constitute lineaments ranging over kilometric distances.

From a general point of view, Table 3 shows that the mean hydraulic conductivity (geometric mean) inside or in the vicinity of fault zones is only slightly higher than the overall mean hydraulic conductivity (geometric mean).

Table 3-2 Mean K-value inside fault zones versus overall mean K-value

	Overall	FZ location	FZ location +/- 25 m	FZ location +/- 50 m	FZ location +/- 75 m
Mean $K_{\text{higher-bound}}$ [m/s]	5.97×10^{-9}	7.91×10^{-9}	6.98×10^{-9}	6.33×10^{-9}	5.14×10^{-9}
Mean $K_{\text{lower-bound}}$ [m/s]	2.39×10^{-9}	2.47×10^{-9}	2.31×10^{-9}	2.18×10^{-9}	1.90×10^{-9}

Considering fault zones individually, some fault zones show K-values above the mean ($K=5.97 \times 10^{-9}$ m/s) in both tubes (FZ42, FZ43, FZ48, FZ49, FZ50, FZ50b, FZ?1), some others show K-values above the mean in one tube only (FZ44, FZ45, FZ46b, FZ?2, FZ?3, FZ53) and the rest show values below the mean along both tubes (FZ40, FZ41, FZ47, FZ?4).

3.6.2. Correlation along a singular tube and between the two tubes

Figure 15 shows four semi-variograms; two for the higher and lower bound K-values along the west tube (SW) and two others for the east tube (SE). The sill is assumed to be equal to the sample variance. Higher bound K-values (HB) present higher nugget values, higher sills and similar ranges as lower bound K-values (LB). The SW-tube exhibits higher sill and longer range values. The correlation length of the K-values is about 800 m in the N-S direction. The correlation between the K-values of the two tunnel tubes is quantified with the correlation coefficient (Table 4). It is assumed that the structures controlling the hydraulic conductivity extend perpendicularly to the tunnel axis. This assumption is verified for the main schistosity and the orientation of the main FZs but isolated faults and fractures vary in their orientation.

Table 3-3 Correlation coefficients between the K-values of the two tunnel tubes

	R-value	P-value
K _{lower-bound}	0.47	6.7x10 ⁻⁷
K _{higher-bound}	0.41	2.0x10 ⁻⁵

Although the two tunnel tubes are only separated by 40 meters, the correlation between the K-values of both tubes is low.

3.6.3. K-distribution

Figure 16 shows the distribution of K for both lower and higher bound K-values. According to a Kolmogorov-Smirnov test both higher and lower-bound K distributions are log-normal. The higher bound K-distribution ranges from 10⁻¹⁰ to 10⁻⁶ m/s and has a geometric mean of 5.97x10⁻⁹ m/s. The lower bound K-distribution ranges from 10⁻¹⁰ to 10⁻⁷ m/s and has a geometric mean of 2.39x10⁻⁹ m/s.

3.7. Discussion

3.7.1. Limitations related to the applied flow model

The Jacob and Lohman model relies on strong assumptions that are not always realized in reality. The "infinite aquifer" assumption is valid as long as the pore-pressure perturbation does not reach an external flow boundary. This does

not take into account possibly existing internal flow boundaries like a thick fault core for example or a zone of higher conductivity.

The “uniform aquifer thickness, permeability and compressibility” assumption is problematic as well. First, observations in the tunnel demonstrate that the thickness of structures, like FZ cores for example, varies from one tube to the other as well as within one tube itself. Second, properties like hydraulic conductivity and compressibility (specific storage) are everything but constant for a given measurement interval. In general the inflow rate assigned to an interval is controlled by few discrete structures like faults or joints whereas the rest of the interval is of much lower conductivity. Similarly the compressibility of fractures is much higher than the compressibility of the intact rock. The “no flow boundary” assumption implies that no water exchange takes place between the layers defined by the different intervals. There are no arguments to say that water-exchange does not take place in reality. However, as long as the derived K-values are treated as local equivalent continuum values, the errors induced by the model simplifications should not be larger than half an order of magnitude (Pesendorfer and Loew, 2010). The “uniform initial head” and the “instantaneous drop of the head” assumptions do not take into account the transient advance of the boreholes and the progressive propagation of the pore-pressure perturbation. Finally, considering the “Darcian single-phase-flow” assumption, flow might be locally and temporarily turbulent due to the presence of strong pressure gradients and CO₂ degassing can occur.

From the pre-drilling data alone, it is not possible to quantify the errors induced by such discrepancies between the model and reality, and the K-uncertainty derived by MCS does not consider them either. These discrepancies must be kept in mind as a potential source of error.

3.7.2. Limitations related to uncertain input parameters

The results of the analysis of the contribution to the K-variance of the different parameters show that the K-uncertainty mainly relates to the ill-constrained specific storage and the uncertainties on the pore-pressure values. This does not mean that the uncertainty related to other parameters can always be neglected. For example, the elapsed time is not a sensitive parameter in the present study because the time values are relatively important. The sensitivity of the time parameter decreases as the time increases similarly to the slope of the inflow rate versus time curve. The uncertainty calculated for the elapsed time

does not take into account the potential error induced by the underlying assumptions of the derivation method, such as constant drilling speed and constant hydraulic conductivity values along the interval.

The contribution to the variance of the diverse parameters is valuable information. It suggests on which parameter to focus in order to reduce the K-uncertainty. For example, in the present study, the precision of the derived K-values would be higher if the pore-pressure measurements had been more systematic and if the specific storage had been derived, for example with interference test between boreholes.

3.7.3. Conductive structures

The conductive structures include fractures such as faults and joints (discontinuities without evidence of shearing). Only a small proportion of fractures effectively conduct water to the pre-drillings. Most intact rocks and the fault cores clay rich gouge or breccias have a much lower conductivity which is below the detection limit (rate is too small to be measured).

In the frame of this study it was not possible to differentiate between conductive types of fault and joint and not conductive ones. The type of fracture however cannot control conductivity alone. The fracture connectivity is as well an important factor.

The location of conductive fractures also varies. These are sometimes located at the rim of fault zones. It is difficult to say whether a fracture is part of the damage zone of a fault zone on the basis of the drilling information. However when spatially related to fault zones, these were mostly associated with fault zones exhibiting a small core and not overprinting an older ductile shear zone. Conductive fractures are also often associated with lithologic boundaries constituting a significant stiffness contrast. This also includes the major tectonic contacts, the alternation of gneiss and schistous gneiss and the presence of pegmatitic or lamprophyric dikes. In the rest of the cases conductive fractures are isolated features (from the pre-drilling point of view).

Heterogeneous hydraulic properties exist within faults and fractures. The presence or absence of infilling, the fault width and the joint aperture are parameters that vary within a single structure. Moreover singular faults and joints are finite structures at the massif scale. At larger scale the heterogeneity results from the distribution and the connectivity of fractures.

Consequently, assuming that fault zones conduct the majority of flow to the tunnel is wrong for the studied section. This is in agreement with observations made along the Amsteg section of the tunnel by the site geologists, where fault zones yielded less water inflow than expected. Note that no particularly strong inflow rates have been reported from the pre-drillings of this test section, whereas strong inflow rates exist in other underground excavations of the Aar and Gotthard massifs (Masset and Loew, 2010).

3.7.4. General K-distribution

The general K-distribution is incomplete towards the lower hydraulic conductivity values due to the limit of inflow detection. The lower values might anyway approach the values measured in the field in intact rock. The spatial distribution is well known in one direction only (N-S, tunnel direction). Some further information is obtained about the distribution of K in the E-W direction by comparing data from the two tubes and finally no direct information is available for the distribution of the hydraulic conductivity in the vertical direction. The absence of correlation between the FZs location and high-K intervals is consistent with the low correlation between K-values of the two tubes.

3.7.5. Representativeness of the studied section

The geometric means of the higher-bound (6.3×10^{-9} m/s) and lower-bound K-values (2.5×10^{-9} m/s) are slightly lower than the K-values derived from inflows to tunnel and galleries located in the GM at similar depths (10^{-8} m/s) (Masset and Loew, 2010). Note that in Masset and Loew (2010) K-values have been derived for 100-meter-long intervals. The highest rate reported from the studied section is relatively small (13 l/s). Higher rates have been encountered in other sections of GBT and in other tunnels of the GM as well (Masset and Loew, 2010). The variability of the K-values is firmly bounded to the interval size. Longer intervals would exhibit a lower variance. When the interval length tends to the length of the entire section, the variance tends to zero. Figure 3-17 illustrates this phenomenon. The K-values envelope of the East tube are plotted together with moving geometric means of the K-values for three different window sizes of 50, 200 and 1000 m length.

3.8. Conclusion

In this paper, a new methodology to quantitatively analyze inflow and pressure data from pre-drillings (drillings made ahead of an underground excavation) was presented. The method based on the Jacob and Lohman solution for transient rate to a well under constant drawdown allows for the derivation of transmissivity (T) and hydraulic conductivity (K) values as well as their associated uncertainties through Monte Carlo simulation. The T-/K-uncertainties only take into account uncertainties related to the input parameters of the Jacob and Lohman solution. Misfits between the conceptual model and reality are not accounted.

This methodology was applied along a 5 km long section of GBT covered by a systematic pre-drilling campaign conducted ahead of the two tunnel tubes. The result is the hydraulic conductivity distribution along each tube per 50 meters interval. Higher- and a lower-bound hydraulic conductivity distributions were derived, taking into account the uncertainty related to the input parameters. The lower-bound K-distribution ranges from 10^{-10} to 10^{-7} m/s with a mean of 2.39×10^{-9} m/s and the higher bound K-distribution ranges from 10^{-10} to 10^{-6} m/s with a mean of 5.97×10^{-9} m/s.

The analysis of the contribution to the variance of T or K from the different parameters shown that the uncertainty in T or K mainly relates to uncertainties associated with the specific storage and the pore-pressure values.

The analysis of the distribution of K along each tunnel tube shown that the hydraulic conductivity at the location of fault zones and in the vicinity of fault zones is only slightly higher than the overall hydraulic conductivity and that the correlation between the K-values of the two tubes is weak. These results do not agree with the common assumption that the large majority of the flow to the tunnel is fed by few major faults.

3.9. Acknowledgements

The authors acknowledge the support from AlpTransit Gotthard AG (H. Ehrbar).

3.10. References

- Ambühl E, Huber HM, Niggli E, Huber W, Niggli M, Flück W, Lützenkirchen V (2008) Geologischer Atlas der Schweiz, Nr. 126, Blatt 1232 Oberalppass - Karte und Erläuterungen.
- Goodman RE, Moya DG, Schalkwyk AV, Javandel I (1965) Ground water inflows during tunnel driving. Bull Assoc Eng Geol 2: 39-56
- Guntli P (2006) Vortrieb Gotthard-Basistunnel, Teilabschnitt Sedrun: geologisch-geotechnisch-hydrogeologische Verhältnisse im Tavetscher Zwischenmassiv und in Urseren-Garvera-Zone. In: Löw S, Wyss R (eds) Geologie und Geotechnik der Basistunnels am Gotthard und am Lötschberg:129-137.
- Herwegh M, Pfiffner OA (1999) Die Gesteine der Piora-Zone (Gotthard-Basistunnel). In: Loew S, Wyss R (eds) Vorerkundung und Prognose der Basistunnel am Gotthard und am Lötschberg:77-88.
- Hoehn E, Fierz T, Thorne P (1990) Hydrogeological characterisation of the migration experimental area at the Grimsel test site Nagra Technical Report.
- Jacob CE, Lohman SW (1952) Nonsteady flow to a well of constant drawdown in an extensive aquifer. Trans Amer Geophys Union 33
- Labhart TP (1977) Aarmassiv und Gotthardmassiv Gebrüder Borntraeger, Berlin-Stuttgart
- Löw S, Ehrminger B, Klemenz W, Gilby D (1996) Abschätzung von Bergwasserzuflüssen und Oberflächenauswirkungen am Beispiel des Gotthard-Basistunnel. In: Oddson B (ed) Instabile Hänge und andere risikorelevante natürliche Prozesse.
- Lützenkirchen V, Loew S (2011) Late Alpine brittle faulting in the Rotondo granite (Switzerland): deformation mechanisms and fault evolution. Swiss Journal of Geosciences 104: 31-54 DOI 10.1007/s00015-010-0050-0
- Maréchal J-C, Perrochet P (2003) Nouvelle solution analytique pour l'étude de l'interaction hydraulique entre les tunnels alpins et les eaux souterraines. Bull Soc géol Fr
- Marquer PD (1990) Structures et déformation alpine dans les granites hercyniens du massif du Gotthard (Alpes centrales suisses). Eclogae geol Helv 83: 77-97
- Masset O, Loew S (2010) Hydraulic conductivity distribution in crystalline rocks, derived from inflows to tunnels and galleries in the Central Alps, Switzerland. Hydrogeology Journal 18: 863-891 DOI 10.1007/s10040-009-0569-1

- Nagra (1988) Berichterstattung über die untersuchungen der phase I am potentiellen standort Piz Pian Grand (Gemeinden Mesocco und Rossa, GR).
- Perrochet P (2005a) A simple solution to tunnel or well discharge under constant drawdown. *Hydrogeology Journal* 13: 886-888
- Pesendorfer M, Loew S (2010) Subsurface exploration and transient pressure testing from a deep tunnel in fractured and karstified limestones (Lötschberg Base Tunnel, Switzerland). *International journal of rock mechanics and mining sciences* 47: 121-137 DOI DOI: 10.1016/j.ijrmms.2009.09.013
- Pfiffner OA, Sahli S, Stäubli M (1997) Structure and evolution of the external basement massifs (Aar, Aiguilles Rouges /Mt. Blanc). In: Pfiffner OA, Lehner P, Heitzmann P, Mueller S, Steck A (eds) *Deep structure of the Swiss Alps Results of NFP 20*:139-153.
- Raymer J (2001) Groundwater Inflow into Hard-Rock Tunnels. *Tunnels and Tunneling International*: 50-53
- Steck A (1968) Junge Bruchsysteme in den Zentralalpen. *Eclogae geol Helv* 61: 387-393
- Wyss R (1986) Die Urseren Zone-Lithostratigraphie und Tektonik. *Eclogae geol Helv* 79: 731-767
- Zangerl C, Eberhardt E, Evans KF, Loew S (2008) Consolidation settlements above deep tunnels in fractured crystalline rock:Part2 - Numerical analysis of the Gotthard highway tunnel case study. *Int J Rock Mech Min Sci* 45: 1211–1225
- Zangerl C, Evans KF, Eberhardt E, Loew S (2008a) Consolidation settlements above deep tunnels in fractured crystalline rock: Part 1 - Investigations above the Gotthard highway tunnel. *Int J Rock Mech Min Sci* 45: 1195–1210
- Zangerl C, Loew S, Eberhardt E (2006) Structure, geometry and formation of brittle discontinuities in anisotropic crystalline rocks of the Central Gotthard Massif, Switzerland *Eclogae geol Helv* 99: 271-290
- Zangerl CJ (2003) Analysis of Surface Subsidence in Crystalline Rocks above the Gotthard Highway Tunnel, Switzerland. PhD Thesis, ETHZ

3.11. Figures

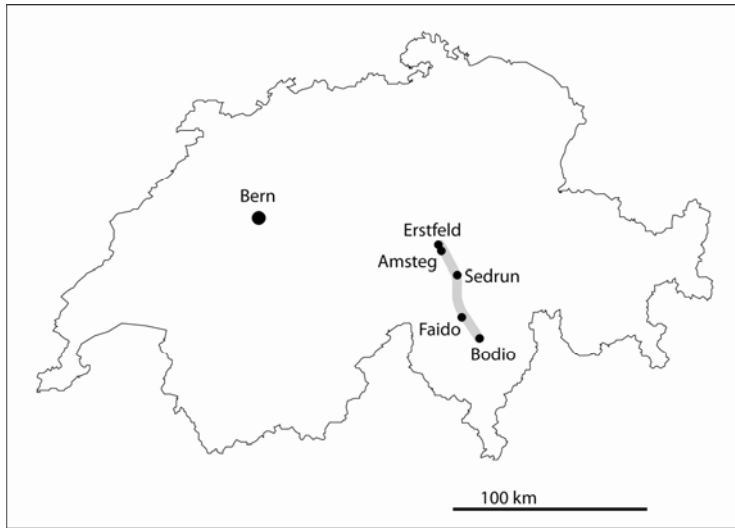


Figure 3-1 Location of Gotthard Base Tunnel (thick grey line)

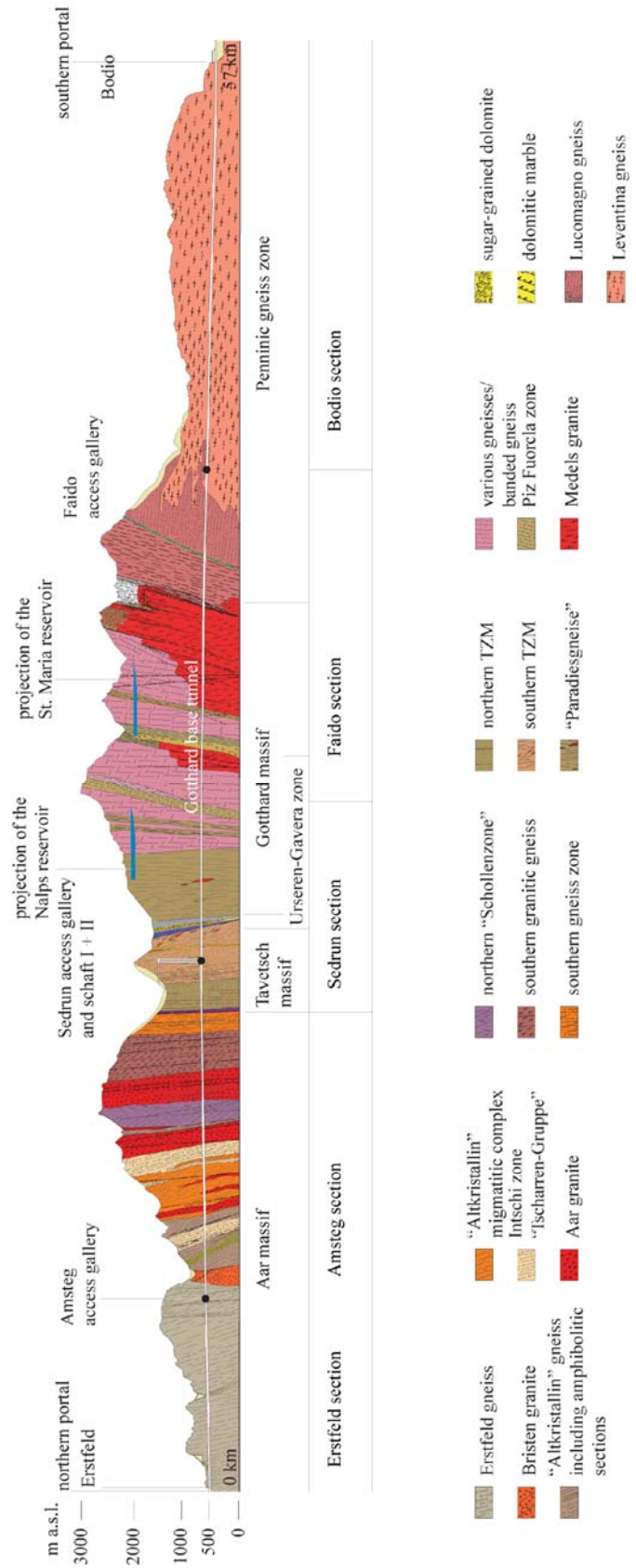


Figure 3-2 Geological cross-section along Gotthard Base Tunnel starting in Erstfeld and ending in Bodio

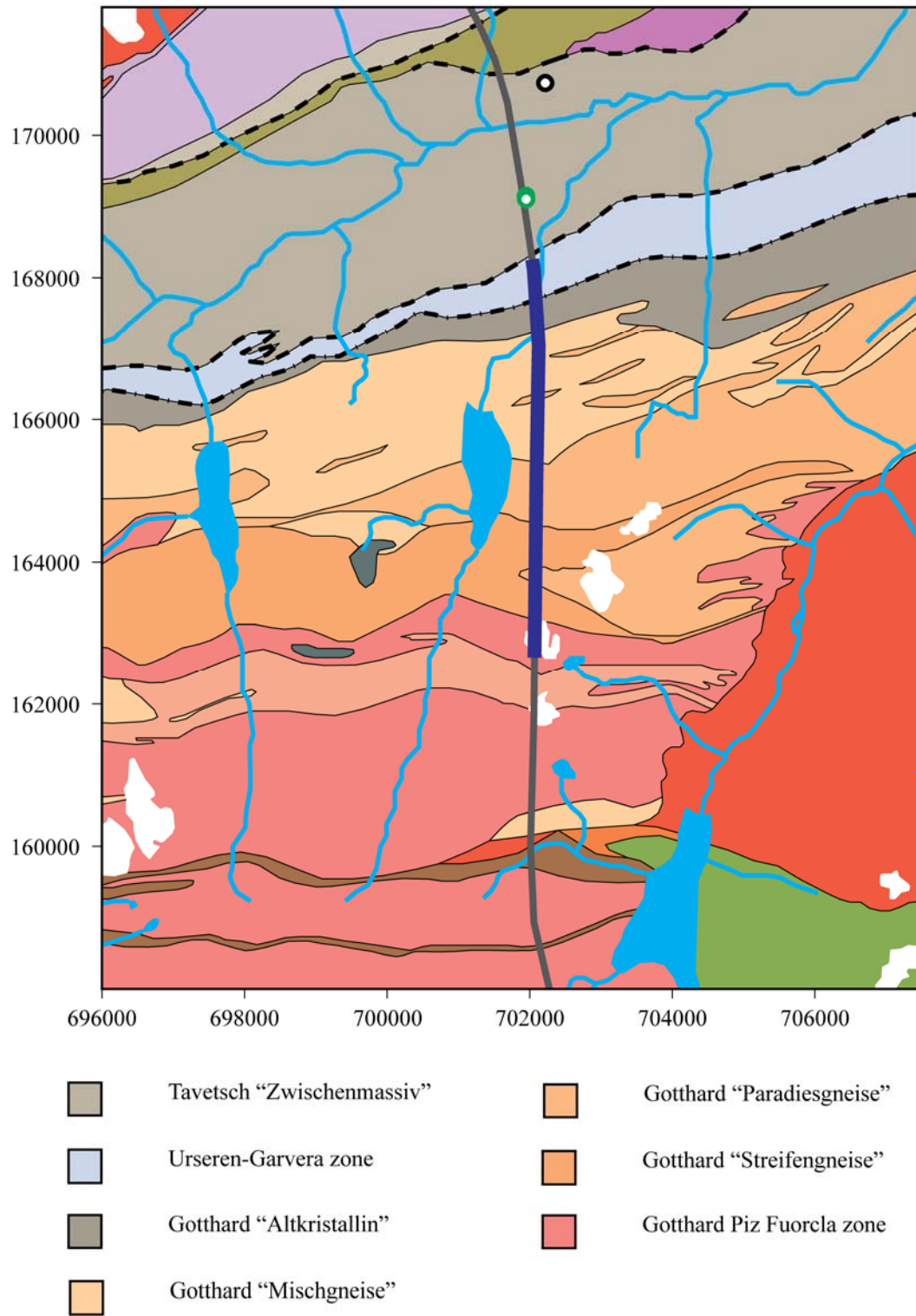


Figure 3-3 Location of the studied tunnel section (thick blue line), Sedrun (black circle) and Sedrun shaft (green circle)

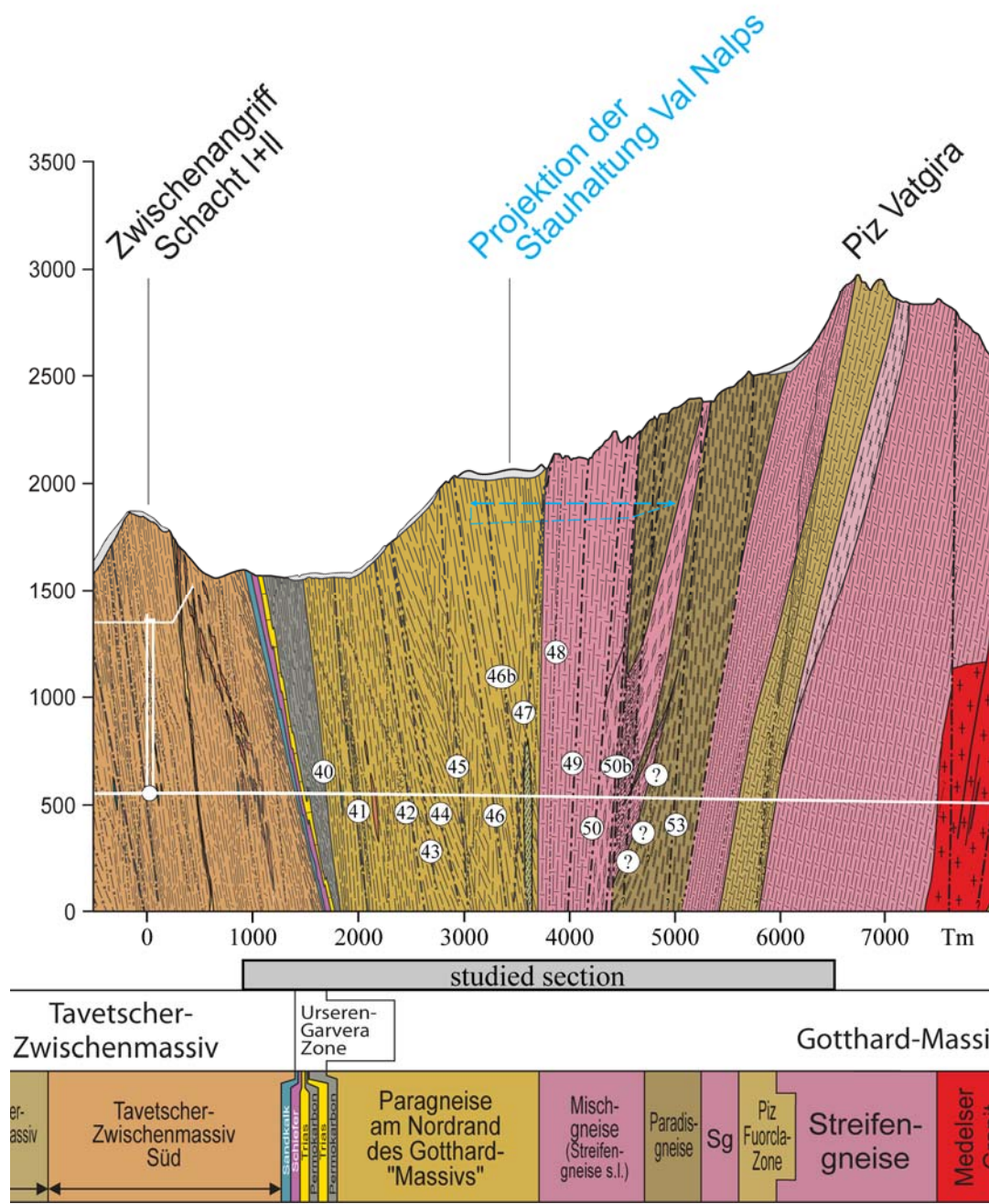


Figure 3-4 Geological cross-section along the studied tunnel section with main fault zones

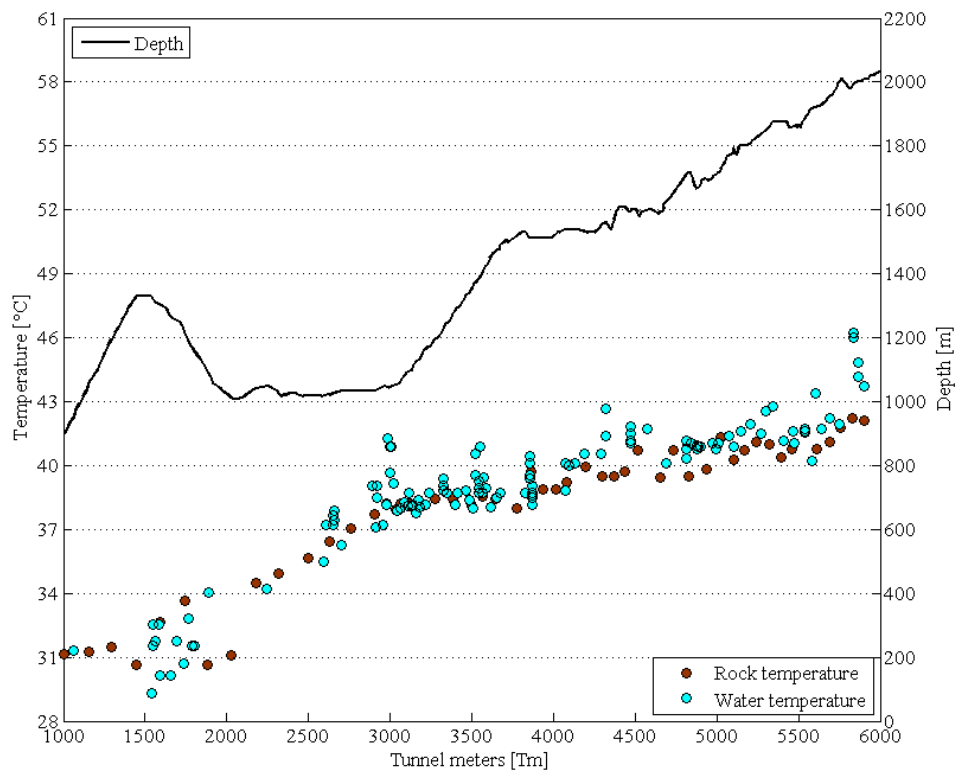


Figure 3-5 Depth, water temperature and rock temperature along the studied section

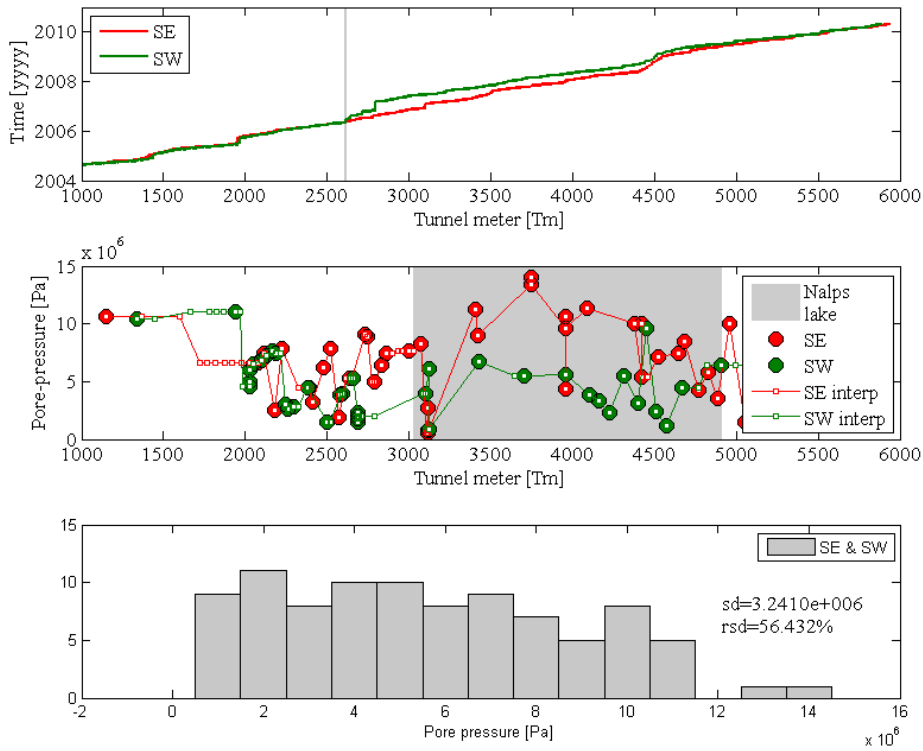


Figure 3-6 Tunnel advance, measured and interpolated pore-pressure values and measured pore-pressure distribution

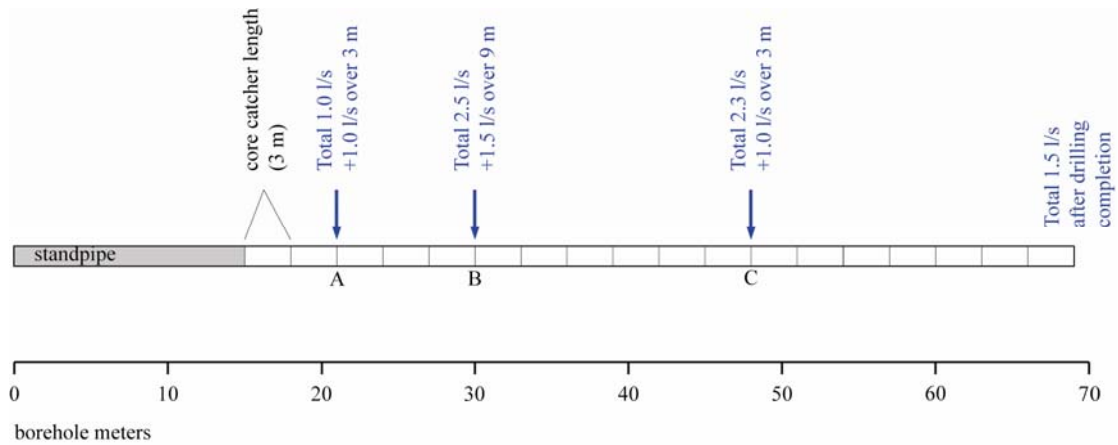


Figure 3-7 Sketch of a cored borehole

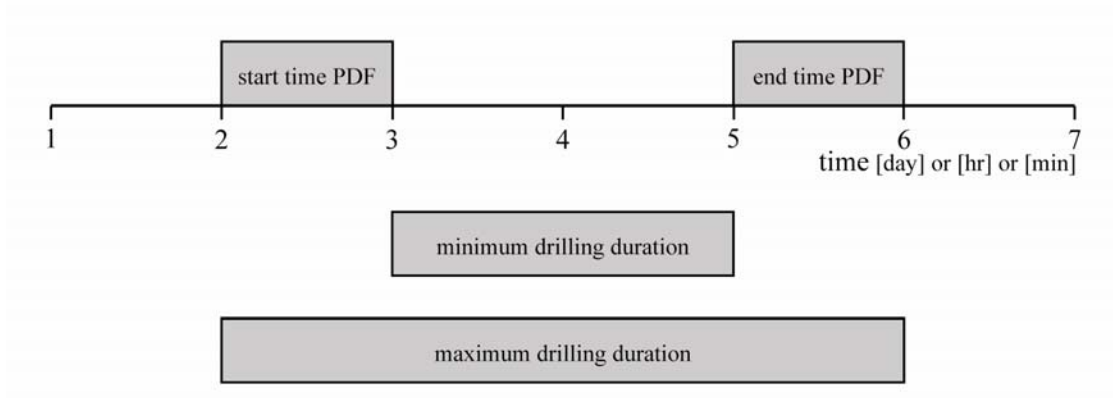


Figure 3-8 Total drilling duration

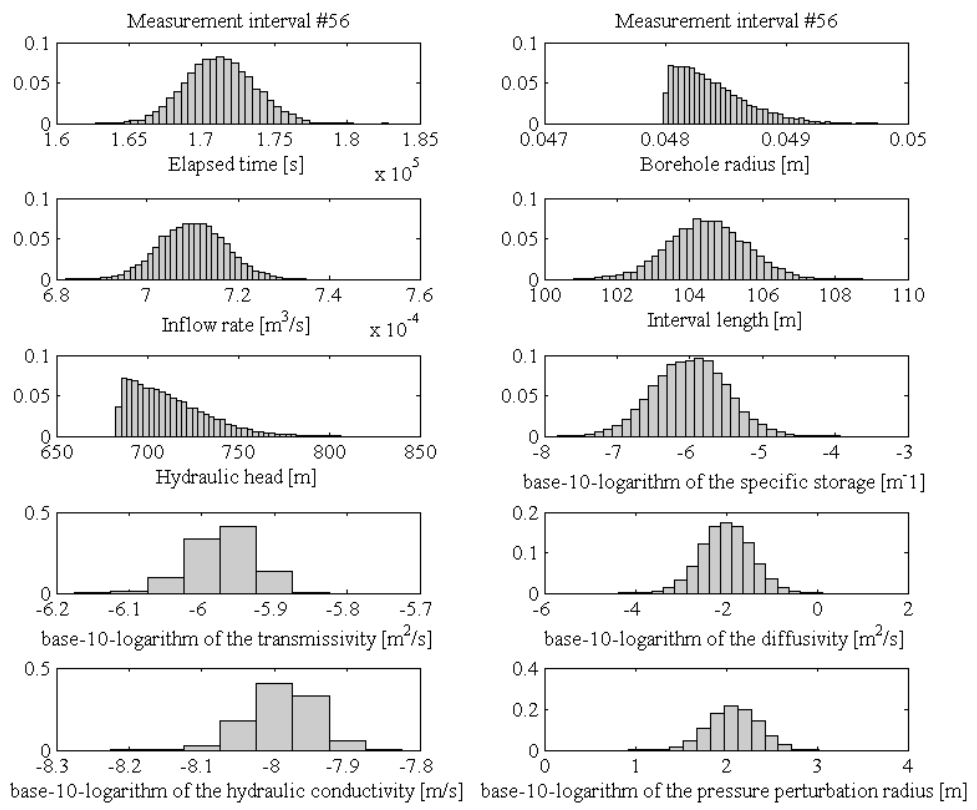


Figure 3-9 Example of parameter distributions generated by Monte Carlo simulation for interval #56

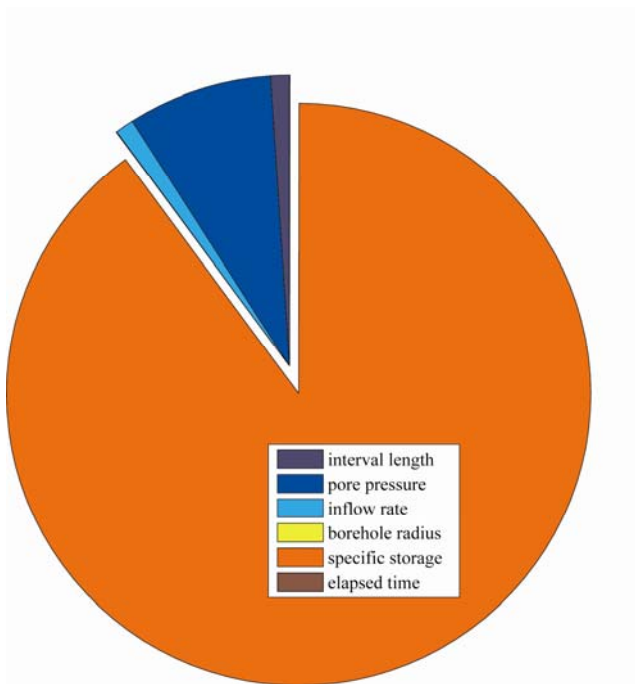


Figure 3-10 Contribution to the variance of the transmissivity from diverse parameters

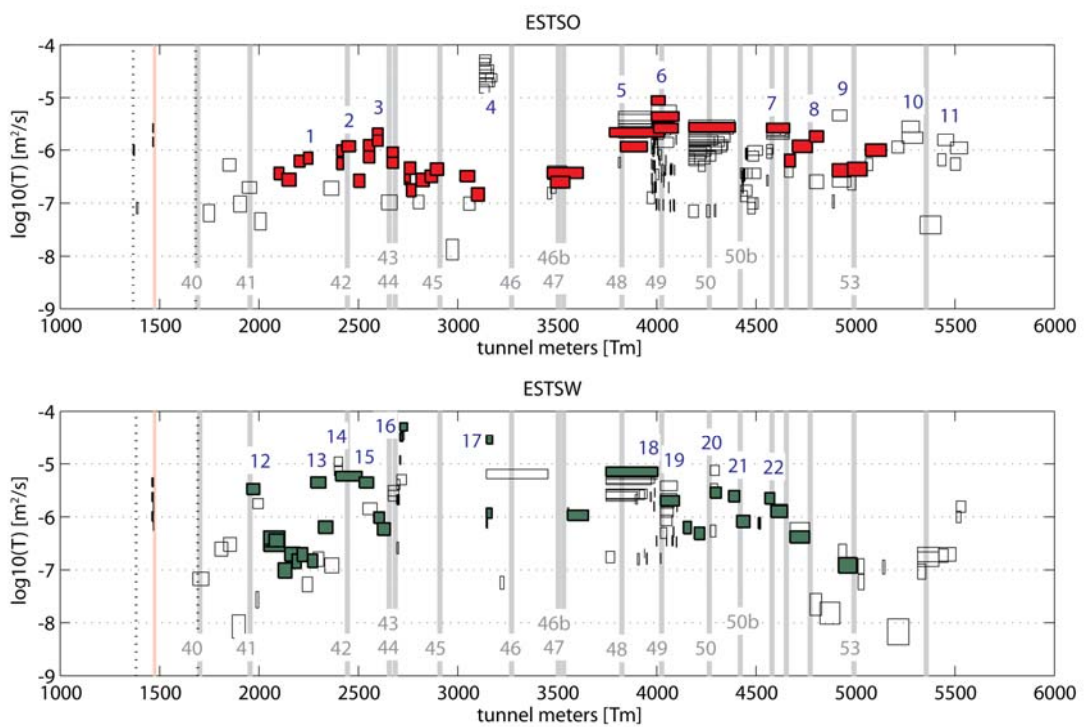


Figure 3-11 Distribution of the transmissivity and major faults along the studied section for East (ESTSO) and West (ESTSW) tube

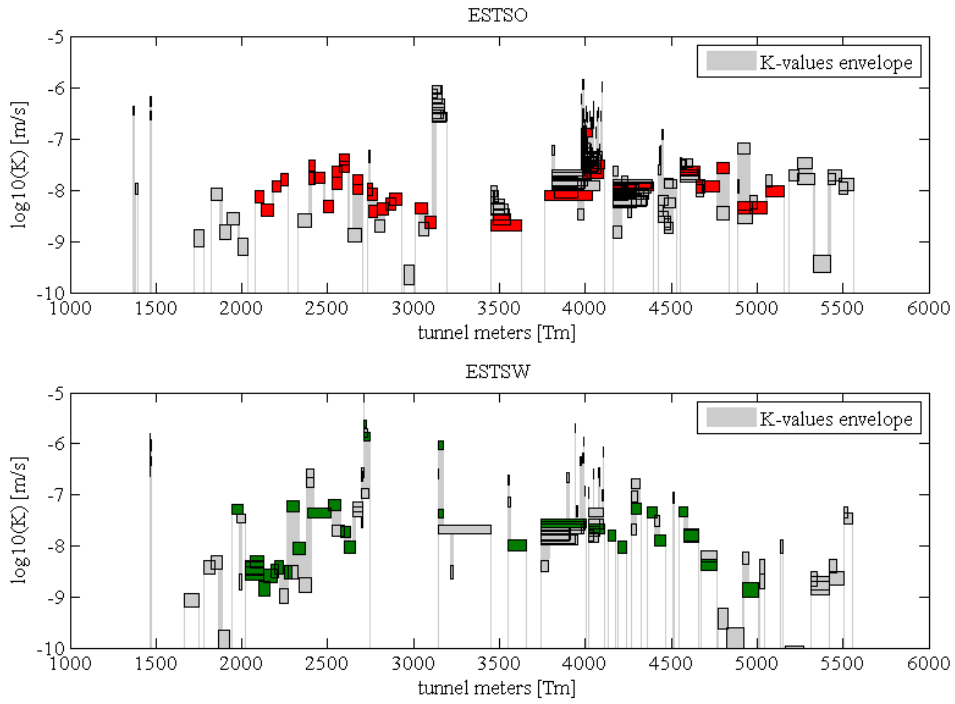


Figure 3-12 Raw K-values and K-envelope for East (ESTSO) and West (ESTSW) tube

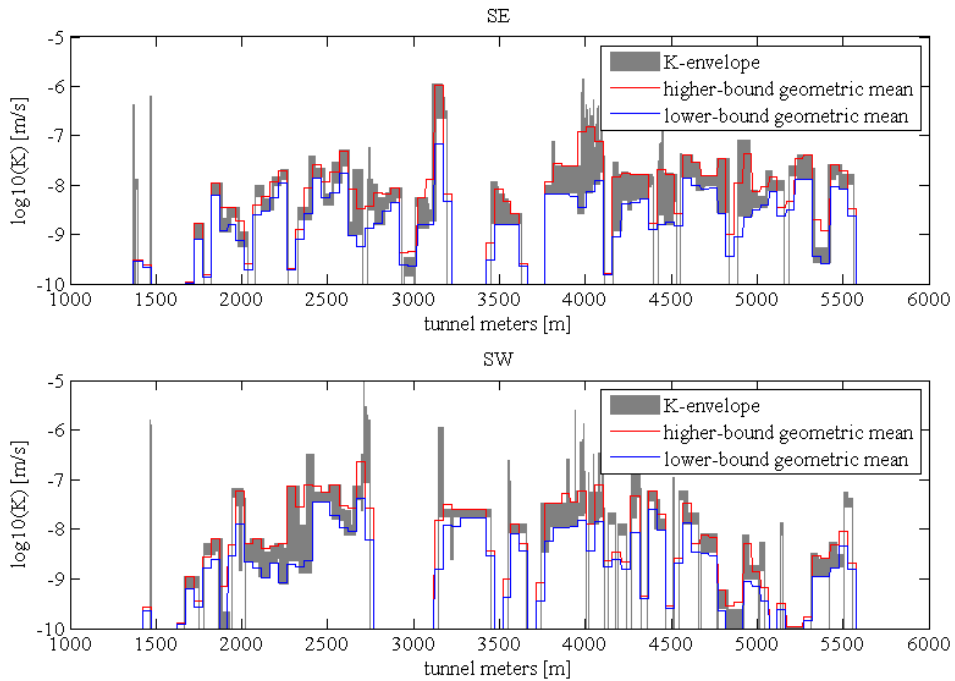


Figure 3-13 Geometric average of the K-envelope higher and lower bounds for East (SE) and West (SW) tube

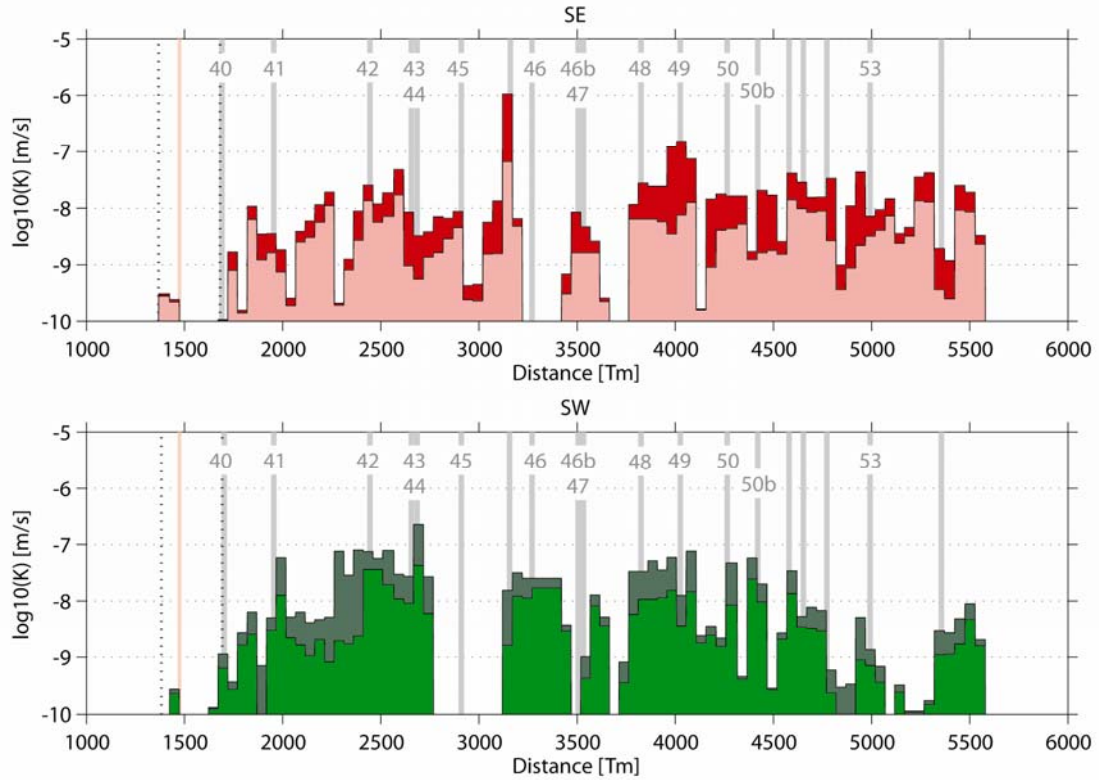


Figure 3-14 Processed K-distribution along tunnel for East (SE) and West (SW) tube

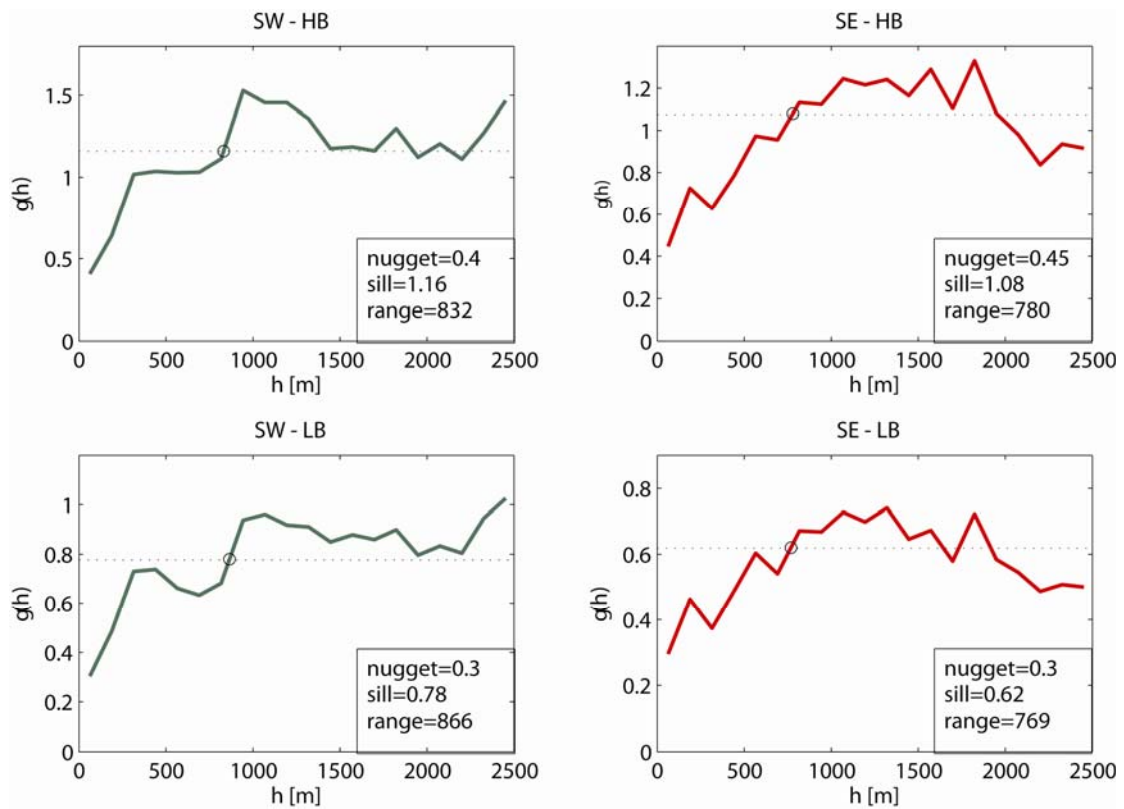


Figure 3-15 Semi-variograms of the K-values along the two tunnel tubes

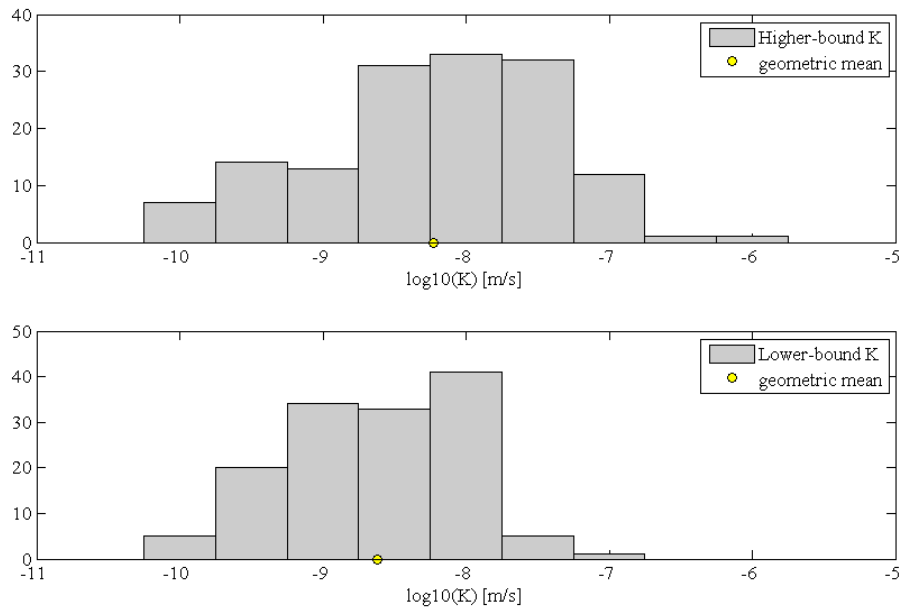


Figure 3-16 Hydraulic conductivity distribution

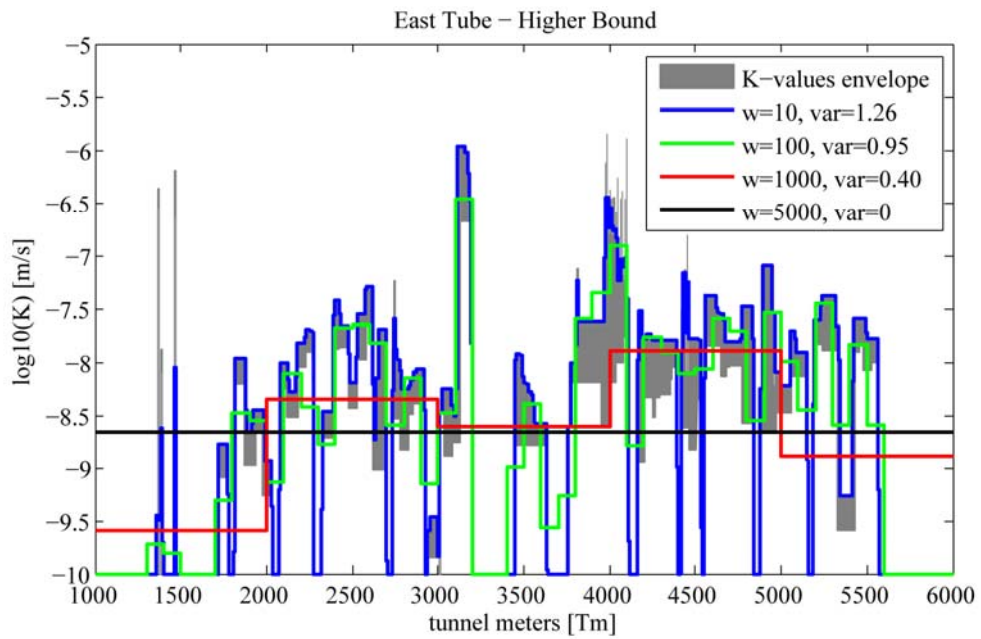


Figure 3-17 Variance versus interval length

4. Influence of hydraulic heterogeneity on transient tunnel inflows

4.1. Abstract

The prediction and the interpretation of the transient inflow rate to a tunnel during its excavation are difficult tasks since variations of the rock mass hydraulic conductivity and excavation speed can both lead to variations in the inflow. In the present paper, the authors focus on the impact of the spatial hydraulic conductivity distribution on transient tunnel inflows.

Two types of finite element models are implemented with the HydroGeoSphere numerical code. The first, a simple box model, simulates the instantaneous excavation of a tunnel with varying types of hydraulic conductivity distributions. The second model simulates the transient excavation of Gotthard Base Tunnel (GBT) South of the Sedrun shaft. Hydraulic conductivity values back-calculated from the inflow rate into boreholes belonging to a systematic pre-drilling campaign conducted along a 5 kilometer long section of the tunnel are used as input to the model.

The box model shows that individual inflows exhibiting non-radial flow dimensions may result of the channeling induced by a heterogeneous hydraulic conductivity field. The GBT model, implemented with four types of hydraulic conductivity distribution (constant, depth-dependent, constant with continuous fault planes and stochastic continuum) show that the stochastic model yields the best simulation of the inflow rate to a tunnel section during its excavation.

4.2. Introduction

The prediction of the inflow rate to underground excavations is of primary importance during the planning phase of a project. Two types of rate are necessary to consider, the steady-state rate and the maximum (initial) rate. The steady-state rate is required to design the long-term drainage system of an excavation; during the excavation phase, most relevant is the maximum inflow rate close to the tunnel face. The dimensioning of the pumping system of falling excavations strongly relies on the estimation of such maximum rates.

Both analytical and numerical approaches have been used in the past to calculate the inflow rate to an underground excavation. The analytical solutions are based on the steady-state solution of Polubarinova-Kochina (1962) and the Jacob and Lohman (1952) solution for transient flow to a well under constant drawdown. The steady-state inflow rate to a tunnel with varying assumptions on the boundary conditions and the hydraulic conductivity distribution has been studied for example by Goodman et al (1965), Zhang and Franklin (1993), Lei (1999; 2000), El Tani (2003), Kolymbas and Wagner (2007) and Park et al. (2008). Transient inflow rates to tunnels have been analytically investigated by Maréchal and Perrochet (2003), Perrochet (2005b, 2005a), Hwang and Lu (2007). Perrochet (2005a) proposed a simplified analytical formula for the computation of the transient discharge inflow rates into a tunnel or a well under constant drawdown. The Perrochet formula is used throughout the paper as a reference.

$$4-1 \quad Q(t) = 2\pi T s_0 G(\alpha)$$

$$4-2 \quad \alpha = \frac{Tt}{S_0^2}$$

$$4-3 \quad G(\alpha) = \frac{1}{\ln(1 + \sqrt{\pi\alpha})}$$

with, $Q(t)$, the inflow rate in function of the time (t), T , the transmissivity, s_0 , the drawdown, S , the storage coefficient and r , the well or tunnel radius.

All these analytical solutions assume radial flow. For non-radial flow, Doe (1991) proposed a solution for the transient inflow rate to a well under constant drawdown for any dimension (integer and fractional) based on the generalized radial flow model presented by Barker (1988). In the present study, this model is used to interpret some of the modeling results. Further details related to the Doe analytical solution can be found in the Appendix.

The finite element approach has been applied for steady state simulations (e.g. Jacob et al. 2010; Pesendorfer et al. 2009) and transient simulations (e.g. Molinero et al. 2002). Modeling of the excavation has been done implicitly (e.g. Jacob et al. 2010, Molinero et al. 2002) or explicitly (e.g. Coli et al. 2008).

Potentially important hydrogeological factors influencing transient tunnel inflow rates are:

1. The spatial distribution of multi scale hydraulic conductivity (e.g. Jacob et al. 2010) and storativity
2. The speed of excavation (e.g. Perrochet 2005b)
3. The presence/absence of draining pre-drillings
4. The length of the sampled tunnel section, including superposition of localized inflows
5. The hydraulic properties of brittle faults
6. The tunnel depth and boundary conditions at ground surface (e.g. water-table drawdown).

The objective of this paper is to study and discuss some of these factors in detail, based on a unique hydrogeological data set collected during the construction of the Gotthard Base Tunnel, predominantly from fractured crystalline rocks of the Gotthard massif. We first describe and analyze transient inflow rates reported from seven 500-900 meter long sections of Gotthard Base Tunnel. Then we describe the resulting tunnel inflows from 3D generic stochastic simulations implemented in the numerical code HydroGeoSphere (Therrien et al. 2010). And finally we use the observed transient inflows to evaluate the validity of different 3D conceptual flow models developed for the Gotthard Base Tunnel.

4.3. Hydrogeologic setting of the Gotthard Base Tunnel study section

The Gotthard Base Tunnel (GBT) (Figure 1) crosses the external crystalline massifs and the Penninic gneisses of the Central Swiss Alps. The 57 km long high-speed railway tunnel is composed of two tubes of 10 m diameter, separated by a distance of 40 m. The excavation of the eastern tunnel tube was completed in October 2010; the excavation of the western tube is expected to be completed in summer 2011. The tunnel was excavated simultaneously from 5 points of attack, defining the five different lots of Erstfeld, Amsteg, Sedrun, Faido and Bodio.

This paper focuses on a 5 km long section of the Sedrun lot located south of the Sedrun shaft (Figures 2 and 3) and excavated by drill-and-blast, which included a unique systematic hydrogeological investigation program. The program consisted of systematic pre-drillings with inflow logging and pore pressure monitoring, and detailed monitoring of transient tunnel inflow rates (chapter 3). Pre-drillings are sub-horizontal boreholes drilled ahead of the tunnel at the

excavation front. This hydrogeological monitoring program was motivated by pore pressure drainage induced surface settlements (Loew et al. 2000) and the existence of a concrete arch dam (Nalps hydropower dam) above the investigated tunnel section (Figures 2 and 3). The objective of the pre-drillings was to detect and eventually reduce large inflows to the tunnel in order to mitigate the surface settlements. The elevation of the tunnel is at about 530 m a.s.l. and the overburden increases from 897 in the north to 2026 m in the south. From a tectonic point of view, the section starts in the Tavetsch "massif" (TZM) in the North, crosses the Urseren-Garvera zone (UGZ) and ends in the Gotthard massif (GM) in the South.

The TZM is a 35 km wide (in NE-SW orientation) body of crystalline basement rocks in contact with the Aar massif (AM) in the North and the metamorphosed sediments of the Urseren-Garvera zone (UGZ) in the South (Figure 2-3). The UGZ (Ambühl, Huber, Niggli, Huber, Niggli, Flück and Lützenkirchen, 2008) mainly consists of the post-Variscan mono-metamorphic (greenschist facies) sediment cover of the Gotthard massif. The steeply dipping layers contain metasediments from Permo-Carboniferous to Jurassic ages. The GM is a 115 km long (in NE-SW orientation) crystalline body composed of pre-Variscan polyorogenic and polymetamorphic basement rocks, including gneisses, schists, migmatites and amphibolites, intruded by Variscan granitoids (Labhart, 1977). The Gotthard massif is subdivided in several lithologic units. In the present study only the northernmost GM lithologic unit is considered, the Gotthard "Altkristallin" which mainly consists of paragneisses, gneisses and stripped gneisses. All the above mentioned tectonic units present a NE-SW striking steeply dipping Alpine foliation and are intersected by steeply dipping faults of up to several km of visible length at ground surface. The thickness of the fault cores, mainly composed of tectonic cataclasites and gouge, typically ranges between a few decimeters and meters, while the entire width of fault zones can reach up to about hundred meters (Figure 3).

4.4. Observed transient inflow rates to the Gotthard Base Tunnel test section

Three types of inflow rate have been measured and reported by the drillers and on-site geologists:

1. Inflow rates to open boreholes drilled from the tunnel (mainly pre-drillings). These are presented and analyzed in detail in chapter 3.
2. Inflow rates to the tunnel excavation from major preferential groundwater pathways
3. Cumulative inflow rates to both tunnel tubes measured at selected cross-passages

Hydraulic conductivity values have been derived from the first rate type (chapter 3) and will be used as input for numerical modeling of the Gotthard Base Tunnel inflows. The second rate type consists of monthly measurements taken manually with a bucket and a watch. The third rate type consists of weakly measurements of inflow rates measured for tunnel sections of several hundred meters length. Figures 2 and 3 show the location of these individual sections along the tunnel and Figure 4 shows the corresponding measured transient rates. The different sections are identified in this paper by numbers ranging from 1 to 7 and described in Table 1. Only the cumulative flows from both tubes have been measured and cannot be separated for each tube. Moreover, the inflow rate to the different sections includes as well the water used by the miners (e.g. water for drilling boreholes) and the inflow rates to subsurface boreholes in these sections (pre-drillings included). Inflows from preferential flow path (mainly faults and joints) are well spread along the studied section, which means that each measurement section includes several inflow entry points. Figure 4 shows the location of the main faults and fault zones and the advance of the two tubes between 2004 and 2010. Fault zone numbers correspond to Figure 3.

The cumulative inflow rate of a measurement section remains null until the excavation of the first tube enters the section (Figure 4). Once the excavation of the section has started the rate increases and oscillates. This first phase is called "syn-excavation phase" in subsequent chapters. When the excavation of the section is completed by both tubes, the inflow rate tends to stabilize at a more or less constant value. This second phase is called "post-excavation phase". The oscillations of the inflow rate during the syn-excavation phase can have different origins. Increasing rates can be due to an increase in the excavation speed, the excavation/drilling of a more conductive rock-mass or preferential groundwater pathway, or an input of water through mining and pumping operations. Therefore the following interpretation of some of major (labeled) peaks in the cumulative inflow rates of Figure 4 needs some caution:

1. Peak (a) may result from the intersection of the "Spitzmeilenserie" with the West- and/or the East-tube (UGZ).
2. Peak (b) may result from the intersection of one or both tubes with the southern damage zone of fault zone FZ40.
3. Peak (c) may result from the intersection of FZ 41 with both tubes.
4. Peak (d) results from the intersection of FZs 43/44 with the SW tube.
5. Peaks (e) may result from the intersection of FZ49 and of zones of higher conductivity in the vicinity of FZ49.

The difficulty to interpret such cumulative inflow rates (especially from the syn-excavation phase) demonstrates the need for a better comprehension of the factors controlling transient tunnel inflow rates.

Table 4-1 Monitoring section details

Section#	Start [Tm]	End [Tm]	Length [m]	Color	Approximate mean depth [m]
1	912	1524	612	blue	1062
2	1524	2460	936	red	1050
3	2460	3372	912	green	1488
4	3372	4056	684	brown	1487
5	4056	4620	564	magenta	1638
6	4620	5268	648	violet	1749
7	5268	5892	624	cyan	1887

4.5. Generic numerical simulations (box model)

The purpose of generic box model simulations is twofold: test the accuracy of the numerical model against the analytical solution of Jacob and Lohman (1952) and investigate the effect of a heterogeneous hydraulic conductivity distribution on the transient inflow rate into an instantaneously excavated tunnel.

4.5.1. Numerical code description

The code used for the hydrodynamic modeling is HydroGeoSphere (Therrien et al. 2010) which is a 3D finite element code developed by the Groundwater Simulations Group at the Waterloo University. HydroGeoSphere

(HGS) has fully-integrated hydrologic, water quality, subsurface flow and transport capabilities. It simulates coupled surface and subsurface flow and transport using the control volume finite element method (or finite volume method).

4.5.2. Box model description

The box model is a cube with edges of 2000 meters (Figure 5). A tunnel crosses the cube from the centre of the left cube face to the centre of the right cube face. Boundary conditions are no flow through the bottom and lateral faces and constant head at the top face. The grid is build of cubic cells with edges of 40 m. The tunnel is modeled implicitly using tile drain segments (Therrien et al. 2010). The flow to each segment is calculated according to the general equation of continuity for flow in an open channel (Dingman 1994). The tunnel is connected to drain nodes at its intersections with the model boundaries in order to let the water flow out of the system. The tunnel radius is 5 m and the simulation of the tunnel excavation is not transient which means that the entire tunnel is excavated at once. The output time values range from 1 sec to 30`000 years.

4.5.3. Homogeneous-K box model description and results

The input parameters of the homogeneous-K model are constant hydraulic conductivity ($K=1.8 \times 10^{-9}$ m/s) and specific storage ($S_s=10^{-6}$ m⁻¹). The resulting inflow rate at each node defining the tunnel (boundary nodes excepted) is represented on Figure 6a with the Perrochet (2005a) solution calculated for the same conditions. Figure 6a shows that the results of the model and the results of the analytical solution only converge after a certain time span. This time span varies in function of the size of the cells surrounding the tunnel and the excavation diameter. The implicit modeling of the tunnel (tunnel simulated as a series of 1D segment) constrains the cell size in the vicinity of the tunnel. It was found by trial and error that the size of the elements surrounding the tunnel should be about four times bigger than the tunnel diameter (Figure 7). Similar conclusions regarding the relation between the cell size and the excavation size have been presented by Jacob (2010) for the implicit modeling of a tunnel with MODFLOW. Consequently, the time steps of any transient simulation using similar settings should be bigger than 1 day. According to the Perrochet solution, time steps shorter than one day would yield underestimated inflow rates. This modeling issue is particularly important in the case of wide excavations; in the

case of a borehole, the minimum cell size can be much smaller and the convergence between the analytical solution and the model is faster (Figure 6b).

4.5.4. Heterogeneous-K box model description and results

Random fields of hydraulic conductivity have been generated with the FGEN code (Robin et al. 1993). The mean hydraulic conductivity equals the conductivity of the preceding homogeneous box model ($K=1.8 \times 10^{-9}$ m/s), the variance equals 5 and the covariance function is exponential. Figure 8 shows the resulting inflow rate curves for each of the 51 nodes constituting the tunnel for diverse correlation lengths and anisotropies. For comparison purpose, the results of the Perrochet solution and of the preceding homogeneous box model are plotted as well. The three isotropic realizations (Figure 8a-c, correlation lengths: 200x200x200 m, 500x500x500 m, 1000x1000x1000 m) show a decrease in the variability of the rates when the correlation length increases. In the case of planar (xz-plane, Figure 8 d-e) and linear (z-direction, Figure 8 f-g) anisotropies the variability of the inflow rate increases with the correlation length. The heterogeneous hydraulic conductivity does not only induce a variability of the inflow rate at a given time value but also a variation in the speed of the rate decrease (variation in the slope of the curves at a given time). Figure 9 shows a zoom of Figure 8 top left plot and suggests that the simulated heterogeneous hydraulic conductivity yields variability in the flow dimension. It also shows that inflows exhibiting a high "initial" rate tend to have a lower flow dimension. Note that the flow dimension of the Perrochet model is 2 (radial flow).

4.6. Numerical simulations of the Gotthard Base Tunnel

The objectives of Gotthard Base Tunnel simulations are to compare diverse conceptual hydrogeological models for large scale flow in fractured rocks with the systematically measured transient inflows, taking into account the progressive excavation of two individual tunnel tubes. The models include variations in the distribution of hydraulic conductivity. The models are described with increasing complexity, starting from homogeneous distributions and ending with stochastic distributions.

4.6.1. General model settings

The model boundaries of the regional model consist of the Vorderrhein River to the North, the Rhein da Medels River to the East, the crest from the pass at the top of the Curnera Valley to Songta Maria Lake to the South and the Rhein da Curnera River to the West (Figure 2). The bottom boundary has a constant elevation of -5000 m and the top boundary corresponds to the real topography as interpolated from a 25-meter DEM.

The mesh is composed of hexahedral elements (bricks) of varying edge sizes (from 25 to 1000 m). Cells in contact with the tunnel are boxes of 25 by 50 by 50 meters (x,y and z). The number of nodes is 452808, the number of elements 431424 and the number of layers 52 (Figure 10).

All external model boundaries, upper boundary excepted, are set to the no-flow-type (Neumann boundary condition with flux equal to zero). The surface river nodes are assigned a Dirichlet boundary condition (constant hydraulic head) with head-values set equal to the node elevation (blue dots on Figure 10). The ground surface has a mixed Dirichlet-Neumann boundary condition (seepage face condition). An infiltration rate (rainfall) is applied to these faces under the condition that the hydraulic head does not overpass the surface elevation (Forster and Smith, 1988). When the head tends to overcome the surface elevation, the surface faces exfiltrate water. The infiltration rate has been set to 10^{-8} m/s, according to Table 2.

Table 4-2 Typical infiltration rate values from other studies located in the Central Swiss Alps.

Recharge [m/s]	Location	Description	Reference
9.51×10^{-9}	Gotthard massif	Crests and steep slopes	(Loew and Herfort, 2006)
1.81×10^{-7}	Gotthard massif	Shallow dipping slopes	(Loew and Herfort, 2006)
3.35×10^{-8}	Loetschberg	Annual mean	(Pesendorfer, 2006)
4.85×10^{-8}	Loetschberg	Maximum	(Pesendorfer, 2006)
1.64×10^{-8}	Loetschberg	Minimum	(Pesendorfer, 2006)
1.44×10^{-8}	Rotondo	Spatial mean	(Oftringer, 2001)

The tunnel is simulated using tile drain segments (Figure 11). The drain diameter is set to 10 m. The tunnel is connected to a constant head node at its intersections with the model boundaries in order to let the water flow out of the

system (white spheres on Figure 11). The simulation of the tunnel tube excavation is transient which means that the tunnel tubes are excavated in many time steps.

Fully saturated flow is assumed over the whole model domain. A pseudo water-table surface is defined where the hydraulic head equals the elevation. This is sufficient for the purpose of the regional model (tunnel inflows) and the highly fractured and permeable rocks in the near surface (Masset and Loew 2010).

The transient simulation starts in 1990 and ends in 2010. The output times are not uniformly distributed. The excavation time of the simulated tunnel nodes was linearly interpolated from the tunnel advance versus time curves (Figure 4). One time step corresponds to the excavation of one tunnel segment, ranging from 50 to 60 m. Therefore the length of an excavation time step is a function of the excavation speed of the corresponding tube segment. The simulation time steps should not be smaller than the excavation time steps to avoid artifacts as illustrated on Figure 12.

4.6.2. Homogeneous K GBT model

The first conceptual model assumes constant hydraulic conductivity and specific storage values. Initially, the assigned hydraulic conductivity value equals the geometric average of the hydraulic conductivity values back-calculated from the inflow rate to other tunnels and galleries located in the same Gotthard "Altkristallin" geological unit at the corresponding tunnel depth ($K=8.15 \times 10^{-9}$ m/s, black and blue lines in Figure 13) (Masset and Loew, 2010). The specific storage is set to 10^{-6} m^{-1} (chapter 3). In a second step, calibrated hydraulic conductivity and specific storage values have been derived with the PEST parameter estimation code (Doherty, 2005) from the inflows observed in the GBT (red line in Figure 13).

Figure 14a shows the measured- (dots) and modeled (lines) rates with constant hydraulic conductivity and specific storage values ($K=8.15 \times 10^{-9}$ m/s, $S_s=10^{-6} \text{ m}^{-1}$). Figure 14b shows the measured- (dots) and modeled-rates (lines) with calibrated constant hydraulic conductivity ($K=1.8 \times 10^{-9}$ m/s) and specific storage ($S_s=5.8 \times 10^{-7} \text{ m}^{-1}$) values. On Figure 14a the modeled rates are overall too high compared to the measured rates. On Figure 14b, a relative good fit of the inflow rate is achieved for most inflow monitoring sections, highest rates of the green and brown sections excepted. The modeled inflow rates show similar behavior as the measured one: they first increase and oscillate before to slowly decrease and stabilize. The first phase corresponds to the syn-excavation phase of one or both tubes, the second phase to the post-excavation phase. The variation

of the excavation speed and the superposition of the two tubes induce the oscillations of the first phase. This again illustrates the difficulty to interpret measured inflow rates.

4.6.3. Depth dependent K GBT model

The second model series assume a constant specific storage and a decreasing hydraulic conductivity with depth. A power-law relationship between hydraulic conductivity and depth is assumed (Figure 13) from the values back calculated from inflows to other subsurface excavations in the study area (Masset and Loew 2010). The advantage of the power-law model over a negative exponential model is to better fit the shallow hydraulic conductivity values (dashed blue curve of Figure 13). The power-law parameters are derived by the fitting this dataset and a specific storage of $S_s=10^{-6}m^{-1}$ is assumed. In a second step, the function of the hydraulic conductivity and the specific storage are recalibrated for the transient inflows to the GBT section (dashed red curve in Figure 13). In this case not all parameters of the power-law function are optimized. The curve is only allowed to shift along the hydraulic conductivity axis because the depth range of the studied section of GBT is too narrow to constrain the overall trend of the function; it only constrains the hydraulic conductivity value at the tunnel depth.

Figure 15a shows the measured- and modeled-rates with a constant specific storage ($S_s=10^{-6}m^{-1}$) and a depth-dependent hydraulic conductivity (Figure 13). Figure 15b shows the measured- and modeled-rates with the locally optimized specific storage ($S_s=3.0 \times 10^{-6}m^{-1}$) and function of hydraulic conductivity with depth (Figure 13). Figure 16 shows the optimized inflow rates with and without hydraulic conductivity variation with depth and Figure 17 shows the steady-state water-table elevation above the tunnel for both models. The recalibrated depth-dependent K model exhibits higher rates for the shallower sections (1 and 2), lower rates for the others and a general lower water table elevation.

4.6.4. Continuous fault zone GBT model

The third model assumes a homogeneous rock mass with constant hydraulic conductivity and specific storage ($K=1.8 \times 10^{-9} m/s$, $S_s=10^{-6}m^{-1}$) intersected by ten fault zones with identical transmissivity, simulated as isotropic and homogeneous planar structures entirely cross-cutting the model (Figure 18).

The location and orientation of the fault zones corresponds to some of the mapped fault zones of Figure 3. Water exchange between the matrix and the fault zones is included. In a set of simulations the fault zones have been assigned diverse hydraulic conductivities (K) and a constant width (W), leading to transmissivity values ranging from $2.0 \times 10^{-7} \text{ m}^2/\text{s}$ to $2.0 \times 10^{-4} \text{ m}^2/\text{s}$. Figure 19 shows that the increase in fault zones transmissivity results in a decrease of the tunnel inflow rate and Figure 20 shows that the steady-state water table elevation decreases as the transmissivity of the fault zone planes increases. Fault zone planes with a higher transmissivity induce a lower water table elevation. The simulation of transmissive planes does not create new peaks in the modeled inflow rates.

4.6.5. Stochastic hydraulic conductivity GBT model

The fourth model series assumes that the hydraulic conductivity distribution is a Gaussian random field conditioned by fixed local values around each tunnel tube. The turning band simulation method was selected to generate the hydraulic conductivity fields (Emery and Lantuéjoul 2006). The method allows generating random field conditioned by fixed local values. It is assumed that the local hydraulic conductivity around each tunnel tube is known and corresponds to the hydraulic conductivity values back-calculated from the inflow rate to the pre-drillings (chapter 3) plotted on Figure 21. In this study higher and lower bound hydraulic conductivity values have been defined for each 50 m interval of each tube, "dry" intervals excepted. A threshold hydraulic conductivity of 10^{-10} m/s has been assigned to the "dry intervals". This threshold values has been back-calculated from the water vapor input to 1000-m-long dry section of Gotthard Base Tunnel (Masset and Loew 2010). Figure 22 shows empirical variograms of the hydraulic conductivity for each tube and for the higher (HB) and lower (LB) bound values. The exponential covariance model was chosen for the generation of the Gaussian random fields (no nugget, sill=1, exponential). Due to the model element varying size as a function of distance to the tunnel, the generated random fields had to be up-scaled. The hydraulic conductivity value of each cell of the grid was defined as the geometric mean of all the included values. Figure 23 shows an example of such an upscaled field and Figure 24 shows vertical and horizontal cross-sections through one random realization with a correlation length (cl) of 500 m. Figures 25-30 show the modeled rates for varying correlation length ($cl=250$, $cl=500$ and $cl=1000$) with higher- and lower-bound K -values for each

monitoring section (lines). Measured values are plotted for comparison purpose as well (dots).

From a general point of view, the lower bound K-values yield inflow rates that are closer to the measured values. By analogy with the stochastic box model, in case of isotropic correlation length, the variability of the inflow rate decreases as the correlation length increases. The location of the peaks in inflow rate depends on the distribution of local K-values only which is constant over all realizations. In contrast, the amplitude of the peaks depends on the realization. This means that the amplitude depends on the K-values of the non-conditioned cells of the model. Looking at the sections individually, modeled rates (lower bound) of sections 3, 4 and 5 are the closest to the measured rates. Figure 31 compares modeled rates of one realization of the stochastic model (lower bound K and 500 m isotropic correlation length) with modeled rates of the constant K model and shows significantly different rate curve patterns. The location of some of the rate peaks changes with the introduction of heterogeneity in the hydraulic conductivity distribution of the model. In the stochastic simulations the increase and decrease of inflow rates is generally faster and the rate peaks sharper.

4.7. Discussion

4.7.1. Study limitations

Limitations related to the measured tunnel inflow data

As mentioned earlier, the inflow rates to the different monitoring sections include as well the water introduced by the mining operations (e.g. water for drilling) and the inflow rate from boreholes located in these sections (pre-drillings included), whereas in the GBT models, no boreholes or input of water through mining operations are simulated. Moreover, the relative low frequency of the rate measurement (one per week in mean) does not guaranty a systematic sampling of the highest initial inflow rates. The most reliable part of the rate time series is the post-excavation phase (no extra input of water from pre-drillings and mining operations).

Limitations related to the modeling approach

As long as the time/excavation steps of all GBT models are longer than the time needed for the Perrochet solution and the finite element model to converge, the implicit modeling of the tunnel does not underestimate the

transient inflow rate. In the present study, the frequency of the time steps is comparable to the frequency of the measurements and the time/excavation steps are longer than the time needed for convergence. On the other side, these long time steps also imply that some of the highest early time inflows are not captured by the model. This is why some of high inflow rate peaks (for example peak d in section 3, resulting from fault zone 43/44) are not reproduced in the simulations, even in case of the explicitly modeled high transmissivity faults (Figure 19).

If smaller time/excavation steps were needed to assess the maximum early time inflows, the only solution would be to model the tunnel explicitly. However, in reality very early time inflows only occur in pre-drillings (like peak d in monitoring section 3); because the inflows to the excavated tunnel sections have been reduced by pre-excavation pore pressure drainage.

Considering the GBT stochastic models with varying cell size, the generated random hydraulic conductivity fields had to be upscaled over each cell of the model. This artificially decreases the variability of hydraulic conductivity in the bigger cells. Furthermore the Ababoo criterion (cell size at least smaller or equal to a fifth of the correlation length) is not fulfilled for the larger cells. Ten different realizations have been generated for each parameter set. The number of realizations is too small to derive statistics like the mean or the variance of the inflow rate, but it is for example sufficient to describe relationships between the correlation length and the variability in the inflow rate.

Finally, input parameters such as infiltration rate and specific storage are not well constrained because no data were available. These parameters have been assigned values according to the literature. Results of the present paper are dependent on the values attributed to these parameters. The effects of the variation of these parameters on the results are beyond the scope of this study.

4.7.2. Impact of the spatial distribution of hydraulic conductivity

Box models

The comparison of results of both homogeneous-K and heterogeneous-K box models show that a heterogeneous K-field not only induces variations in the early and steady-state inflow rates but can modify the apparent flow dimension as well. It was observed that tunnel nodes with a higher early rate tend to have transient inflows representing a lower flow dimension. Starting from a tunnel

node located in a relative conductive zone, the pore-pressure perturbation will be somehow bounded by zones of lower conductivity because the pore pressure propagation in these zones is much slower. Consequently, flow channeling is induced. In contrast, starting from a tunnel node located in a low conductivity zone, the pore pressure perturbation preferentially spreads in the neighboring zones of higher conductivity.

GBT models

The comparison of results of the homogeneous K and depth-dependent K models show that once the model is calibrated with local tunnel inflow data the simulated transient rates are similar. Slightly higher rates are simulated with the depth-dependent model for the shallower monitoring sections (1 and 2) and slightly higher rates for the deeper monitoring sections (3, 4, 5, 6 and 7). In the present study this effect is of little significance; the measured rates are not clearly better fitted by either model. This effect could be of higher significance in the case of a vertical shaft for example. The steady-state water table elevations of these two models show differences which could be significant when environmental impacts have to be assessed. Consequently, when the inflow rate is the only interest and the difference in overburden does not significantly change along the excavation the constant K model is sufficient for most practical inflow prediction purposes. Note that in such a case the numerical simulation might be advantageously replaced by a less time-consuming analytical solution such as presented by Perrochet (2005b).

The lowering of the inflow rate obtained by addition of persistent higher permeability fault planes to the homogeneous permeability matrix model is somehow counterintuitive. With higher conductivity one would expect higher rates. However, the comparison of the water table elevation at steady-state shows that a significant decrease of the water table at steady-state occurs when higher K fault planes are added. Besides the lowering of the water table, no significant change in the pattern of the hydrographs is observed; the number of rate peaks does not increase and their location is unchanged. In theory, the higher K fault planes should yield higher initial/early inflow rates but the model time steps duration is most probably too long to capture the higher initial rates. This is why this peak is never reproduced in the simulations, even in case of the explicitly modeled high transmissivity faults (Figure 19). At steady-state, the inflow rate to the tunnel seems to be controlled by the conductivity and flow from the adjacent

rock mass. This might be due to the fact that the higher K planes are fed by the porous medium and that the amount of water that percolates from the porous medium to the higher K planes is controlled by the conductivity of the porous medium.

The stochastic model showed that the location of the transient rate peaks depend on the distribution of hydraulic conductivity in the cells that are contiguous to the tunnel tubes. These cells are conditioned and do not change over the different realizations. Therefore, the location of the inflow peaks is independent from the realization. In contrast, the variation of the amplitude of the inflow peaks demonstrates that the amplitude depends on non-conditioned cells that are not in direct contact with the tubes. When the correlation length gets higher, the variability of the hydraulic conductivity inside these cells gets lower and consequently, the variability in the inflow rate gets smaller as well. The pattern of the rate curves differs from the pattern of rate curves obtained with the other models (constant K, depth-dependent K and high K planes).

4.7.3. Impact of the excavation speed

In case of constant hydraulic diffusivity, the excavation speed determines the advance of the pore pressure perturbation in front of the excavation face. When the excavation is faster, the tunnel is excavated through a rock mass of lesser disturbed pore pressure (Perrochet, 2005b). Figure 4-32 presents two horizontal cross-sections at the tunnel elevation (a, b) and a plot of the inflow rate in function of the time (c). Cross-section (a) shows the head distribution at a specific time value, and cross-section (b), the head distribution at the following time value. The time step preceding the first time value is large and the excavation speed slow. In contrast the time step separating the first and the second time values is short and the excavation speed fast. It can be seen close to the excavation front (a, b) that when the excavation speed is higher the isolines are characterized by a smaller spacing and a narrower angle at the intersection with the tunnel. This is more complex in the case of heterogeneous diffusivity because the advance of the pore pressure perturbation depends on both the distribution of the diffusivity and the excavation speed.

4.7.4. Adequacy of the different models in the context of the GBT

The best fits of the measured rates are obtained with the calibrated constant and depth dependent hydraulic conductivity models. The post-excavation phase rates are better fitted than the syn-excavation rates. In the present study, a satisfactory reproduction of the late time rates is obtained without introducing heterogeneity to the model. This means that at a late time the rock-mass surrounding each section behaves like a REV. In the test section the size of the REV should be smaller than 500 meters, because the steady state rates of all monitoring intervals are impressively similar. Compared to the regional analysis of Masset and Loew (2010), that includes a systematic analysis of late time tunnel inflows to 25 underground excavations in the Aar and Gotthard massifs, the test section is a representative sample (compare with Figure 13). However, it is known that significantly higher transmissive fractures also occur at similar tunnel depth in these tectonic units. Such structures have not been intersected by the Gotthard Base Tunnel in the studied section but elsewhere. The impacts of such highly transmissive structure (both close to surface and at greater depth) have not been studied in this paper.

The introduction of persistent and higher K fault planes to the model did not improve the reproduction of the observed inflow rates. Considering the low correlation between the local conductivity values derived from the pre-drillings of each tube (chapter 3), such a model is not appropriate for the data of our test section. At this scale homogeneous higher conductive planes spanning the whole model seem unrealistic. The existence of heterogeneity in the hydraulic properties of the rock mass is obvious but the structures responsible for the higher conductivities are smaller than the massif-scale in the test section.

The stochastic simulations yielded the best reproduction of the syn-excavation rates. However, the simulated inflow rates of the syn-excavation phase show less variability than the observed rates. This smoothing might be related to the spatial and temporal discretization of the model. Some sections are better reproduced than others by the stochastic model. Local misfits of the measured rates can be explained by many factors, such as the volume tested by the pre-drillings, the uncertainty in the geostatistical properties in the vertical and transversal directions, and the uncertainties related to scaling effects.

Although not the focus of this paper, the modeled water table elevations and drawdowns are compatible with field observations. These observations show

that springs in the upper Nalps valley (south of the Sedrun shaft) have not been significantly impacted by the Gotthard Base Tunnel.

4.7.5. Overestimation of tunnel inflow rates

All the models using hydraulic conductivity values back-calculated from the inflow rate to other tunnels or to pre-drillings yield overestimated rates. Among these, the one using the lower bound K-values derived from the pre-drillings is the closest to reality. The geometric average of the lower bound K-values is close to the optimized K-value for the constant K model.

A faster decrease of the inflow rate than predicted with the radial flow model has often been observed in several tunnels and galleries of the Aar and Gotthard massifs. These data and their interpretation will be presented in a future publication. The stochastic box model offers a sensed explanation for individual inflow rates with an apparent flow dimension lower than 2. The heterogeneous distribution of the hydraulic conductivity gives rise to flow channeling which implies a reduction of the flow dimension. The authors do not say that it is the only valid explanation; other phenomena such as hydro-mechanical coupling could also be invoked. For example, Ivars (2006) demonstrated that a stress-permeability coupling effect can as well explain the overestimation of the inflow rate when estimating from pre-drillings; when the excavation radius increases, the tangential stress around the excavation increases, leading to a local decrease of the hydraulic conductivity.

4.8. Conclusion

In this paper, the impact of the spatial hydraulic conductivity distribution on transient tunnel inflow rates has been investigated by the mean of 3D finite element models (HydroGeoSphere hydrogeological code). Two types of model have been implemented: a simple box model simulating the instantaneous excavation of a tunnel and a more complex model simulating the transient excavation of Gotthard Base Tunnel (GBT) South of the Sedrun shaft, both assuming diverse types of spatial hydraulic conductivity distribution. The objectives of the first model were (1) the check of numerical model and modelling techniques against the Jacob and Lohman solution and (2) the comparison of simulated transient inflow rates with homogeneous and Gaussian hydraulic conductivity fields. The goals of the second model were (1) the validation of hydraulic conductivity distributions derived in chapters 2 and 3 and

(2) the comparison of simulated transient inflow rates assuming varying conceptual models for the distribution of hydraulic conductivity (homogeneous, depth-dependent, major faults with enhanced transmissivity and Gaussian distribution of hydraulic conductivity).

With respect to the finite element modeling of a tunnel the authors have shown that the implicit modeling of a tunnel constrains the cell size in the vicinity of the simulated tunnel (cell size about four times bigger as the tunnel diameter) and that the simulated transient rate only converges with the analytical solution after a time span which is a function of the cell size in the vicinity of the tunnel (large excavations imply longer times for convergence).

Concerning the transient behavior of individual inflows it was shown that individual inflows exhibiting relative rapid flow rate decrease can be approximated by non-radial flow which can be the result of channeling induced by a heterogeneous hydraulic conductivity field.

Considering the transient cumulated flow to a tunnel section it was shown that during the syn-excavation phase, inflow peaks can result from a change in the rock properties or a change in the excavation speed. The post-excavation rates of the monitoring sections can be reproduced with a homogeneous hydraulic conductivity model; meaning that, the rock mass compartments defined by the different sections behave like REVs.

The distribution of hydraulic conductivity with depth in the GBT model impacts on the water table elevation; with a depth-dependent hydraulic conductivity distribution the modeled water table position is lower than with a constant hydraulic conductivity. The higher transmissivity of the continuous fault planes results in lower position of the steady-state simulated water table. The water table position and the hydraulic conductivity of the blocks in between the fault planes control the modeled late time inflow rate. (The model time steps are too big to allow the observation of inflow peaks generated by continuous conductive fault planes.)

The stochastic GBT model yielded the best simulations of the syn-excavation phase. The position of the rate peaks is function of the local hydraulic conductivity values of the conditioning cells in contact with the tunnel and therefore is invariant. In contrast the amplitude of the peaks depends on more distant unconditioned cells.

Finally, when incorporated to the GBT model, hydraulic conductivity values back-calculated from pre-drilling inflows yielded overestimated tunnel inflow

rates. The smallest difference between the measured and the modeled rates was obtained with the hydraulic conductivity lower-bound values derived from the pre-drillings inflow rates (calibrated models excepted). In the case of a transient inflow of flow dimension lower than two, the prediction of the inflow rate with the radial flow model results in a systematic overestimation of the inflow rate.

4.9. Acknowledgments

The authors acknowledge the support from AlpTransit Gotthard AG (H. Ehrbar, P. Guntli) and the designers of HydroGeoSphere (R. McLaren, E. Sudicky, R. Therrien) for giving access to the code and support.

4.10. Appendix: Hydraulic conductivity derivation for fractional flow dimensions

Doe (1991) gave the Laplace transform space solution of the transient flow rate to a well under constant drawdown (equation 4-4):

$$4-4 \quad \bar{Q}(p) = \frac{H_0 K b^{3-n} \alpha_n r_w^{n-2} (\lambda r_w) K_{\nu-1}(\lambda r_w)}{p K_{\nu}(\lambda r_w)}$$

$$4-5 \quad \alpha = \frac{2\pi^{n/2}}{\Gamma(n/2)}$$

$$4-6 \quad \lambda = (p S_s / K)^{1/2}$$

$$4-7 \quad \nu = 1 - \frac{n}{2}$$

with H_0 , the constant head, K , the hydraulic conductivity, b , the length of the borehole, n , the flow dimension, r_w , the radius of the well, $K_{\nu}(\dots)$ and $K_{\nu-1}(\dots)$, modified Bessel functions, p , the Laplace space variable, $\Gamma(\dots)$, the gamma function and S_s , the specific storage. The inversion of equation 4-4 gives the generalized radial-flow solution for transient flow to a well under constant drawdown. Doe as well defined dimensionless rate and time variables to simplify equation 4-4:

$$4-8 \quad Qd = \frac{Q}{h K b^{3-n} \alpha r_w^{n-2}}$$

$$4-9 \quad td = \frac{\eta^* t}{r_w^2}$$

with Qd , the dimensionless rate, Q , the rate, h the head, td , the dimensionless time and η , the hydraulic diffusivity. Using these dimensionless variables reduces equation 4-4 to:

$$4-10 \quad Qd = \frac{K_{y-1}(\sqrt{s})}{\sqrt{s}K_y(\sqrt{s})}$$

with s , the Laplace space variable. The inversion of equation 4-10 returns the dimensionless rate as a function of the dimensionless time.

The hydraulic conductivity (K) can be derived from the combination of equations 4-8 and 4-10 for given borehole length (b), head (h), rate (Q), well radius (r), specific storage (S_s), time (t) and flow dimension (n). K can then be re-injected in equation (5) to derive $Q(t)$ for a series of time values.

4.11. References

- Ambühl E, Huber HM, Niggli E, Huber W, Niggli M, Flück W, Lützenkirchen V (2008) Geologischer Atlas der Schweiz, Nr. 126, Blatt 1232 Oberalppass - Karte und Erläuterungen.
- Barker JA (1988) A Generalized Radial Flow Model for Hydraulic Tests in Fractured Rock. *Water Resour Res* 24: 1796-1804
- Coli N, Pranzini G, Alfi A, Boerio V (2008) Evaluation of rock-mass permeability tensor and prediction of tunnel inflows by means of geostructural surveys and finite element seepage analysis. *Engineering Geology* 101: 174-184 DOI DOI: 10.1016/j.enggeo.2008.05.002
- Dingman LS (1994) *Physical hydrology* Prentice- Hall, Englewood Cliffs, N.J.
- Doe TW (1991) *Fractional Dimension Analysis of Constant-Pressure Well Tests*. Society of Petroleum Engineers 22702
- Doherty J (2005) *PEST - Model-Independent Parameter Estimation - User Manual: 5th Edition*
- El Tani M (2003) Circular tunnel in a semi-infinite aquifer. *Tunnelling and Underground Space Technology* 18: 49-55
- Forster C, Smith L (1988) Groundwater flow systems in mountainous terrain: 2. Controlling factors. *Water Resour Res* 24: 1011-1023 DOI 10.1029/WR024i007p01011
- Goodman RE, Moya DG, Schalkwyk AV, Javandel I (1965) GROUND WATER INFLOWS DURING TUNNEL DRIVING. *Bull Assoc Eng Geol* 2: 39-56
- Hwang J-H, Lu C-C (2007) A semi-analytical method for analyzing the tunnel water inflow. *Tunnelling and Underground Space Technology* 22: 39-46
- Jacob Z, Bradley M, David B (2010) Simulating Seepage into Mine Shafts and Tunnels with MODFLOW. *Ground Water* 48: 390-400
- Kolymbas D, Wagner P (2007) Groundwater ingress to tunnels - The exact analytical solution. *Tunnelling and Underground Space Technology* 22: 23-27
- Labhart TP (1977) *Aarmassiv und Gotthardmassiv Gebrüder Borntraeger*, Berlin-Stuttgart
- Lei S (1999) An Analytical Solution for Steady Flow into a Tunnel. *Ground Water* 37: 23-26
- Lei S (2000) Steady Flow into a Tunnel with a Constant Pressure Head. *Ground Water* 38: 643-644

- Loew S, Herfort M (2006) Zeitliche Entwicklung der Setzungen im Gotthard-Massiv bei Nalps: Untersuchungen mit einem vereinfachten hydrogeologischen Modell. In: AlpTransit (ed) AlpTransit Gotthard Fachkommission - Vortriebe und Stauanlagen - Gotthard Basistunnel, Los 360 Sedrun.
- Maréchal J-C, Perrochet P (2003) Nouvelle solution analytique pour l'étude de l'interaction hydraulique entre les tunnels alpins et les eaux souterraines. Bull Soc géol Fr
- Mas Ivars D (2006) Water inflow into excavations in fractured rock--a three-dimensional hydro-mechanical numerical study. International journal of rock mechanics and mining sciences 43: 705-725
- Masset O, Loew S (2010) Hydraulic conductivity distribution in crystalline rocks, derived from inflows to tunnels and galleries in the Central Alps, Switzerland. Hydrogeology Journal 18: 863-891 DOI 10.1007/s10040-009-0569-1
- Molinero J, Samper J, Juanes R (2002) Numerical modeling of the transient hydrogeological response produced by tunnel construction in fractured bedrocks. Eng Geol 64: 369-386
- Ofterdinger US (2001) Ground water flow systems in the Rotondo Granite, Central Alps (Switzerland). PhD Thesis, ETHZ
- Park K-H, Owatsiriwong A, Lee J-G (2008) Analytical solution for steady-state groundwater inflow into a drained circular tunnel in a semi-infinite aquifer: A revisit. Tunnelling and Underground Space Technology 23: 206-209
- Perrochet P (2005a) A simple solution to tunnel or well discharge under constant drawdown. Hydrogeology Journal 13: 886-888
- Perrochet P (2005b) Confined Flow into a Tunnel during Progressive Drilling: An Analytical Solution. Ground Water 43: 943-946
- Pesendorfer M (2006) Hydrogeologic Exploration and Tunneling in a Karstified and Fractured Limestone Aquifer (Lötschberg Bas Tunnel, Switzerland). PhD Thesis, ETHZ
- Pesendorfer M, Loew S, Zappa M (2009) Environmental impacts of the Lötschberg Base and Crest Tunnels, Switzerland. Paper presented at the Eurock 2009 - Rock Engineering in Difficult Ground Conditions - Soft Rocks and Karst, Dubrovnik2009
- Polubarinova-Kochina PY (1962) Theory of Ground Water Movement Princeton University Press, Princeton, New Jersey

- Robin MJL, Gutjahr AL, Sudicky EA, Wilson JL (1993) Cross-Correlated Random Field Generation With the Direct Fourier Transform Method. *Water Resour Res* 29: 2385-2397 DOI 10.1029/93wr00386
- Therrien R, McLaren RG, Sudicky EA (2010) HydroGeoSphere—a three-dimensional numerical model describing fully-integrated subsurface and surface flow and solute transport. In: Group GS (ed) (draft ed) University of Waterloo.
- Zhang L, Franklin JA (1993) Prediction of water flow into rock tunnels: an analytical solution assuming an hydraulic conductivity gradient. *Int J Rock Mech Min Sci* 30: 37-46

4.12. Figures

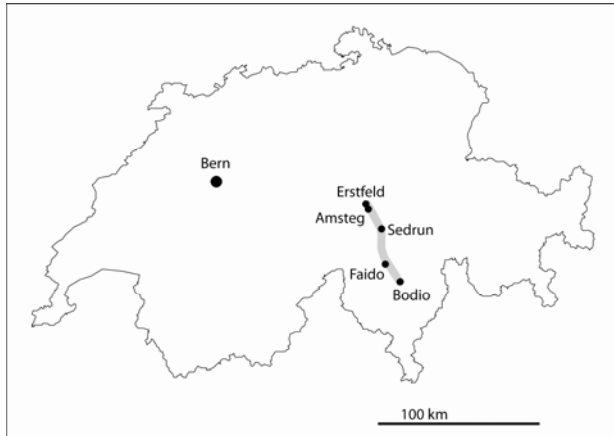


Figure 4-1 Location of Gotthard Base Tunnel

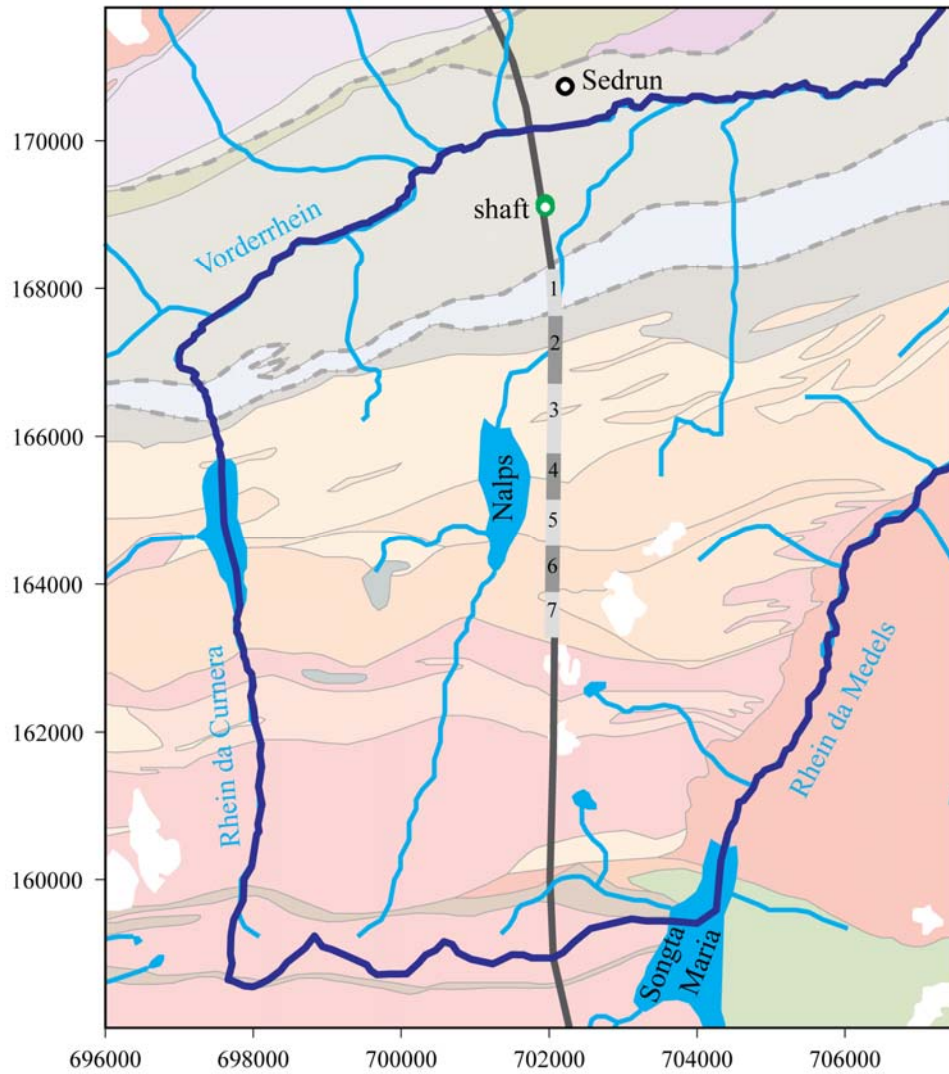


Figure 4-2 Studied section location with the different monitoring intervals (pale and medium grey, 1-7), the model perimeter (dark blue line), the location of the Nalps and Songta Maria lakes, the location of the main rivers (Vorderrhein, Rhein da Curnera and Rhein da Medels), the location of the Sedrun village (black circle) and the location of the access shaft (green circle)

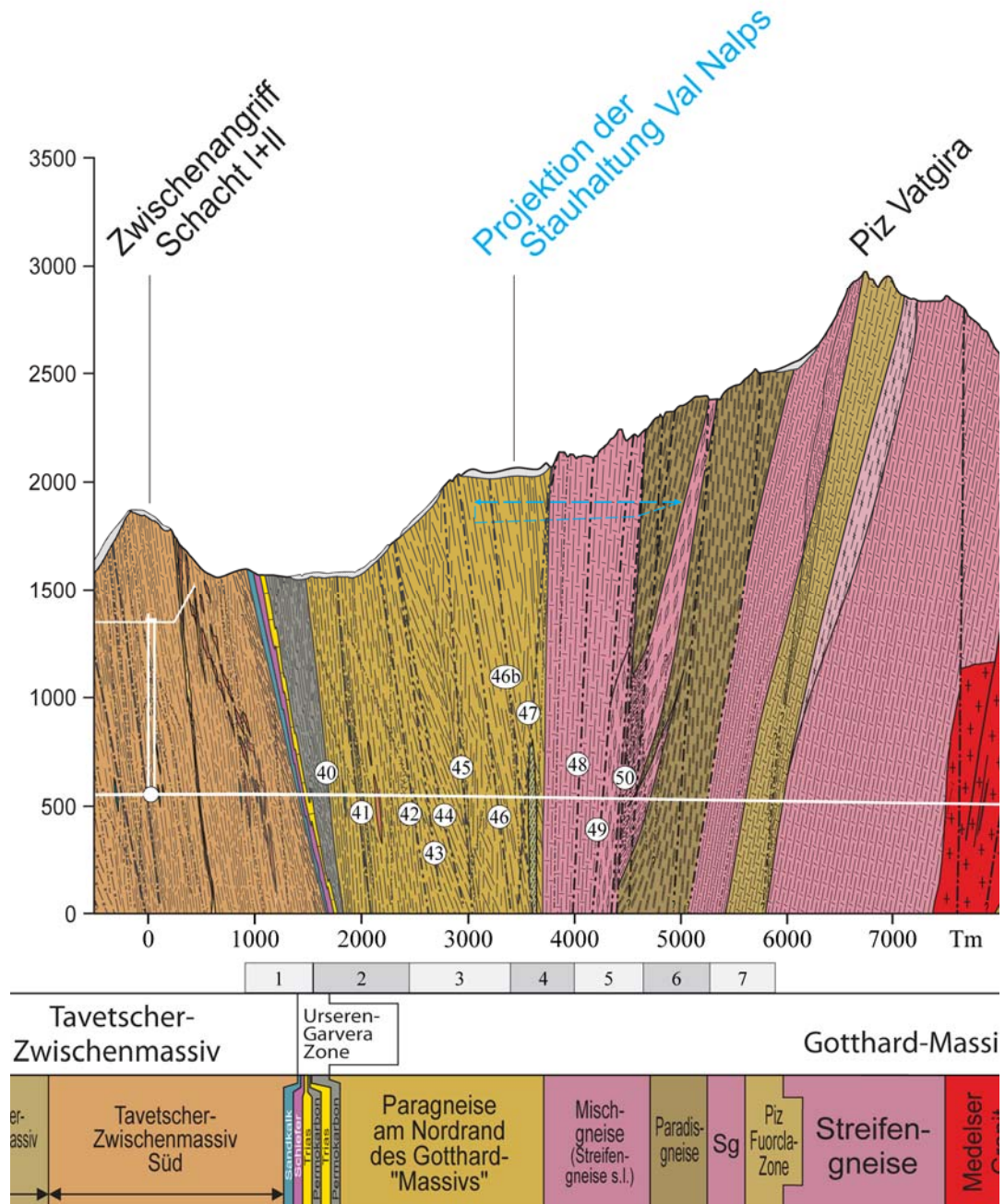


Figure 4-3 Cross-section along the studied section of Gotthard Base Tunnel with the position of the main fault zones with ids and the location of the monitoring sections (pale and medium grey)

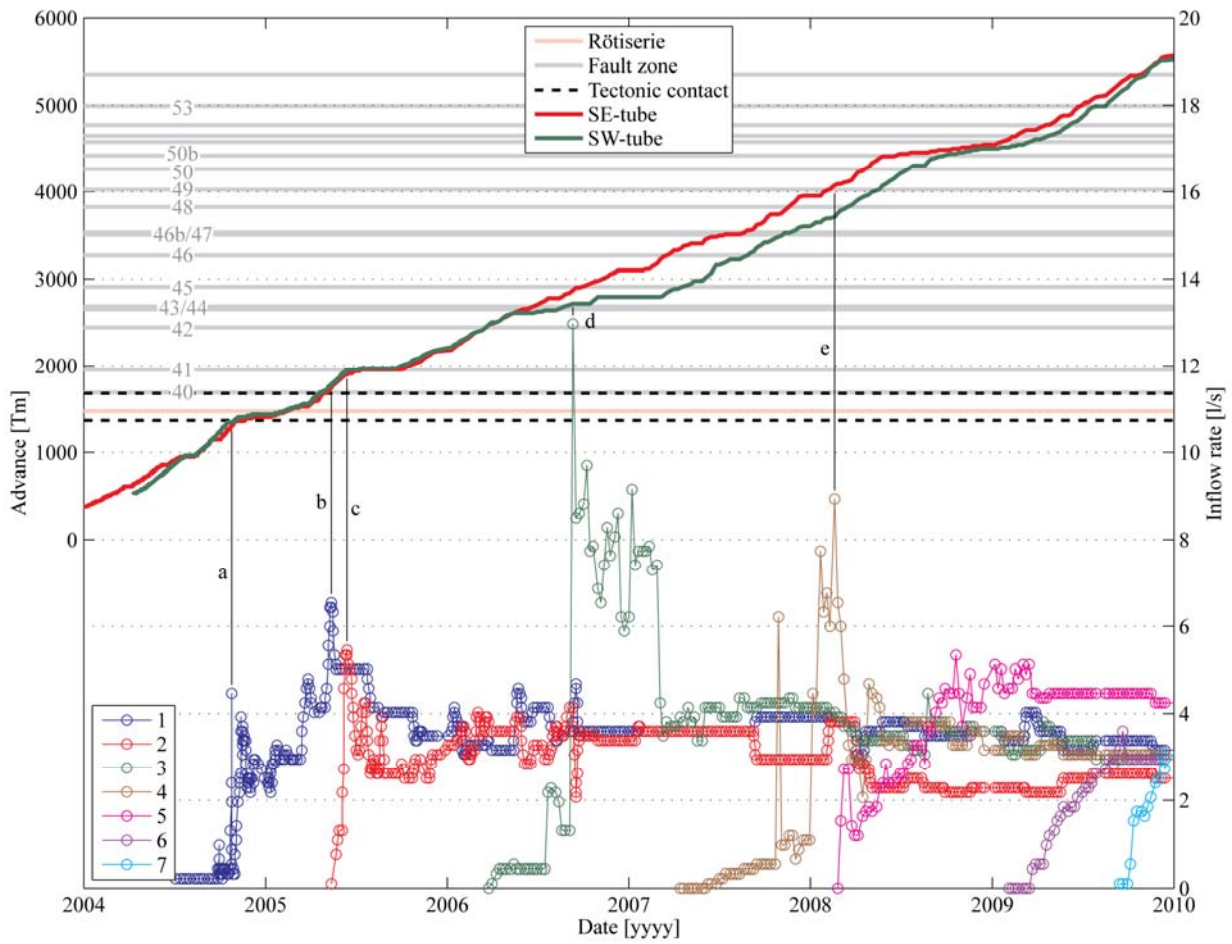


Figure 4-4 Tunnel inflow measured rates of each monitoring section of the tunnel (right y-axis) and advance of each tunnel tube (left y-axis) with location of the main fault zones and structures, in function of the Time (x-axis)

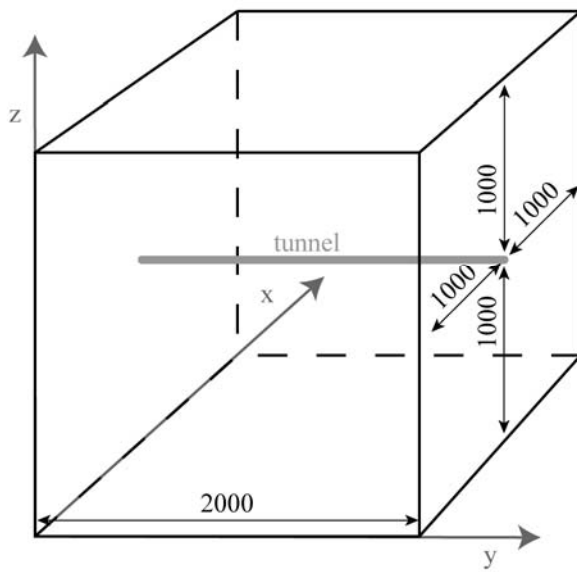


Figure 4-5 Sketch of the box model

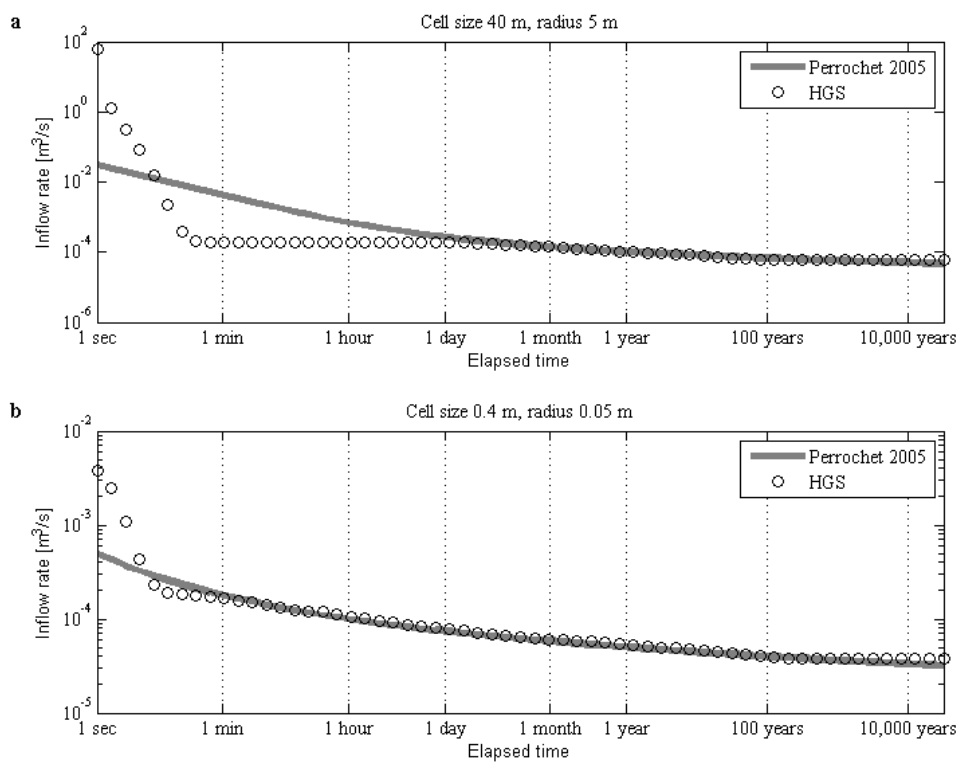


Figure 4-6 Modeled rate for a 5 m tunnel radius and a cell size of 40 m (a), and for a 5 cm borehole radius and a cell size of 40 cm (b)

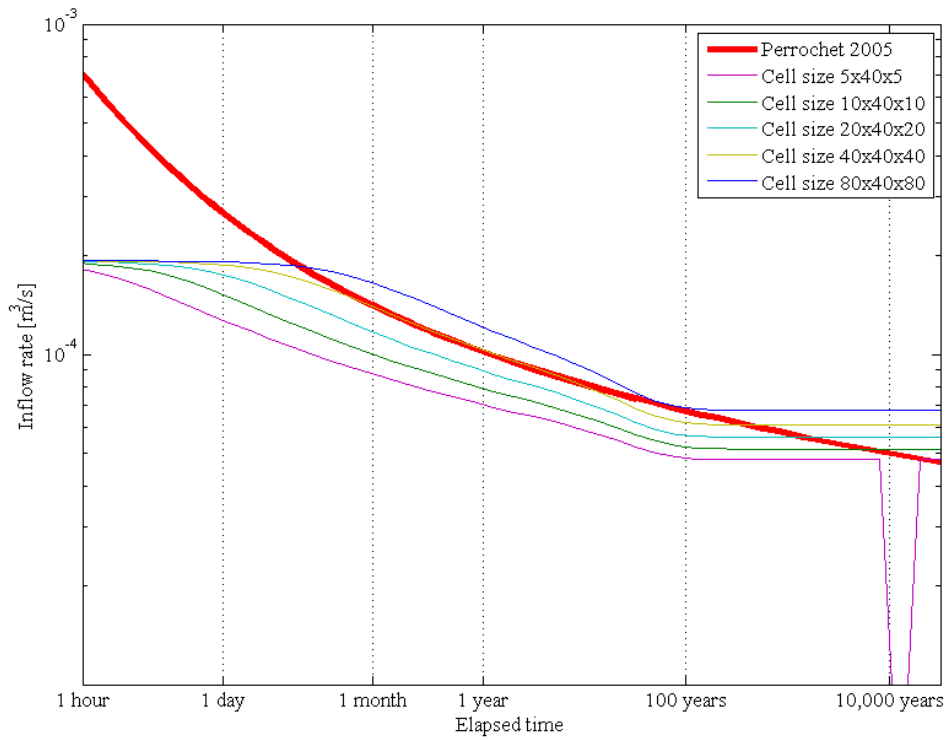


Figure 4-7 Modeled tunnel inflow rates in function of cell size

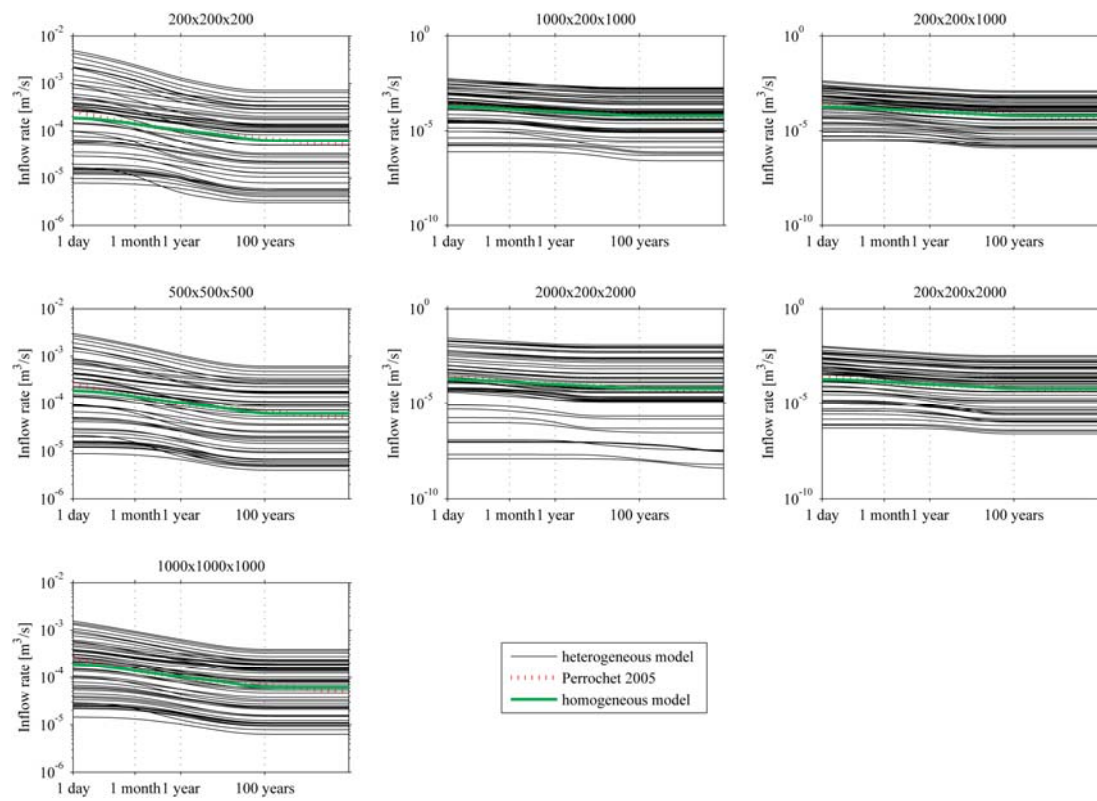


Figure 4-8 Modeled rates of the heterogeneous box model with individual plot titles showing the correlation length in the x, y and z directions

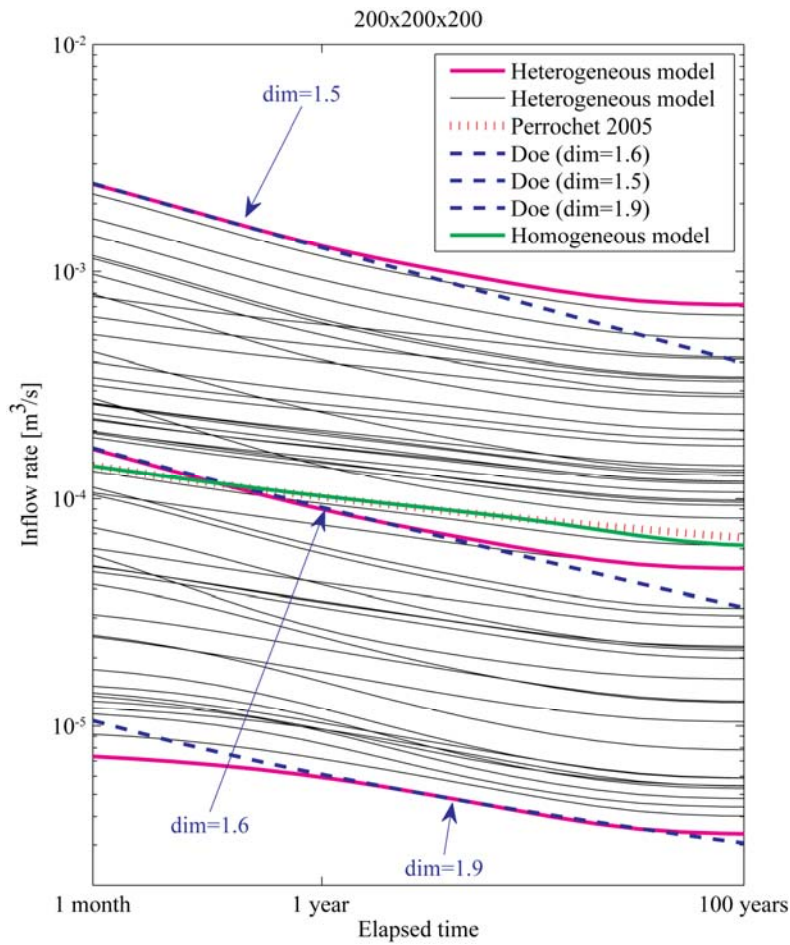


Figure 4-9 Impact of heterogeneous hydraulic conductivity on flow dimension

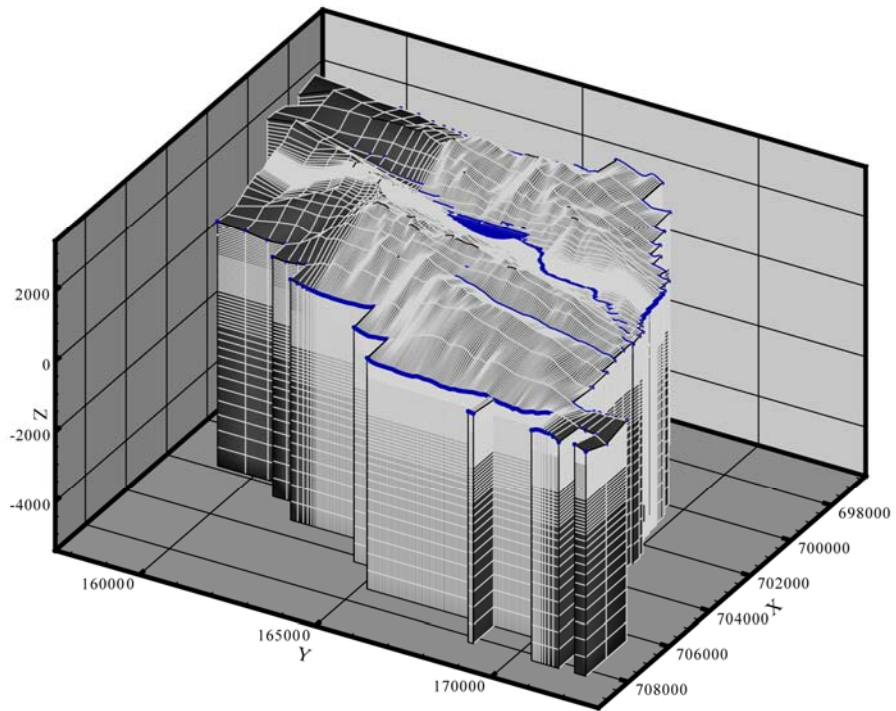


Figure 4-10 GBT model (NE-SW view) with constant head surface nodes at the rivers and lakes locations (blue dots)

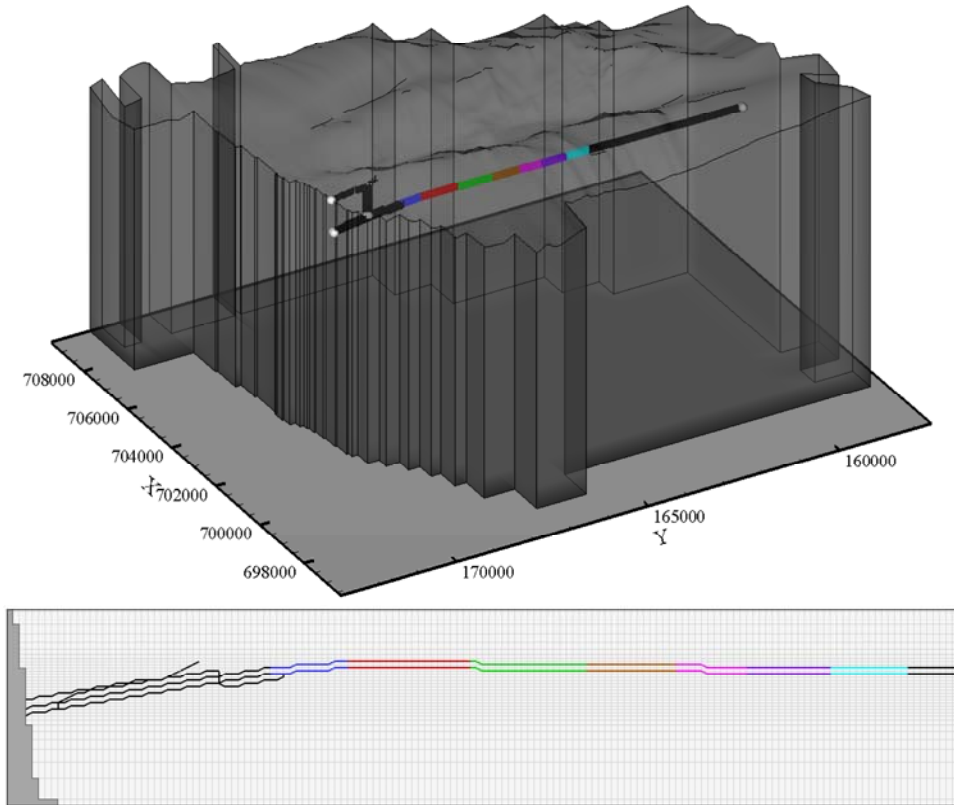


Figure 4-11 GBT model tunnel (NW-SE view) with white spheres representing exutory nodes and plan view of the same tunnel with the different monitoring sections identified by colors (see Table 1 for color code)

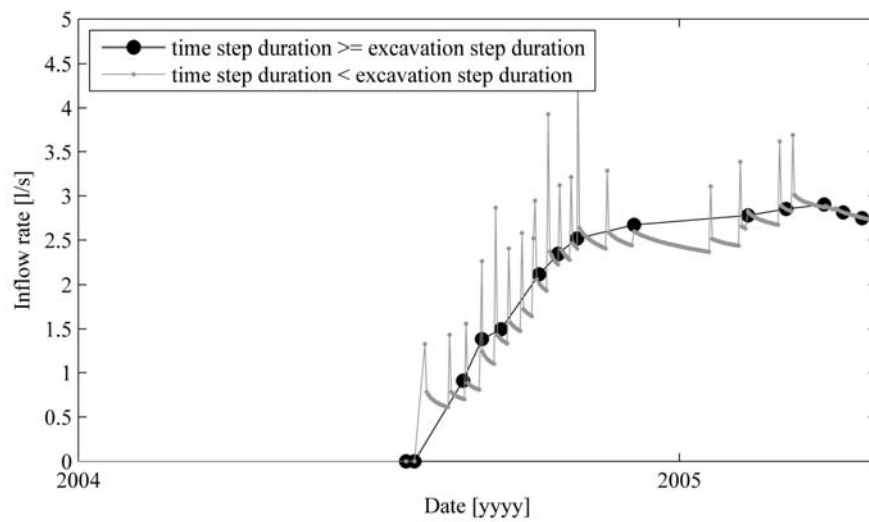


Figure 4-12 Relation between time step and excavation step

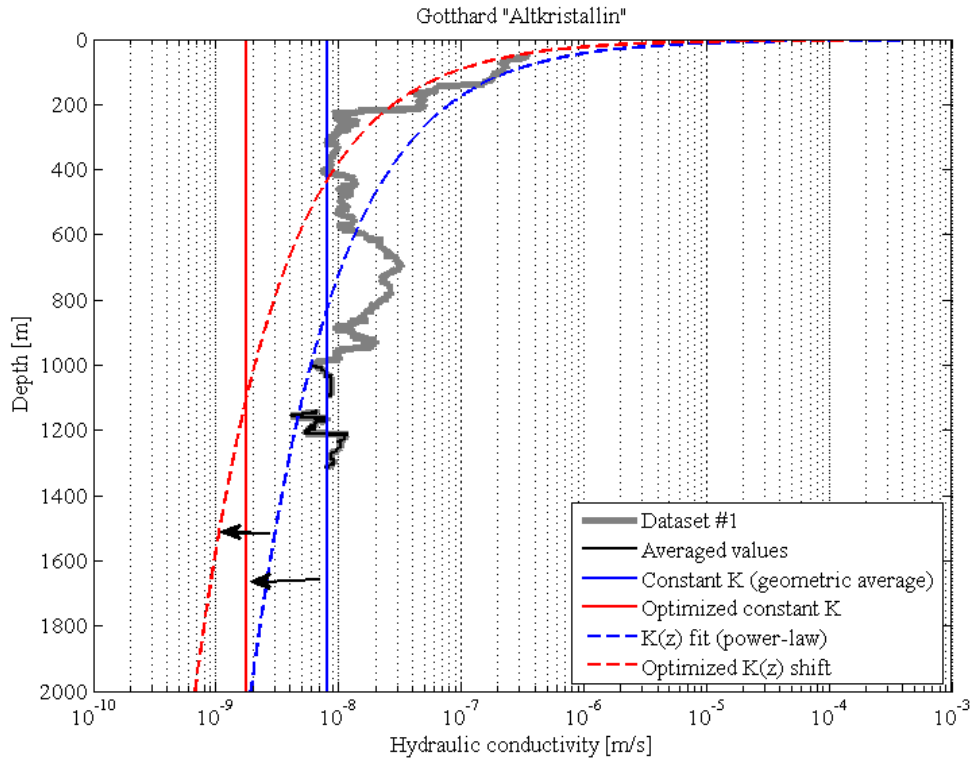


Figure 4-13 "Altkristallin" Hydraulic conductivity distribution with depth

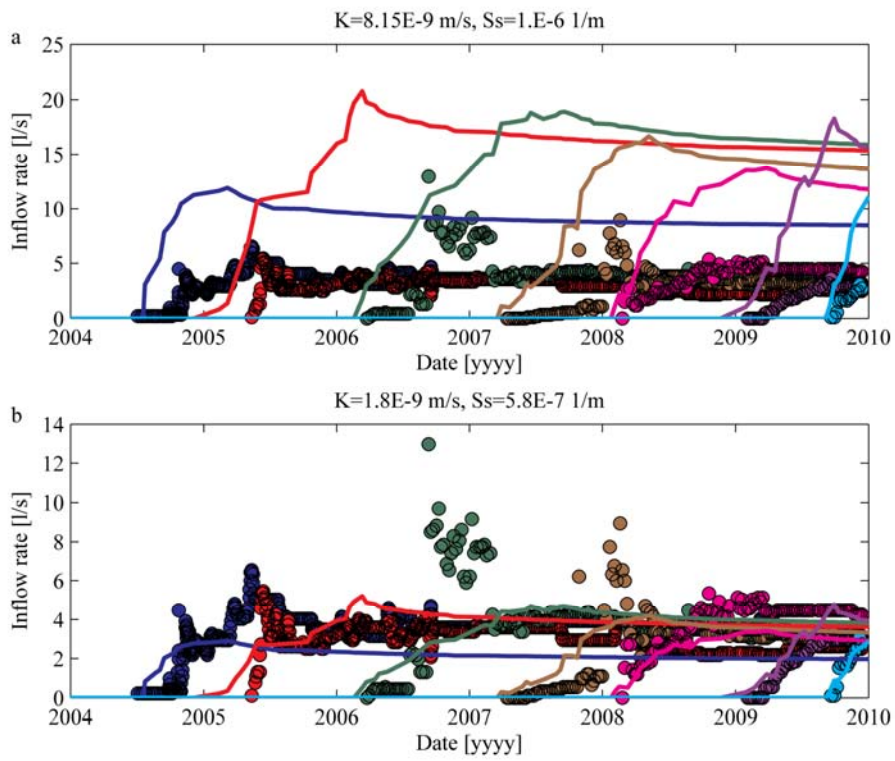


Figure 4-14 Measured rates (dots) and modeled rates (curves) of the GBT homogeneous K model with (a) the hydraulic conductivity derived from the regional analysis and (b) the calibrated hydraulic conductivity and specific storage values

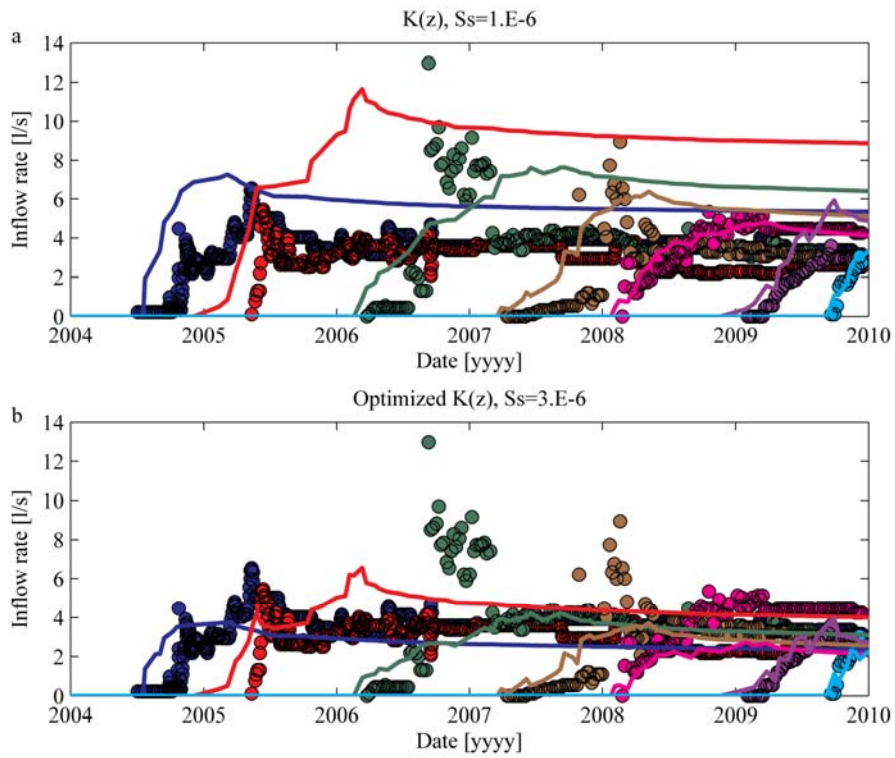


Figure 4-15 Measured rates (dots) and modeled rates (curves) of the GBT depth-dependent K model with (a) the function of hydraulic conductivity with depth derived from the regional analysis and (b) the calibrated function of hydraulic conductivity with depth and specific storage value

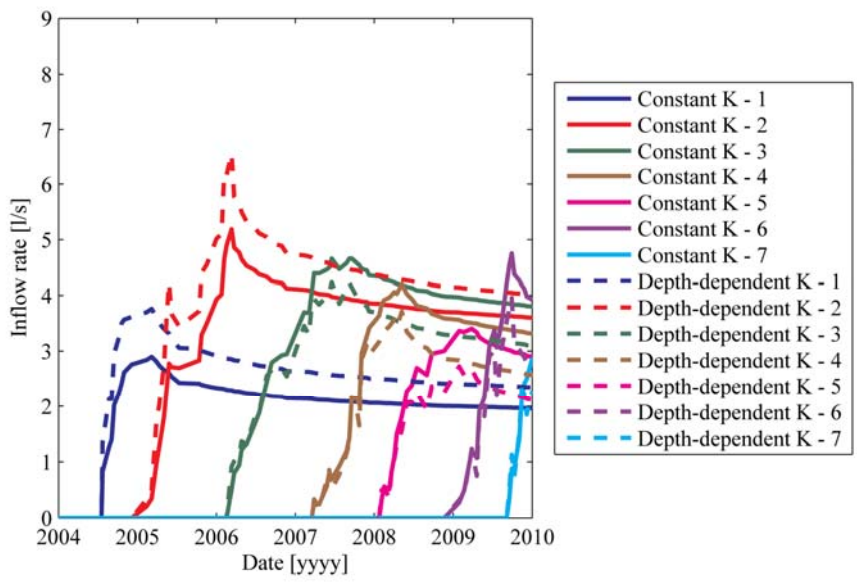


Figure 4-16 Comparison of the modeled rates of the constant and depth-dependent K models

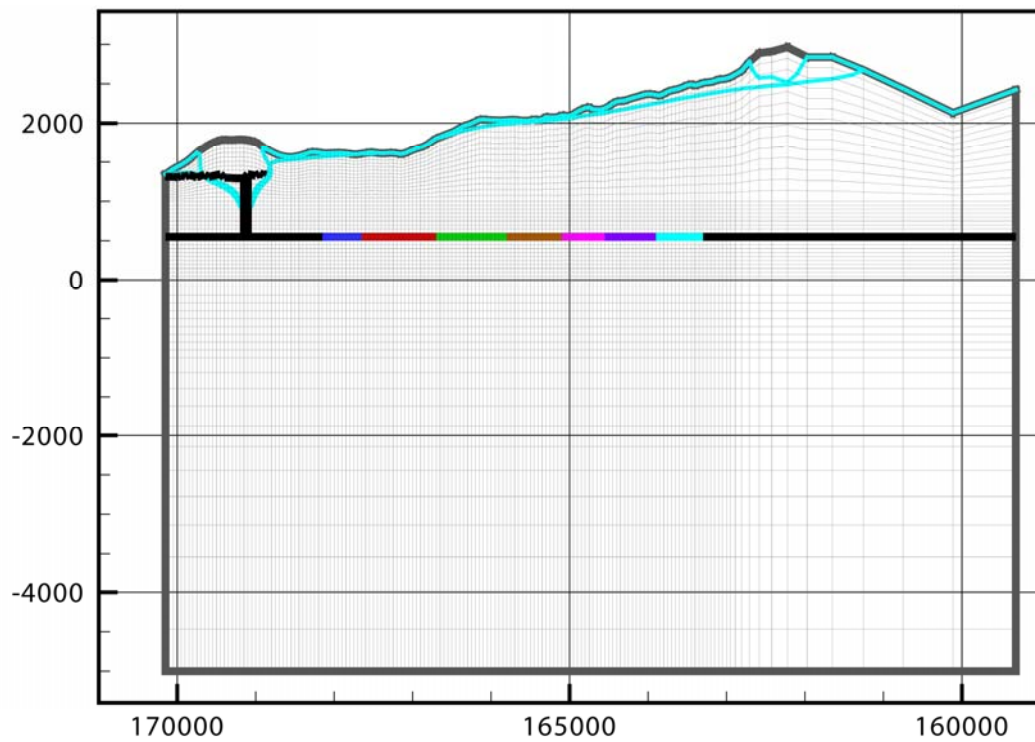


Figure 4-17 Comparison of the steady-state water table elevation of the constant (upper water table position) and depth-dependent (lower water table position) K models (X=702000)

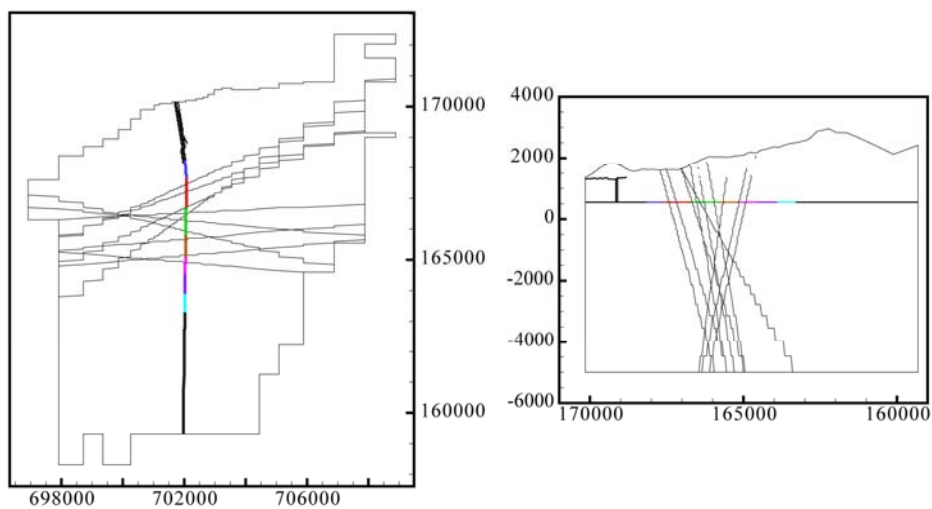


Figure 4-18 Cross-sections of the continuous fault zone model (Z=550 and X=702000)

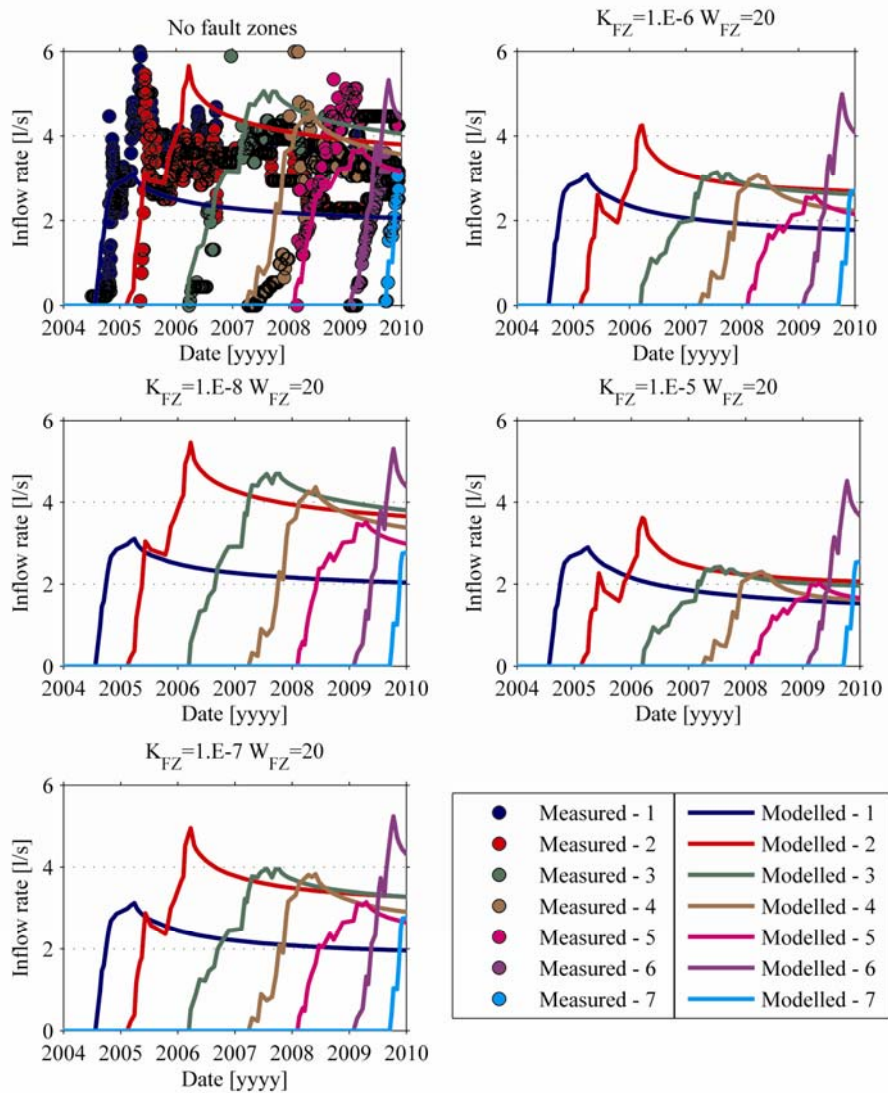


Figure 4-19 Impact of conductive planes (fault zones) on modeled rates with varying fault zone conductivity

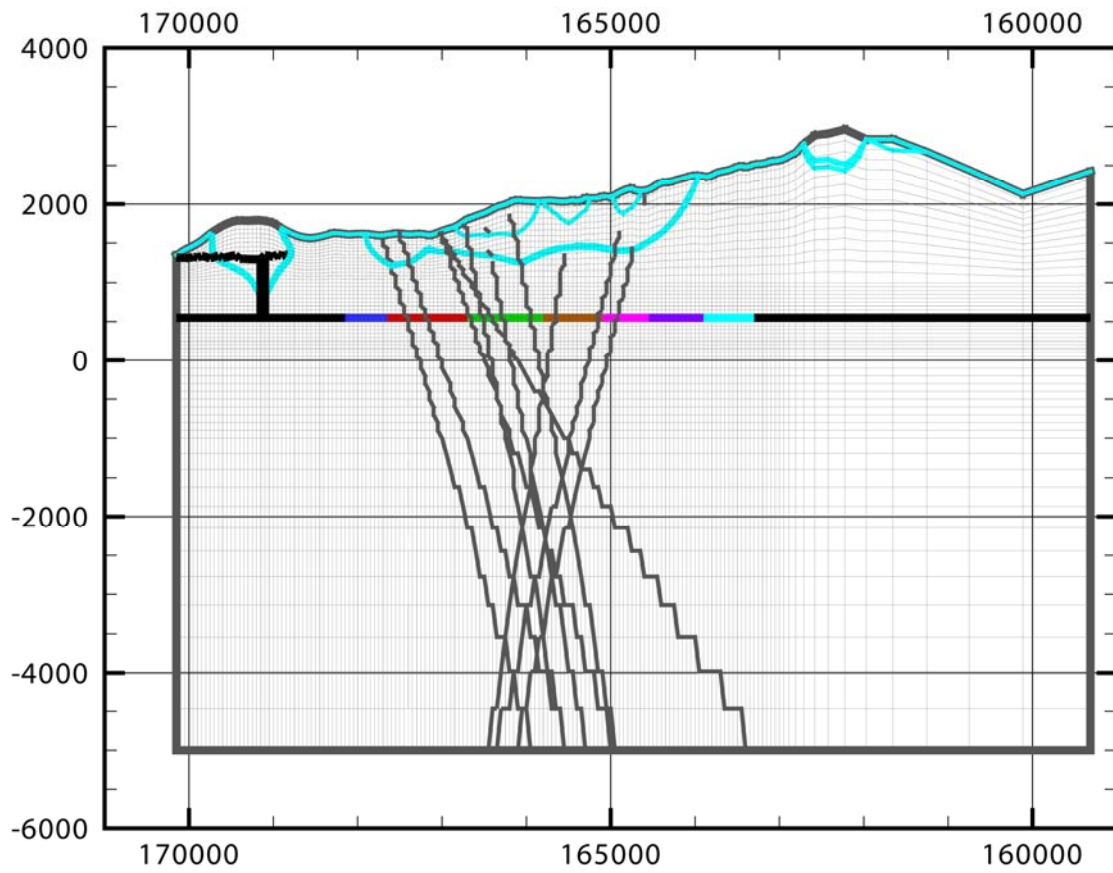


Figure 4-20 Impact of transmissive planes (fault zones) on water table position (X=702000) with the different stages of the water table position resulting from the change in the properties assigned to the planes as shown in Figure 19 (the lower water table position corresponding to the higher conductivity values)

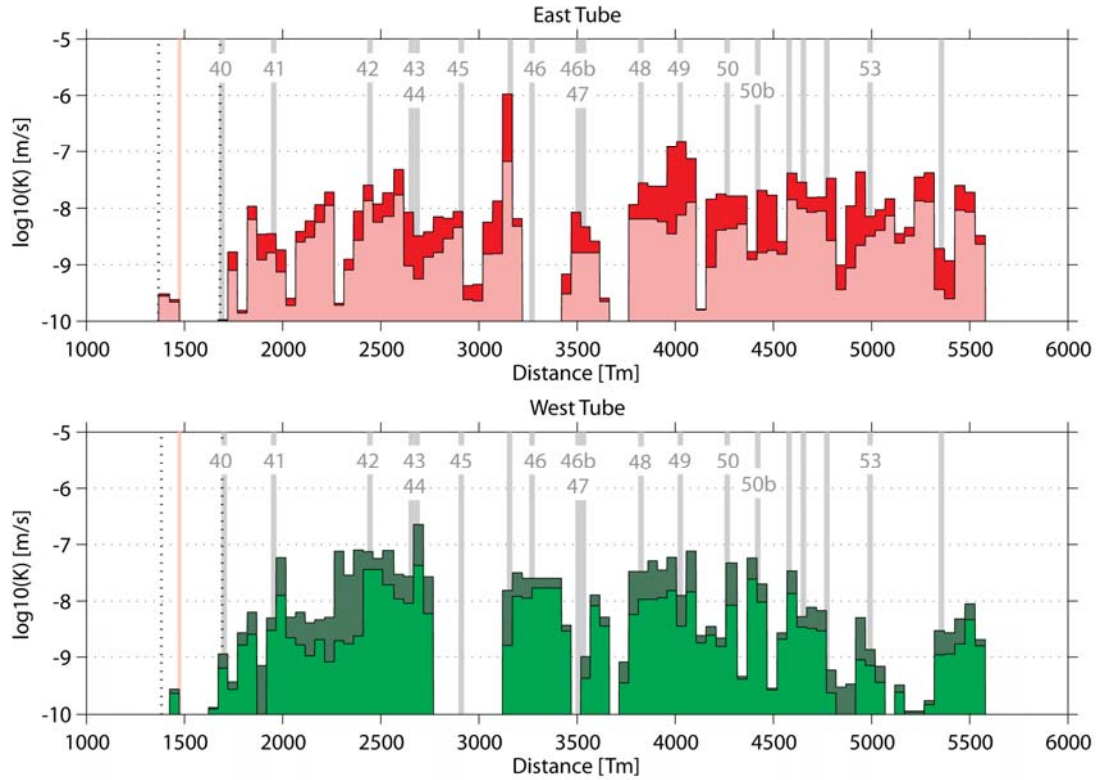


Figure 4-21 Back-calculated hydraulic conductivity distribution along each tunnel tube with location of the main fault zones

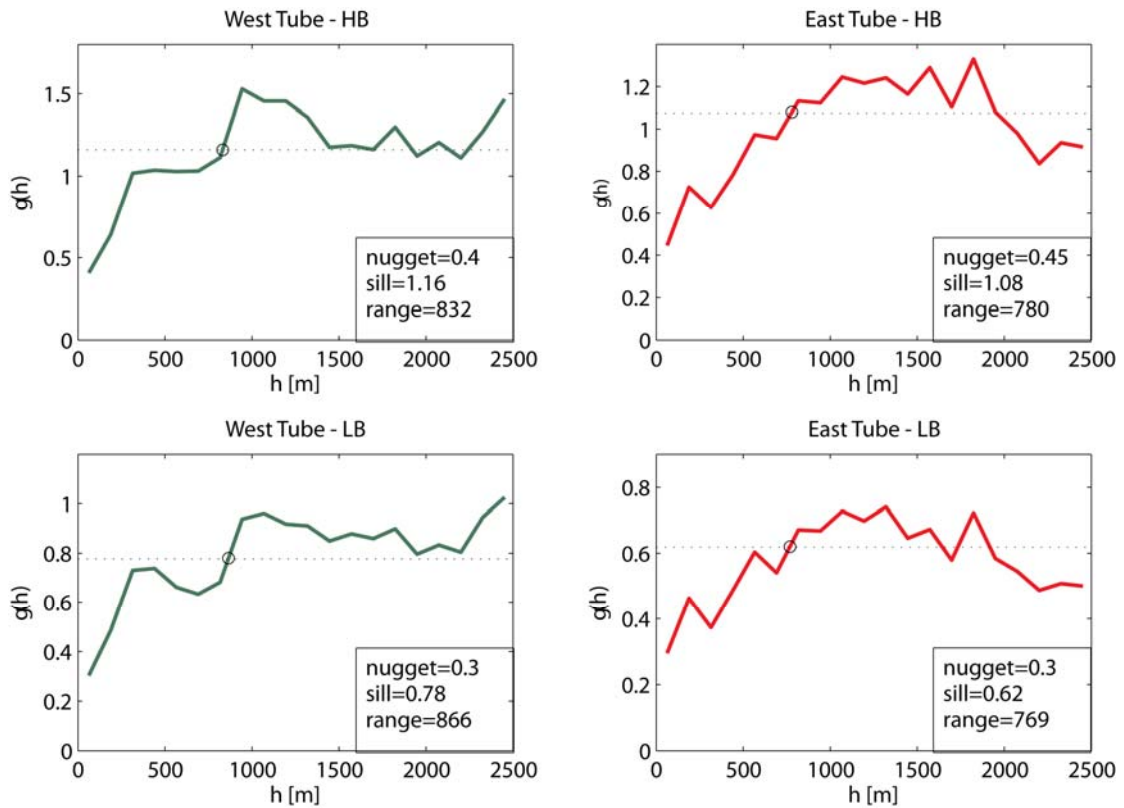


Figure 4-22 Empirical variograms of hydraulic conductivity along each tunnel tube and for the higher (HB) and lower-bound (LB) hydraulic conductivity distribution

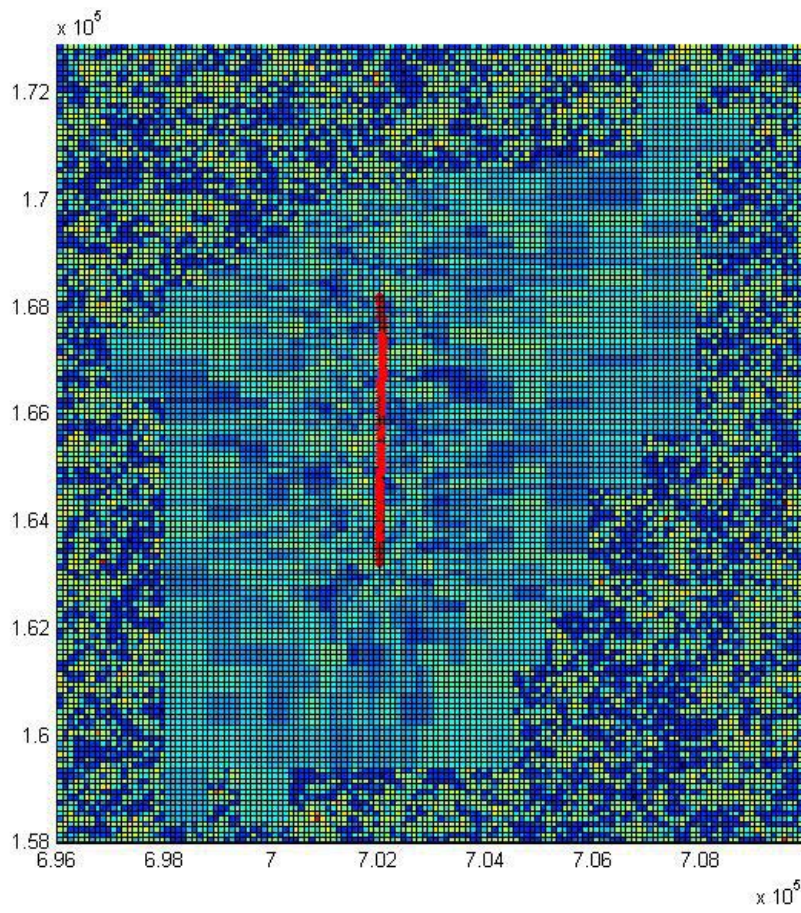


Figure 4-23 Cross-section through an upscaled hydraulic conductivity field (Z=550)

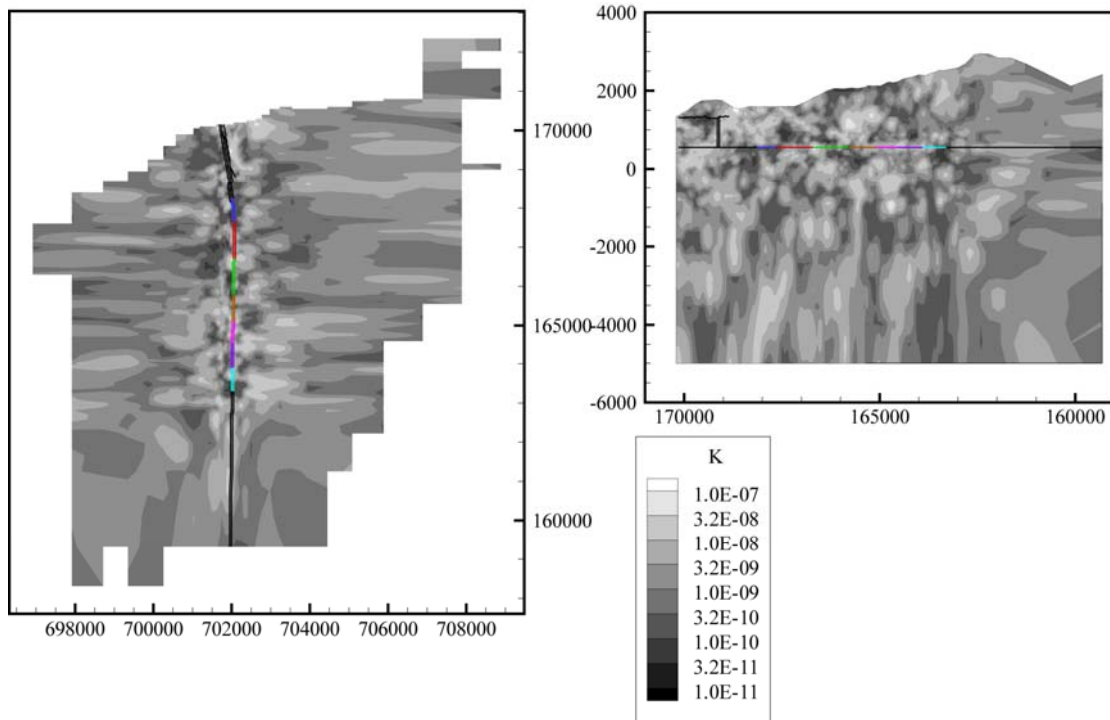


Figure 4-24 Cross-sections through the stochastic model ($Z=550$, $X=702050$, exponential, no nugget, sill=1, $cl=500$)

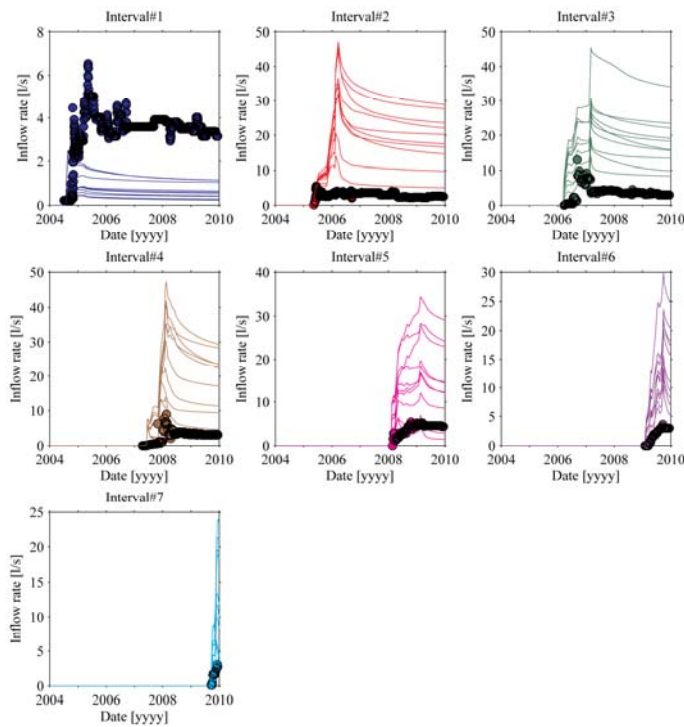


Figure 4-25 Stochastic model with isotropic 1000 m correlation length and higher bound K-values

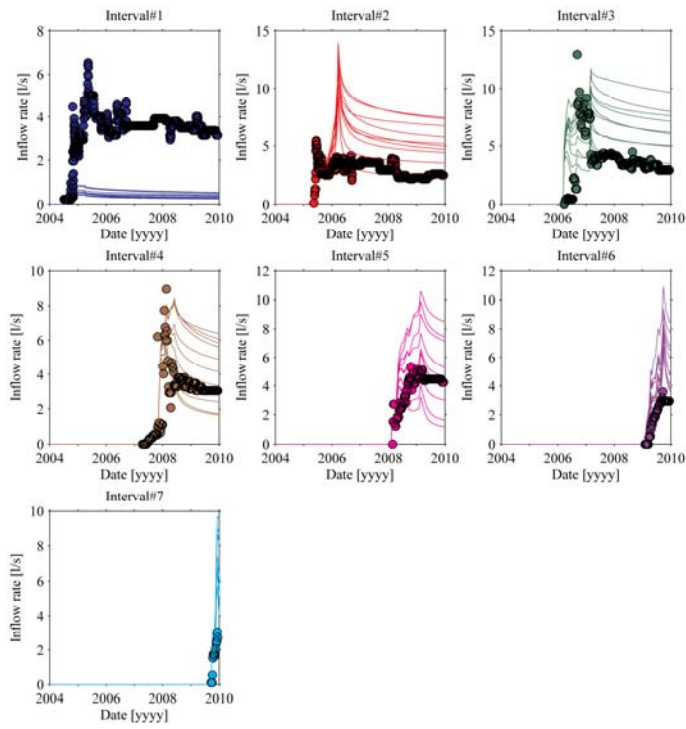


Figure 4-26 Stochastic model with isotropic 1000 m correlation length and lower bound K-values

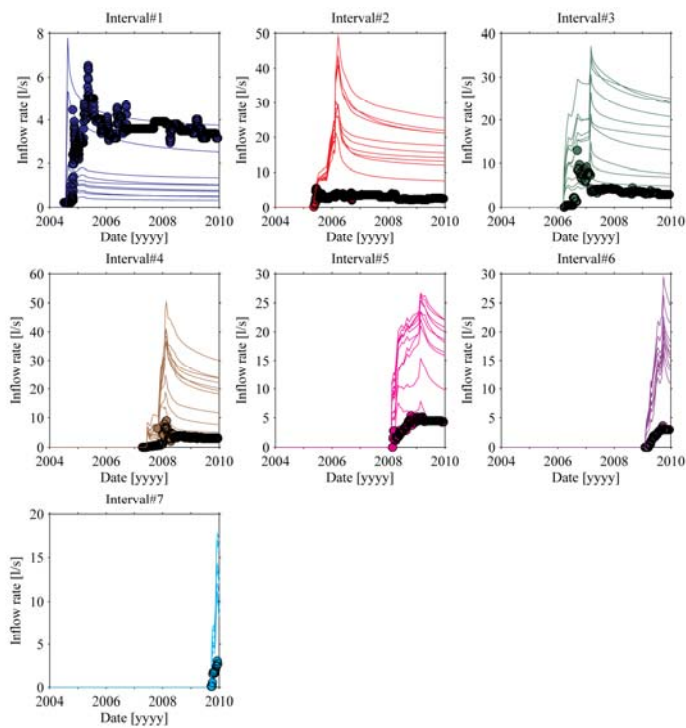


Figure 4-27 Stochastic model with isotropic 500 m correlation length and higher bound K-values

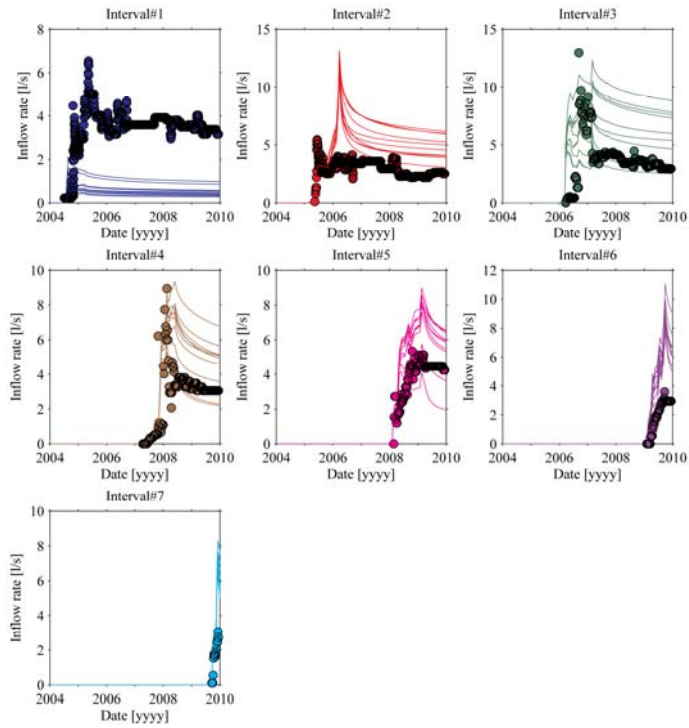


Figure 4-28 Stochastic model with isotropic 500 m correlation length and lower bound K-values

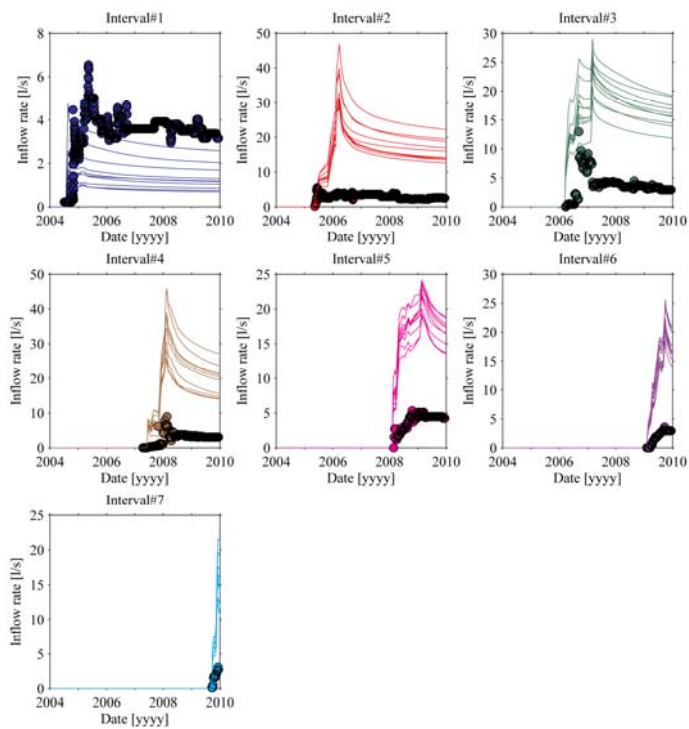


Figure 4-29 Stochastic model with isotropic 250 m correlation length and higher bound K-values

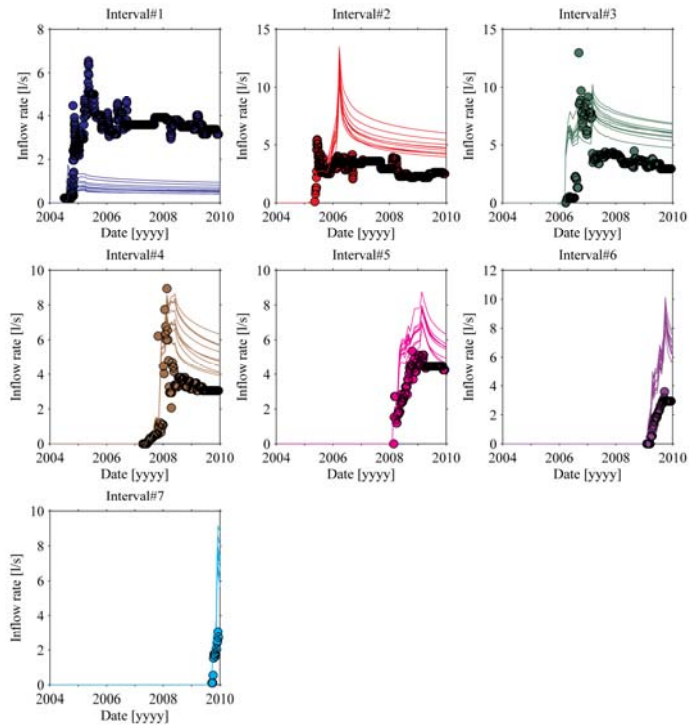


Figure 4-30 Stochastic model with isotropic 250 m correlation length and lower bound K-values

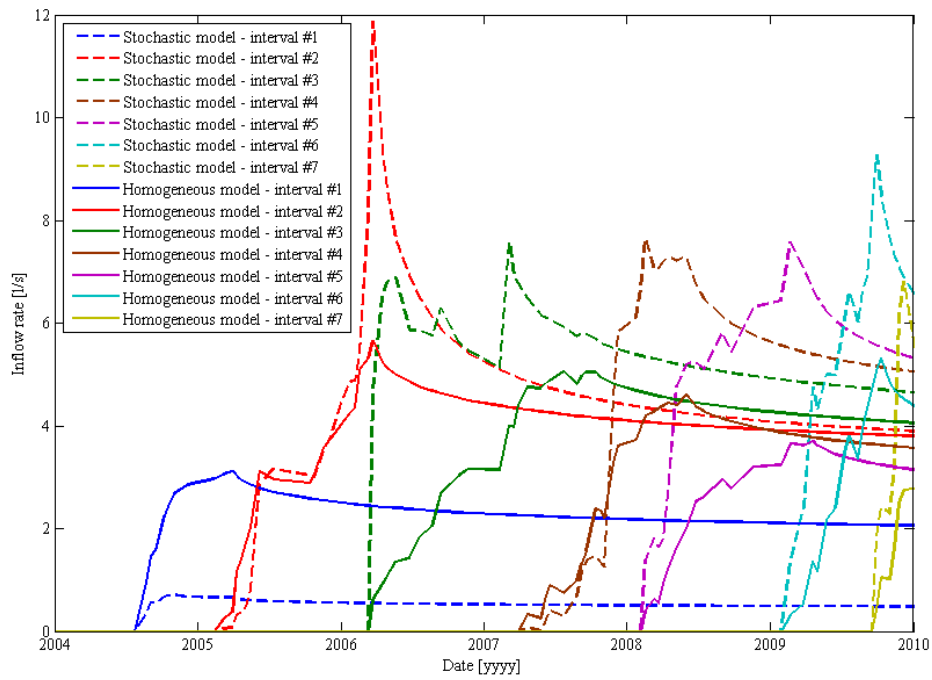


Figure 4-31 Comparison of the modeled rates of the homogeneous K and stochastic models (one realization)

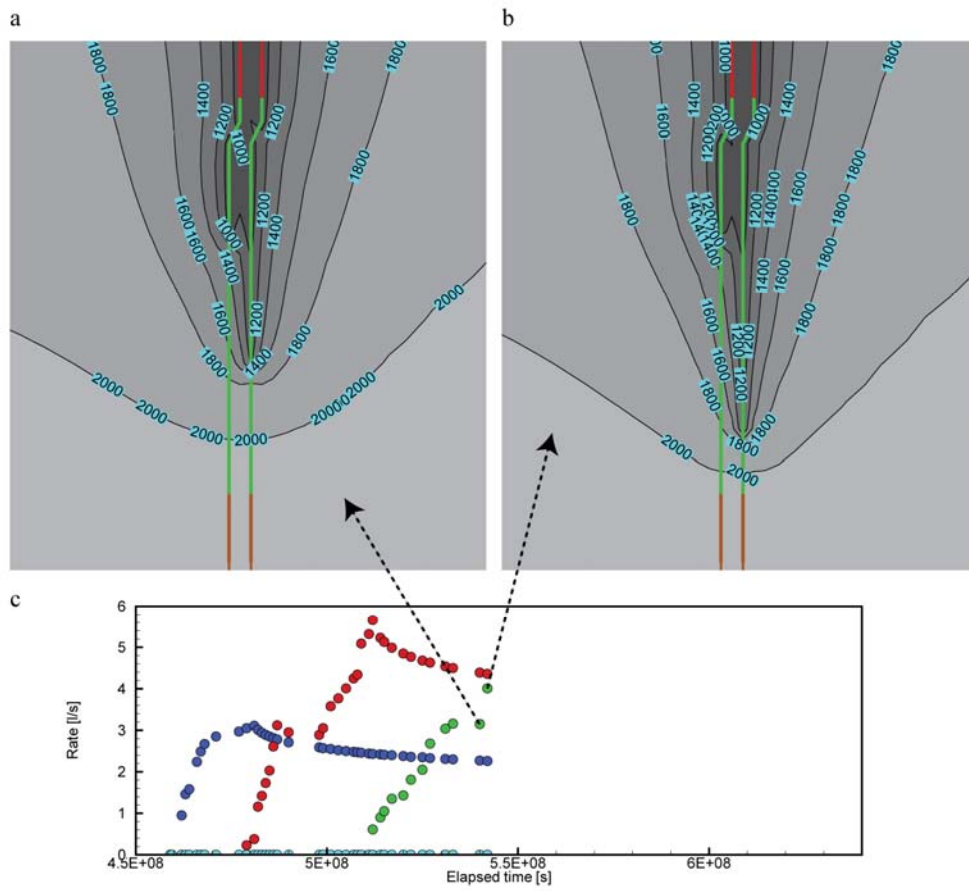


Figure 4-32 Slow excavation speed (a) versus high excavation speed (b) impact on pore pressure distribution and corresponding inflow rates and time steps (c)

5. Concluding remarks

This PhD project benefitted from an exceptional quantity of inflow data from varying sources and quality. Some of the main challenges related to these data were their homogenization and the evaluation of associated uncertainties. The Monte Carlo simulation constitutes a pragmatic and efficient way to calculate the uncertainty related to the input parameters when back-calculating hydraulic conductivity values from inflow rates.

Although originated from industrial projects and not meant for research, the inflow data analyzed allowed for a good characterization of the large scale hydraulic conductivity distribution in the Aar and Gotthard crystalline massifs. The derivation of the rock mass hydraulic conductivity through simple inflow rate measurement or basic borehole inflow logging is not as precise as its derivation with packer tests but it is cheaper, easier to implement and still of great value given the amount of data.

The analysis of the inflow rate to Gotthard Base Tunnel pre-drillings gave insights into the medium scale distribution of hydraulic conductivity along a specific section of Gotthard Base Tunnel. The comparison of the distribution along each tunnel tube shows that the correlation between the two tubes, separated by a distance of 40 meters, is weak. Furthermore, the finite element modeling of Gotthard Base Tunnel transient excavation showed that the best reproduction of the transient inflow rate to a tunnel section during the excavation is obtained with a stochastic continuum model with a Gaussian distribution of hydraulic conductivity. In contrast, a constant hydraulic conductivity model including continuous planes of higher transmissivity proved to be inappropriate. Consequently, for the portion of the Gotthard massif considered, a conceptual model considering the major fault zones as continuous planes of higher transmissivity is unrealistic. From the point of view of the inflow rate the stochastic continuum model is the most appropriate of the tested models.

Finally a basic box model was sufficient to demonstrate that the heterogeneous distribution of hydraulic conductivity leads to flow channeling going in pair with a reduction of the flow dimension. Flow dimension might therefore constitute a mean to constrain heterogeneity. In other words when simulating the transient inflow rate to an excavation, heterogeneity should be structured in such a way that the flow dimension is reproduced.

Open questions remain concerning the distribution of the specific storage which was always assumed constant in the implemented models and may vary in reality. Furthermore, the present thesis describes the distribution of hydraulic conductivity mainly from the point of view of tunnel, gallery and borehole inflow rates. Clarifying the relation between fracture properties and hydraulic conductivity may be complementary and allow the derivation of more realistic models of the distribution of hydraulic conductivity. Lastly, smaller-models in terms of space and time scale may be designed to study the tunnel inflow early rates.

Curriculum vitae

Personal details

Name: Masset
First name: Olivier
Date of birth: 18.05.1977
Place of birth: Lausanne
Nationality: Swiss

Education

1999-2004: Diploma of geologist, Earth Sciences department, University of Lausanne

2004-2005: Master of advanced studies in engineering and environmental geology, GEOLEP, Swiss Federal Institute of Technology Lausanne

2006-2011: Doctoral thesis, Engineering Geology group, Earth Sciences department, Swiss Federal Institute of Technology Zurich